LBL-891

MOLECULAR BEAM KINETICS

Shen-Maw Lin
(Ph. D. Thesis)

September 1972

AEC Contract No. W-7405-eng-48

LBL-891

DISCLAIMER

Table of Contents

MOLECULAR BEAM KINETICS

Shen-Maw Lin

Inorganic Materials Research Division, Lawrence Berkeley Laboratory
and Department of Chemistry; University of California,
Berkeley, California

ABSTRACT

A crossed molecular beam apparatus has been constructed to measure angular distributions of reactively scattered products of Group IIA alkaline earth metals by employing an electron-impact-ionizer-massfilter detector. Product center-of-mass (CM) recoil energy and angular distributions have been fit to the measured laboratory (LAB) angular distributions by averaging over the measured (non-thermal) beam speed distributions. Studies have been made of the reactions of Ba, Sr, Ca, and Mg with Br_2, Cl_2, CH_3I, CH_2I_2, CCl_4, CF_3I, $(CH_3)_2CHNO_2$, and CCl_3NO_2. These reactions have been found to span a wide range of chemical behavior; in the CM coordinate system, they vary from forward scattering for Br_2, Cl_2, CH_2I_2, CCl_3NO_2, and $(CH_3)_2CHNO_2$ to backward scattering for CH_3I, with intermediate behavior for CCl_4 and CF_3I.

For the halogen reactions, there is no indication of a dihalide product (MeX_2) and the fraction of the product scattered into the forward CM hemisphere increases in the sequence: Mg, Ca, Sr, Ba. The similarity to the alkali atom reactions is most pronounced for the Ba atom reactions and least pronounced for the Mg atom reactions. In this work, not all of the alkaline earth atoms have been observed to react with the six organic compounds studied here; for Mg, no product

has been found. Of the six organic reactants, measurements of product LAB angular distributions for the reactions of CH_3I, CH_2I_2, and CCl_4 with alkali atoms have been made; similarities and differences between the present results and features of the reactions of alkali atoms are discussed.

A comparison is presented between transition probabilities for photodissociation of HI and of NaI obtained by two methods: (1) by exact numerical evaluation of the Franck-Condon overlap integrals and (2) by the "delta approximation" wherein the vibrational wavefunction of the bound state is reflected onto the continuum state potential. Both methods were used to constract the repulsive potentials from the observed continuous spectra in the two molecules; for both molecules, the delta approximation provided estimates potential energies which were significantly lower than those obtained from the exact Franck-Condon calculations and $\bar{r}$-centroid analysis indicates that the Franck-Condon principle is a good approximation.

I. INTRODUCTION

The ideal experimental approach to dynamic problems in a chemical or physical system consists in probing the molecular, or microscopic, picture rather than the macroscopic ensemble in which a loss of detailed information is entailed due to statistical averaging effects. The technique of crossed molecular beam experiments offers the chemists a unique opportunity to achieve this ultimate goal. Although there are certain practical problems limiting the choice of feasible experiments, some potential advantages of employing a suitable crossed beam arrangement are selection of a specified translational and internal energy state for the reactants; identification of product energy states and recoil directions which are not masked by any subsequent collisions; and direct location of threshold energy for chemical reactions and other collision dynamics.

The observation of the scattering of molecular beams by gases was first demonstrated by Dunoyer[1] in 1911. In the 1920's beams were used to verify kinetic theory of gases in a number of semiquantitative measurements.[2] Concurrently, Gerlach and Stern[3] observed the quantization of angular momentum by deflection in an inhomogeneous magnetic field. This led to the growth of magnetic (and later electric) resonance spectroscopy whereby many properties of atoms and molecules were measured as a result of their deflection in inhomogeneous magnetic and electric fields. The usefulness and versatility of these powerful beam methods for the elucidation of atomic and molecular structure have been extensively discussed in Ramsey's manuscript.[4]

The scattering processes that take place in crossed molecular beams may be generally divided into three categories: elastic, inelastic and reactive scattering. In the process of elastic scattering neither change of internal quantum state of collision particles nor chemical rearrangement occurs. The interacting force that dominates the dynamics of such a collision can be determined from measurements of angular distribution of elastic scattering of a non-reactive system.[5] In addition, the elastic scattering from a chemically reactive system also provides indirect information about the reaction probability as a function of collision impact parameter.[6] On the other hand, inelastic scattering is characterized by a change of the internal quantum states of the collision partners during the period of interaction. In principle, the collisional exchange of energy among electronic, vibrational, rotational, and translational energy is possible; thus, compared to elastic scattering, a much more complicated and diverse situation exists.[7]

A collision process that involves a chemical change is defined as reactive scattering. One of the first successful beam experiments was carried out by Bull and Moon[8] in 1954. In 1955, Taylor and Datz[9] developed a two filament surface ionization detector which provided differential detection of both scattered alkali atoms and alkali halides produced by crossing beams of K + HBr. Following this discovery, extensive investigations of the dynamics of alkali reactions have been successfully pursued for the past eighteen years.[10] Information on the dynamics of a chemical reaction in crossed molecular beam experiments is in principle derived from measurements of both angular and

kinetic energy distributions of reaction products. Measurement of angular distribution provides information on the reaction cross section which is closely related to the traditional macroscopic rate constant and the lifetime of the collision complex. On the other hand, the partitioning of the available reaction energy between internal and external degrees of freedom in the products can be evaluated from a measurement of the spectrum of product kinetic energy. Even in experiments which measure only the product angular distribution in the laboratory coordinate system (LAB), however, energy disposal in the products may also be estimated from the transformation of the LAB angular distribution into the center-of-mass coordinate system (CM).[11]

Crossed molecular beam studies of reactive scattering of both ionic and neutral species have developed very rapidly in the past few years. Two main thrusts have become apparent in the evolution of this field. One is dedicated towards diversification of the various types of chemical reactions studied and the other seeks a greater apparatus sophistication so as to be able to measure cross sections for a few reactions as functions of quantum states of both reactants and products. With the improved technical development of the nozzle beam source and the universal detecting system employing electron-impact ionization, investigations of the collision dynamics of neutral species in crossed molecular beams have received a great impetus recently.[12,13] Results presented here from chapters II to IV extend investigations of reactive scattering on crossed beam experiments to the Group IIA alkaline earth atom reactions. Employing two beams with full velocity distributions, the

product angular distributions are measured and nominal values of the product translational recoil energies are extracted.

Chapter V deals with theoretical calculations of transition probabilities for photodissociation of a diatomic molecule from its ground electronic state into excited continuum states whose wavefunctions are obtained from one-dimensional box (energy) normalization. Results are compared with continuous spectra measured experimentally and potential curves of continuum states of HI and NaI molecules are extracted by means of a trial and error method. Comments on traditional delta-approximation treatments[14] which simply reflect the ground state vibrational probability density function to the corresponding turning point of upper continuum state are also given.

REFERENCES

1. L. Dunoyer, Radium, Paris. 8, 142 (1911).

2. (a) M. Born, Z. Phys. 21, 578 (1920). (b) F. Knauer and O. Stern, Z. Phys. 39, 764 (1926); 53, 766 (1929).

3. W. Gerlach and O. Stern, Z. Phys. 9, 349 (1922).

4. N. F. Ramsey, Molecular Beams. (Oxford University Press, London, 1963).

5. (a) H. Pauly and J. P. Toennies, Methods of Experimental Physics. VII A. Atomic Interactions. p 227. (Academic Press, N.Y. 1968). (b) R. B. Bernstein and J. T. Muckerman, Advances in Chemical Physics. XII. Intermolecular Forces. p 389. (Interscience Publishers, N.Y. 1967).

6. (a) J. Ross and E. F. Greene, Proceedings of the International School of Physics. Course 44. Molecular Beams and Reaction Kinetics. p 87. (Academic Press, N.Y. 1970).
(b) E. F. Greene, A. L. Moursund, and J. Ross, Advances in Chemical Physics. X. Molecular Beams. p 135. (Interscience, N.Y. 1966).
(c) F. T. Smith, R. P. Marchi, and K. G. Dedrick, Phys. Rev. 150, 79 (1966).

7. (a) R. B. Bernstein, Proceedings of the Conference on Potential Energy Surfaces in Chemistry. Santa Cruz. p 27. (IBM Research Laboratory, San Jose, RA 18, No. 14748, 1970).
(b) see Ref. 6-(a). R. J. Cross Jr., p 50.

8. T. H. Bull and P. B. Moon, Disc. Far. Soc. 17, 54 (1954).

9. E. H. Taylor and S. Datz, J. Chem. Phys. 23, 67 (1955).

10. (a) For a review, see F. Westley, Rates of Reactions of Alkali Metals with Halogens in Gas Phases. NBS66 (1970).

(b) see Ref. 6-(b). D. R. Herschbach, p 319.

11. (a) D. D. Parrish, Ph. D. thesis, University of California, Berkeley. (1970).

(b) E. A. Entemann, Ph. D. thesis, Harvard University, Cambridge, Mass. (1967).

12. (a) For a review, see J. L. Kinsey, Intern. Rev. of Science (Phys. Chem.). vol. 9. Chemical Kinetics. Chapt. 6. Molecular Beam Kinetics. (J. C. Polanyi, Ed., Med. Tech. Publisher, 1972); and references cited therein.

(b) see Ref. 7-(a). D. R. Herschbach, p 44.

13. T. J. Odiorne, P. R. Brooks, and J. V. Kasper, J. Chem. Phys. 55, 1980. (1971).

14. (a) J. F. Ogilvie, Tran. Far. Soc. 67, 2205 (1971).

(b) H. G. Hanson, J. Chem. Phys. 23, 1391 (1955).

(c) G. Herzberg, Molecular Spectra and Molecular Structure. I. Spectra of Diatomic Molecules. p 391. (Van Nostrand, Princeton, 1950).

(d) A. S. Coolidge, H. M. James, and R. D. Present, J. Chem. Phys. 4, 193 (1936).

II. APPARATUS FOR CROSSED MOLECULAR BEAM STUDIES

A. Introduction

The crossed beam apparatus used in this study consists of three distinct chambers, each with its own high vacuum pumping system. The first chamber is differentially pumped by a combination of a 150 l/s ion pump on the top and a 11 l/s ion pump at the bottom; each ion pump is assisted by a liquid nitrogen cooled titanium sublimator unit. This chamber is further divided into 3 sub-chambers; the second sub-chamber contains most of the essential parts of the detector: an electron-impact ionizer, quadrupole mass filter and electron multiplier. This entire detection chamber may be rotated through a large range of angles with respect to the stationary ovens, thereby making possible the measurement of the in-plane angular distributions of scattered species. Another chamber houses the high temperature oven which produces a beam of alkaline earth atoms. This beam is admitted to the collision chamber through a collimating slit and is intersected perpendicularly at the center-of-rotation (COR) by a second gas beam which is formed in the collision chamber. Although it may be less sensitive, this apparatus is somewhat similar to the universal detector molecular beam apparatus described in Ref. 1.

The design of this apparatus was guided by three considerations. In order to maximize the scattered intensity, the apparatus was designed so as to minimize distances between the oven slits and the COR and also the distance between the COR and the detector without the sacrifice of an ultimate scan region of the detector. On the other hand, since the

molecular beam experiments are "not all a matter of intensity," the technique of beam modulation and phase-sensitive detection is provided to allow the discrimination against background. As a second consideration it was designed to avoid the so-called viewing factor[2] by insuring that the detector could see the entire collision zone at various scan angles. With these design considerations in mind, the defining slits associated with each oven and the detector were carefully chosen. Finally, the achievement of a flexibility to allow for future modification or substitution of components was also considered.

Figure 1 shows the general schematic of apparatus configuration. The description of the apparatus presented here will concentrate on the features of the two beam sources and the vacuum chambers housing them. A detailed discussion of the detection chamber and its associated components is given in Ref. 3. Lists of the mechanical and electrical drawings for this apparatus, with the exception of those pertaining to the detector, are given in Appendix A and B respectively.

B. Vacuum System

To ensure that the molecules in the beams suffer no collision with the ambient background gas, a sufficiently low pressure is required; it is provided by the high pumping speed of oil diffusion pump and liquid nitrogen cold trap. However, because of the excess residual gas resulting from housing the gas source oven in the collision chamber, the studies reported in this thesis have been limited to reactions with gases which are either condensable or moderately condensable at liquid

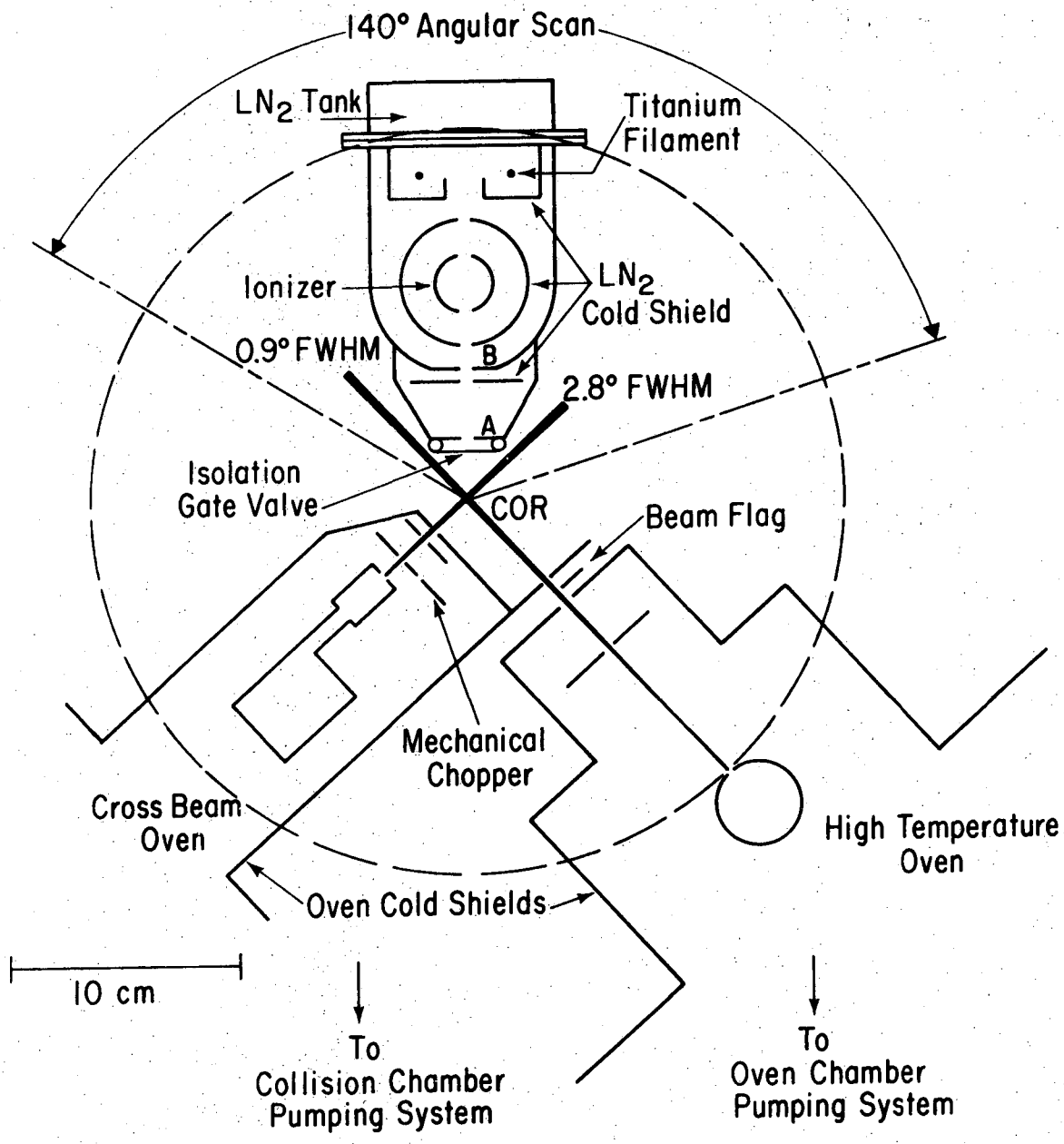

Fig. 1. Schematic diagram of experimental arrangement, as viewed from above. The reactant beams, which cross at an angle of 90°, effuse from the ovens located in separate chambers. The detector, mounted on a platform indicated by the dashed circle, can be scanned from -20° to +120° with respect to the stationary alkaline earth beam.

nitrogen temperature. Figure 2 shows a block diagram of all pumping components associated with each vacuum chamber; notice that the detection chamber, which is mounted by means of a rotatable seal on the top of collision chamber with its bottom half extending into the collision chamber, is also shown in the figure.

1. Vacuum Chambers

The collision chamber and the high temperature oven chamber were constructed as large rectangular boxes with sizes 70 cm × 45 cm × 72 cm and 69 cm × 42 cm × 64 cm respectively. The main bodies of both vacuum chambers consist of flat top and bottom plates connected by vertical supports at each corner; they were fabricated from an aluminum alloy (Alcoa-6061), using welded construction throughout. Three side walls on each chamber were fabricated from the same aluminum alloy plates. These walls are 1.9 cm thick and are bolted onto the chambers by means of bolt holes drilled and tapped directly into the frames of each chamber. The two chambers are joined by means of a copper partition with a small rectangular hole (1.0 cm × 0.6 cm) through which the alkaline earth beam passes. The advantages of this construction method are pointed out in Ref. 2. Thus, removal of any side wall provides a large opening and convenient access into the chambers; the walls themselves are relatively inexpensive to fabricate and furnish flat surfaces for mounting accessory components by means of bolt holes tapped directly into the walls. The detection chamber, which was fabricated from #304 stainless steel and supported by a Kaydon 12 in. diameter bearing (KC 120 × P) which seated in a counter-bored hole in the top

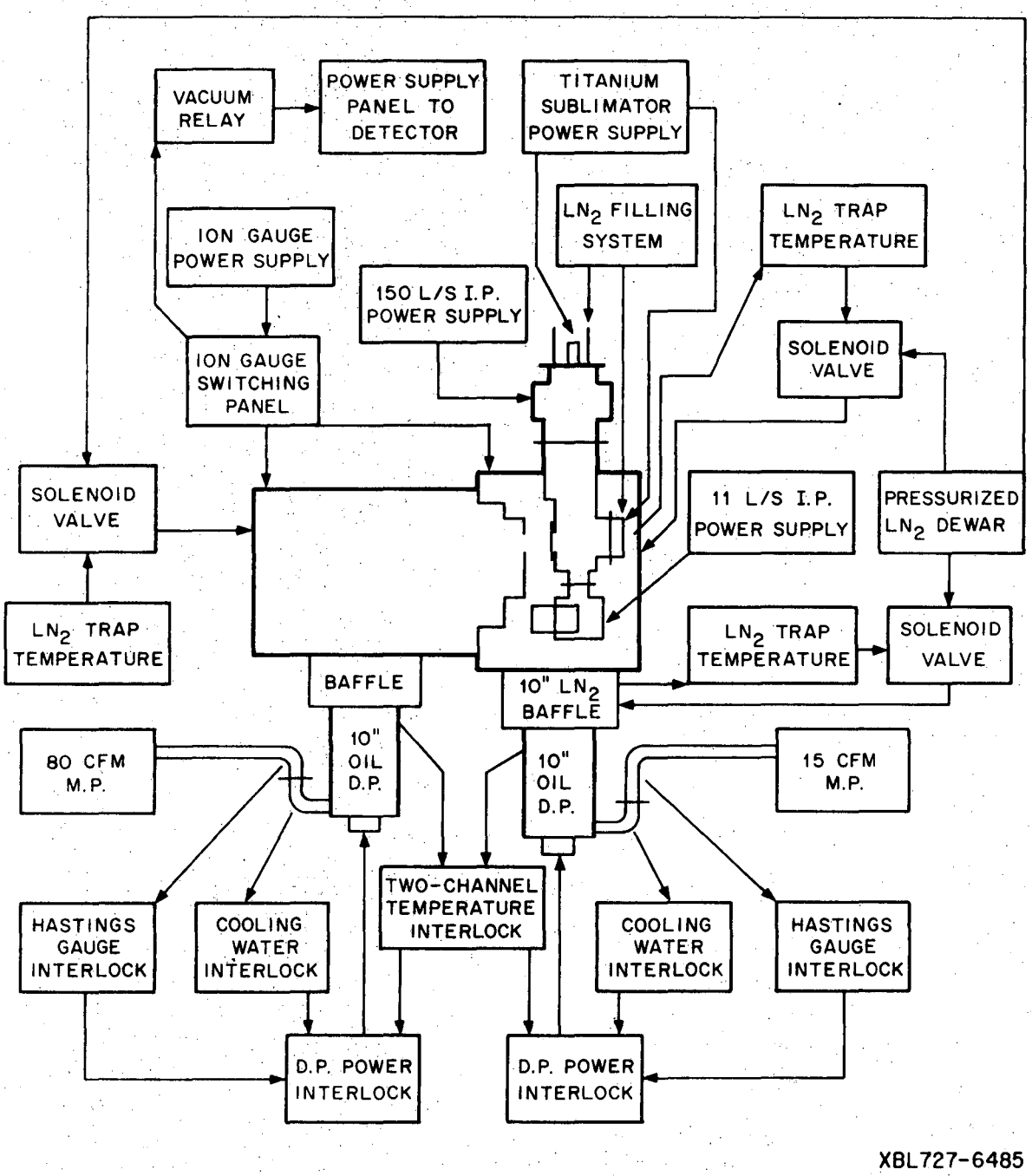

Fig. 2. Vacuum chambers and associated pumping components.

of the collision chamber, may be rotated from outside the chamber while maintaining high vacuum inside.

2. Pumps and Cold Traps

Each chamber is pumped by a Consolidated Vacuum Corporation PMC-10C, 10 in. oil diffusion pump with nominal pumping speed for air of 4300 l/s; these pumps are mounted beneath the chambers. Dow Corning DC704 silicone fluid is used as pump oil; this fluid has the characteristics of low ultimate pressure and high resistance to decomposition. Two aluminum tanks with capacities of 21 liters and 17 liters are housed inside of the collision chamber and the high temperature oven chamber respectively to serve as liquid nitrogen reservoirs. Each tank covers the entire bottom of the chamber, except for a 10 in. diameter hole through each tank which is immediately above the diffusion pump opening. A diffusion pump baffle was bolted onto each of these holes; these baffles were designed to prevent the backstreaming of pump oil into the chamber, at the sacrifice of about 50% of the diffusion pump speed. Copper boxes with removable walls, which were nickel plated, were firmly bolted to each aluminum tank. Clearances of ~ 1.5 cm were provided between the inner walls of the vacuum chambers and the outer walls of these copper boxes, so that each vacuum chamber enclosed an inner chamber which was effectively cooled by liquid nitrogen, thereby providing extensive cryogenic pumping for condensable vapors. These aluminum tanks are supported by thin stainless steel straps, so as to thermally isolate them from the outer vacuum chambers. A standard 1 in. swedgelock fitting is used to couple a liquid nitrogen filling tube to each aluminum

reservoir. They are filled automatically by means of a thermostat interlocked with a solenoid valve equipped on a pressurized dewar. A Kinney KC-15 double-stage mechanical pump served as the forepump for the collision chamber. Realizing that the halogen molecules and other highly reactive gases employed as beam material in these studies may attack the mechanical pump, a liquid nitrogen cold trap was inserted between the diffusion pump and the forepump; it was periodically cleaned while the diffusion pump was idle.

As it was originally designed as an F-Atom source chamber, an extra baffle which would contain hot sodium chloride crystal was also inserted between the high temperature oven chamber and its diffusion pump; this baffle was to convert the very destructive F_2 gas into Cl_2 gas so as to minimize the damage to the pump. This baffle has remained in the system without the hot sodium chloride crystal for the experiments reported in this thesis. A Kinney KDH-80 single-stage mechanical pump served as the forepump for this high temperature oven chamber. Here again, the mechanical pump was protected by a liquid nitrogen cold trap, which was periodically cleaned.

The early attempts to study alkaline earth reactions failed, because of the existence of a high background noise level extending over a broad mass range; it seemed likely that this was mainly due to residual gases (notably diffusion pump oil) which entered the detection chamber when the machine was allowed to warm up. Accordingly, a Consolidated Corporation BCN-101B, 10 in. liquid nitrogen cooled baffle, was then placed above the diffusion pump in the collision chamber and

a small motor-driven gatevalve was also added to make possible isolation of the detection chamber when experiments were not in progress. This resulted in a very significant reduction of the background mass spectrum and made possible the experiments reported in this thesis.

3. Pressure Gauges

The Hastings thermocouple vacuum gauges are used independently to monitor the pressures in the forepump systems for each chamber; they control the interlocks which in turn shut off the diffusion pump power whenever the pressure exceeds a preset value and reset themselves to turn the power on once the pressure sufficiently decreases. The diffusion pump power is also interlocked to the cooling water flow rate and to the pump temperature. The pressure in each chamber is monitored by Veeco RG-75 ionization gauges. An ionization gauge switching panel is used to read either gauge with one power supply; a vacuum relay is also provided to automatically turn off the power supply of the detector electronics if the pressure in the collision chamber drastically increases.

The pressure observed in these chambers was typically maintained at $1\text{-}2 \times 10^{-6}$ torr in the collision chamber and in the high temperature oven chamber and at $\sim 2 \times 10^{-8}$ torr in the detection chamber while running an experiment. After an initial outgassing period, much lower pressures (by a factor of ~ 10) could be achieved in the absence of molecular beams.

The power supply for the Hastings gauges, the ion gauges, the diffusion pump interlocks and the automatic liquid nitrogen filling

system were all designed and constructed by the Lawrence Berkeley Laboratory.

4. Vacuum Seals and Connections

Rectangular rubber gaskets are used to seal all side flanges of each chamber, while rubber O-rings and Viton O-rings in grooves of standard LBL dimensions are used in other static seals. The moveable seal for the 12 in. diameter rotating lid to which the detection chember was welded is provided by a double O-ring grooves with a pump-out ring between the grooves; however, this pump out provision was not necessary during the expeniments reported here. All gaskets and O-rings are greased lightly with Apiezon L and N vacuum grease except those on the rotating seal where Dow Corning 33, a medium consistency, heat stable low temperature silicone grease is used because of its lower viscosity.

Electrical feed-throughs to these two source chambers are all made by either (1) drilling holes in epoxy plugs, threading a bare wire through the hole and sealing with epoxy, or (2) using stupakoff kovar-glass seals. Inside the vacuum chambers, connections for the cooling water lines and liquid nitrogen system were made of swedgelock fittings; although no trouble has been encountered with water lines, relatively rare (~ a few a year) leakes have developed in the liquid nitrogen systems.

C. Beam Sources

In constrast to alkali metals, there is negligible equilibrium concentration of alkaline earth dimers[4] in the vapor phase at the temperatures and pressures employed here. Thus a standard double chamber oven[2] commonly used for producing alkali atom beams is not necessary for the alkaline earth beams. The block diagram shown in Fig. 3 illustrates the general schematic for the oven system and its power supplies.

1. High Temperature Oven

The alkaline earth beam is produced by a direct resistance-heated oven. There are certain advantages in favor of this type of oven. First, because it can sustain high power input, a very high operating temperature can be reached within a short period of time so that a steady beam can be immediately achieved. Second, it can be designed and constructed easily to hold a relatively large quantity of alkaline earths at each loading, thereby reducing the frequency of oven recharges (a time consuming procedure). A third advantage is that it typically provides a more reliable performance than wire-wound oven because the commonly used tantalum heating wire usually becomes brittle after repeatedly heatings at high temperature.

The oven is made of two stainless steel cylinders; the smaller cylinder, which is charged with the alkaline earths, has a capacity of $\sim 65\ cm^3$, while the larger cylinder, enclosing the former, has a thin wall of 0.04 cm and is 16.4 cm long × 3.8 cm O.D. Electrical insulation between the inner and outer cylinders is provided by ceramic spacers. The oven is heated by passing an AC current of ~ 400 amperes at ~ 3 volts

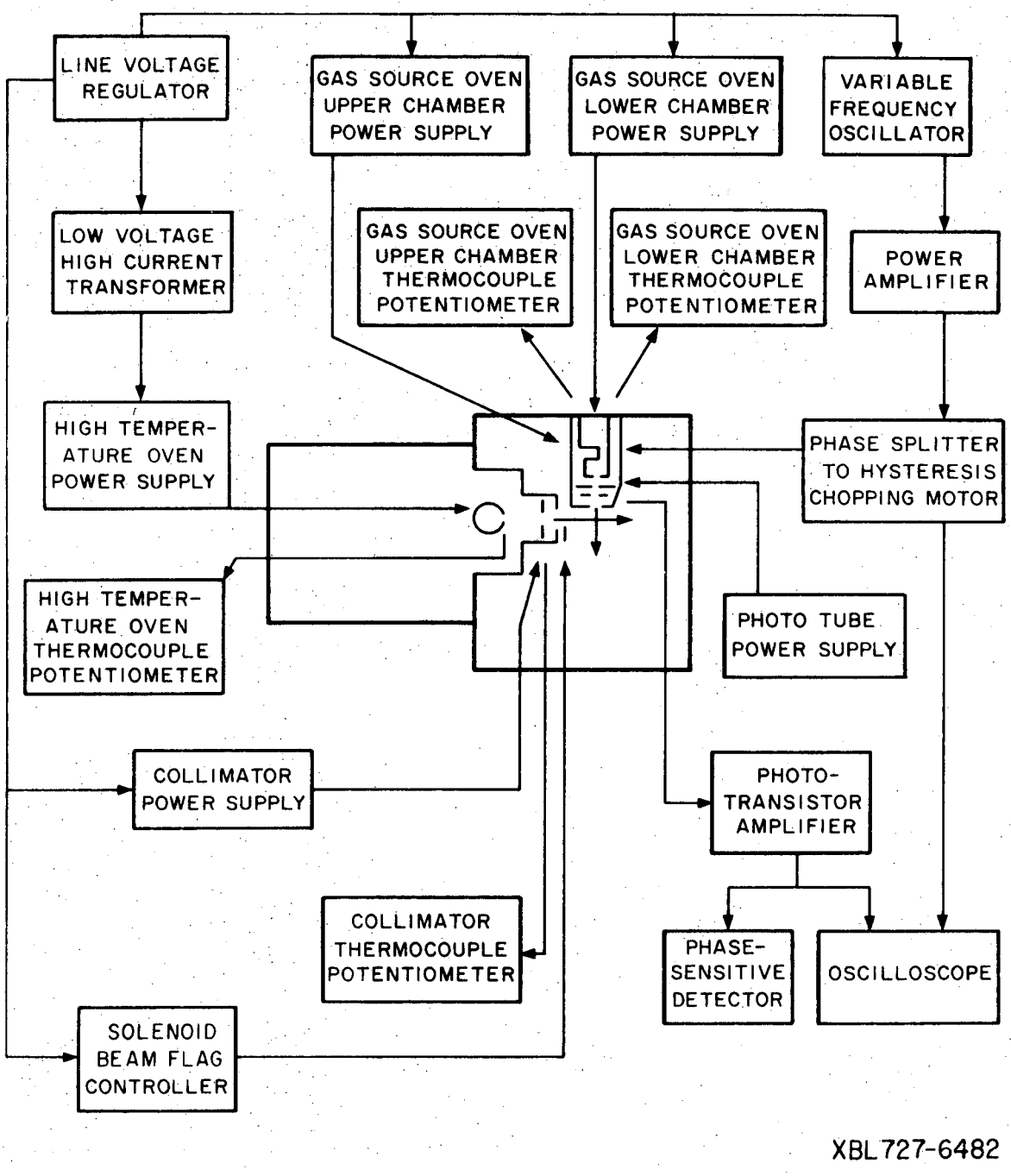

Fig. 3. Block diagram of oven system and its power supplies.

through the outer cylinder whose resistence at room temperature is 2.5×10^{-3} ohm, for a temperature of approximately 1000°K and the inner cylinder attains the same temperature by radiant heating; it took about 10 minutes to register a steady temperature when the oven was previously heated to a temperature typically ~ 200°K below the operating temperature. The power supply for this oven was constructed by the Lawrence Berkeley Laboratory to give a maximum output of 600 amperes and 10 volts. A chromel-alumel thermocouple is used to monitor the oven temperature. In constrast to the molybdenum oven employed in Ref. 5, the stainless steel oven used here was relatively easy to fabricate; no evidence has been found thus far that alkaline earth atoms attack stainless steel at the temperatures employed. Moreover, this oven has a much bigger capacity; it makes possible operation for ~ 80 hours at ~ 0.3 - ~ 0.5 torr after each loading. An attempt to use a graphite oven in early studies failed because of the poor strength of the graphite thin wall (~ 0.12 cm).

In order to reach the desired high temperature, the outer cylinder was polished to reduce its emissivity and several layers of stainless steel foil were used to surround the entire oven as heat shields to further reduce heat loss through radiation. An improvement was found when carbon cloth was inserted between each layer of stainless steel foil.

The oven current is supplied by water-cooled copper blocks which secure the outer cylinder at the top and bottom. The oven is firmly tighted to the top copper block, but is not bolted to the lower block so as to avoid possible strains due to thermal expansion. Good electrical

contact with the bottom copper block is achieved by allowing the bottom of the oven to "float in a pool" of indium metal which is contained in a hole in the bottom copper block. No evidence for vaporization of this indium "solder" has been observed. Figure 4 shows the oven assembly and its elements. The position of the oven slit is guided by a ceramic wafer. The inner and outer cylinders are electrically insulated by ceramic guides as well.

Typical operating temperatures ranged from 820°K for Mg to 1060°K for Ba, corresponding to a source pressure of ~ 0.3 torr in both cases, as interpolated from the tabulated values given in Ref. 6. These beams are produced from a knife-edge slit whose width is comparable to the mean free path within the source and thus considered to be characterized by the molecular effusion.[7] The actual beam velocity distribution has been measured for Ba and is discussed in a later section.

A collimator of adjustable slit width mounted on the top copper block provides collimation for the beam; it is separately heated by a 0.020 in. tantalum wire strung with ceramic beads and wound through holes in the collimator plate from a 110 v AC variac to a temperature typically 50°K higher than oven temperature. A solenoid controlled beam flag, used to intercept the beam path, is mounted on the copper partition between two chambers: the collision chamber and the high temperature oven chamber.

2. Gas Source Oven

The gas source oven was designed as a two-chamber oven so as to permit the use of beam materials with vapor pressure less than 1 torr

Fig. 4. Components of high temperature oven and its assembly.

A. Water-cooled high current low voltage terminals. These are fabricated from copper plates; the top copper block is used to support the entire oven
B. Stainless steel alkaline earth crucible
C. Stainless steel direct resistance-heated oven
D. Quartz
E. Carbon cloth
F. Stainless steel foil
G. Indium pool for electrical contact

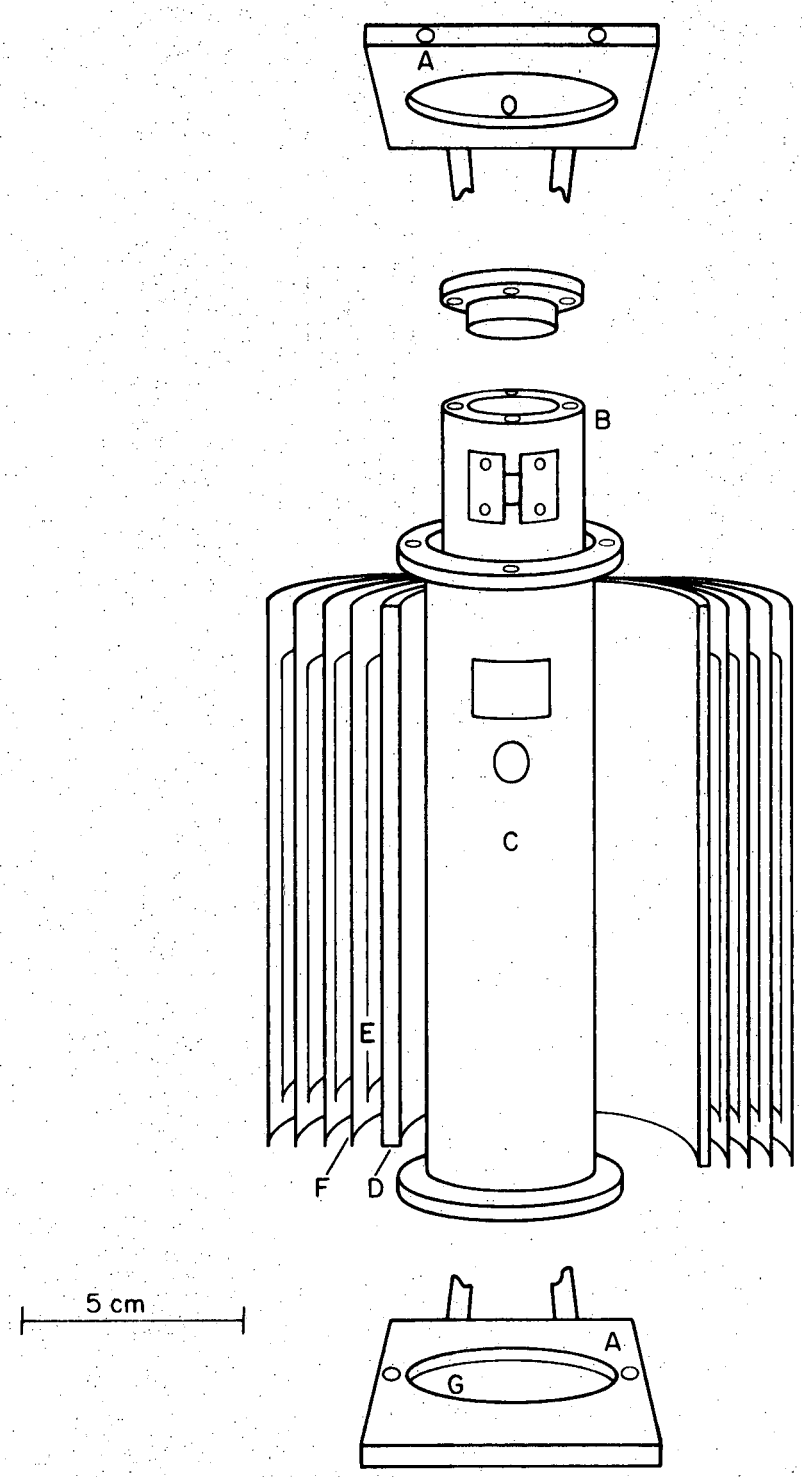

XBL 727-6481

Fig. 4.

at room temperature. However, all experiments were conducted with secondary beam of materials with a vapor pressure exceeding 1 torr at room temperature so that the vapors were prepared on an external gas line at the desired pressure. In this case, the gas was admitted to the lower oven chamber through a stainless tube, and both oven chambers were maintained at the same temperature. The desired pressure of a crossed beam gas, typically about 3 torr, is prepared on the external vacuum line by either using a barostat temperature bath or a slush bath if it is in the liquid phase at room temperature or by means of a Granville-Phillips variable leak valve in the case that the substance is gaseous at room temperature. The slush bath is prepared by slowly adding liquid nitrogen to a dewar, in which the proper organic solvent was previously added, while constantly stirring until the consistancy of a thick malted milk is achieved. Appendix C lists the organic solvents used in the slush bath for various ranges of temperatures. The barostat temperature bath is simply a mixture of acetone and dry ice. The desired vapor pressure is achieved by placing the sample in a inner flask, winding this flask with heating wires, and isolating the heating wires from the acetone-dry ice mixture by means of a concentric outer flask. The pressure of the crossed beam gas was measured by means of a Datametrics manometer at the external gas line.

The oven, made of stainless steel, is equipped with a multichannel source array. The oven construction is similar to the double chamber oven used in producing the Li atom beam in Ref. 2. The standard "crinkly foil" many channel array was constructed by alternatively

stacking layers of flat and 0.01 cm wide corrugated stainless steel foil (0.0025 cm foil thickness). The two chamber oven is heated by 0.020 in. tantalum wires strung with ceramic beads and wound through holes in the oven; the wires are energized by 110 v AC variac. The temperatures of the two chambers were measured with chromel-alumel thermocouples and typically maintained at 340°K and 320°K in the upper and lower chambers respectively.

A mechanical chopper which is partitioned between the oven slit and the collimator slit so as to square-wave modulate the crossed beam. The chopper is a three bladed disk and is indirectly driven by a Globe two phase synchronous-hysteresis motor by means of a pinion gear linkage. With this construction, the crossed beam can be modulated at very low chopping frequencies, ~ 10 Hz, so that a lock-in-amplifier with long time constant may be used to improve the signal-to-noise ratio. A light source and a phototransistor are provided to pick off the reference signal for the PAR HR-8 lock-in-amplifier employed in the detection system. The chopping frequency used in most experiments reported here was typically maintained at ~ 41 Hz and the crossed beam was 100% chopped at this frequency.

The entire oven is surrounded by a copper box with an open end at the bottom. This box is cooled by liquid nitrogen to condense the crossed beam molecules which are intercepted by the chopper and the collimator. In order to maintain the sufficiently low pressure in the collision chamber, this cooling system was important.

D. Beam Profiles, Velocity Distributions, and Product Intensities

Table I gives the dimensions that characterize the beam geometries and the detector resolution. These dimensions were carefully chosen so that the viewing factor, which is defined[2] as the fraction of the collision zone seen by the detector at various scan angle, was essentially unity at all viewing angles. Theoretical viewing factor calculations for the apparatus geometry employed in these studies are presented in Ref. 3.

The beam profiles of 0.9° FWHM and 2.8° FWHM for alkaline earth atom beam and gas beam respectively, which are shown on Fig. 1, are calculated from the oven and collimator slit geometries. However, two corrections are of important before comparing with experimentally measured beam profiles. First, the finite width of the detector has to be considered. Second, since the detector is pivoted about the COR, the beam profiles measured experimentally are referred to this origin rather than an origin situated at the oven slit. When these considerations are included, the resultant beam profiles are 3.2° FWHM for alkaline earth beam and 5.1° FWHM for gas beam. The measured profiles at low electron emission are 3° FWHM and 4° FWHM for the alkaline earth beam and gas beam respectively. The agreement for the alkaline earth beam is fairly good; however, the measured beam profile is narrower than the calculated value for the gas beam. This disagreement is likely to be due to a nozzle effect in the "crinkly foil" multichannel source array, since this multichannel source array may have a certain collimating effect. It should be remarked that the measurements of

Table I. Geometry of Beam Alignment[a]

Elements		Height	Width	Length[b]
High Temperature Oven	Oven Slit	0.48	0.051	17.1
	Collimator	0.71	0.11	9.5
Gas Source Oven	Oven Slit	0.71	0.16	5.1
	Collimator	0.71	0.079	2.5
Detector	Front slits, A	0.95	0.206	2.5
	Rear slits, B	0.41	0.051	6.3

[a] Dimension is given in cm.

[b] Length is the distance measured from COR.

beam profiles, at least the gas beam, had to be conducted at low electron emission[3] ($\lesssim$ 1 ma) to avoid saturation of the ionizer by the highly intense beam.

Since experiments are carried out by employing two beams with full velocity distributions, it should be important to know the actual beam velocity distributions. In theory, molecules which effuse from an orifice should suffer no collision after they emerge from the oven; thus, from the beam source pressures and slits widths used here, one might expect that the alkaline earth beam would retain the thermal velocity distribution and the beam intensity and geometry characteristic of an effusive source.[7] On the other hand, since a "crinkly foil" multichannel source array is used to produce the gas beam, it is very likely that this gas beam may have a non-thermal distribution under the experimental conditions. Other workers[8,9] have reported a non-thermal distribution for a beam source similar to the multichannel source employed in this study. A small, slotted cylindrical velocity selector[3] was thus designed to measure the actual beam velocity distributions.

Due to the limitation of space and background noise, the velocity distribution of the alkaline earth beam was measured for Ba atoms only; a slight deviation from a thermal distribution at the low speed portion was observed at the typical operating temperature 1030 ~ 1120°K (corresponding to 0.2 - 1.0 torr source pressure). A number of reports[10,11] have shown a similar result; it has been attributed to the collisions within the beam in the immediate vicinity of the oven slit. Velocity measurements for crossed beam were conducted for a number of gases.

Empirically, these measured number density speed distributions, including those of the Ba beam, are all fitted by

$$f(v) = (v-v_s)^2 \exp[-(v-v_s)^2/\alpha^2]; \quad v > v_s \qquad (1)$$

$$= 0 \qquad v \leq v_s$$

Here, v_s is a flow speed which increases with increasing source pressure. For the gas beam, α is the most probable thermal source speed which is independent of source pressure, i.e., $\alpha = (2kT/m)^{1/2}$. Thus, the gas beam velocity distributions maintain the breadth characteristic of a thermal distribution, but are displaced to higher speeds with increasing source pressures. For the Ba beam, however, α is a function of source pressure; detailed discussion will be found in Ref. 3. Table II lists the pressure dependence of flow speed for a number of gases.

Although the overall detector sensitivity is not directly calculable, it may be roughly calibrated by comparing the measured umbra intensity of the alkaline earth beam with the predicted intensity calculated from molecular effusion. The umbra Ba beam intensity may be evaluated for the apparatus geometry given in Table I as $\sim 6 \times 10^{12}$ atoms/sec; this would correspond to a current of $\sim 1 \times 10^{-6}$ amp if the overall detection gain were unity. The measured umbra Ba intensity is 3×10^{-7} amp at 2.4 KV applied to the electron multiplier. From the measured electron multiplier gain, 1.5 per 100 volts increment from 2.4 Kv up to 3 Kv, this is equivalent to 3.5×10^{-6} amp at 3 Kv where the product signal was measured, or an overall gain of 3.5 for the detector. We can now proceed to calculate the expected intensity of scattered product BaBr

Table II. Flow speed of gas beam.[a]

Br_2	P	0.53	0.80	1.40	2.50	3.50
	v_s	0.56	0.75	1.10	1.32	1.4
Cl_2	P	0.41	0.74	1.60	3.60	
	v_s	0.55	1.00	1.58	2.00	
$C Cl_4$	P	0.45	0.72	1.7	3.6	
	v_s	0.71	1.04	1.54	1.65	
CH_3I	P	0.44	1.25	2.5		
	v_s	0.6	1.25	1.5		
CH_2I_2	P	0.60				
	v_s	0.67				

[a]Pressure is given in torr and speed in 100 m/sec.

from a prototype reaction of Ba + Br_2. We know that for two gaseous species with uniform number densities N_{Ba} and N_{Br_2} in an intersection volume V, moving toward each other with relative velcity v_r, and with reaction cross section $Q(v_r)$, the rate of forming reaction product will be given by

$$R = N_{Ba} N_{Br_2} v_r \, Q(v_r) \, V. \qquad (2)$$

We estimate $N_{Ba} = 1.5 \times 10^{10}$ cm^{-3} and $N_{Br_2} = 7.7 \times 10^{12}$ cm^{-3} in an intersection volume of approximately 0.036 cm^3; the relative velocity was estimated to be 4.2×10^4 cm/sec for these two beams intersecting at 90° and the temperatures employed. The reaction cross section was estimated as ~ 150 $Å^2$, as this is the value accepted[12] for the analogous Na + Cl_2 reaction; it may be a factor of two too high, as Jonah and Zare[13] reported ~ 60 $Å^2$ for the Ba + Cl_2 reaction.

Substituting these estimated values into Eq. 2, we obtained ~ 2.5×10^{12} sec^{-1} as the formation rate of BaBr at the COR. As shown in Fig. 1, the detector is characterized by the rear slit (slit B) with a cross section area 0.021 cm^2. All molecules travelling through the rear slit will reach the ionization zone and be detected; thus, the detector subtends a solid angle of ~ 5.3×10^{-4} Sr. Assuming an isotropic scattered BaBr angular distribution, we expect the BaBr signal at the detector as to be ~ 1.3×10^9 sec^{-1}. If the detector has the same overall gain for Ba as well as BaBr, the calculated intensity would be ~ 7×10^{-10} amp, in reasonable agreement with the measured value of ~ 5×10^{-10} amp at the peak of measured angular distribution.

Finally, the potential effect of background scattering deserves some comments here. The background scattering has the larger effect on the alkaline earth beam and results in an attenuation of the beam intensity as well as a broadening of the beam profile. In this latter case, the correction for viewing factor could become important. Measurements of the dependence of the Ba beam intensity indicated that a $\sim$ 7% reduction of beam intensity occurred when the pressure in the collision chamber rose from 1×10^{-6} torr to 3×10^{-6} torr; this attenuation increased to almost 30% at 1×10^{-5} torr background pressure. These figures are considerably higher than the attenuation of the alkaline earth beam by the secondary gas beam (typically $\sim$ 5%). Except were noted, all reactive scattering angular distributions were measured for background pressures $\lesssim 1 \times 10^{-6}$ torr so that this pressure attenuation factor was negligible.

REFERENCES

1. Y. T. Lee, J. D. McDonald, P. R. LeBreton, and D. R. Herschbach, Rev. Sci. Inst. 40, 1402 (1969).
2. D. D. Parrish, Ph. D. thesis, University of California, Berkeley, Calif. (1970).
3. C. A. Mims, Ph. D. thesis, University of California, Berkeley, Calif. (1972).
4. (a) W. C. Stwally, Chem. Phys. Letter 7, 600 (1970).
   (b) W. J. Balfour, and A. E. Douglas, Can. J. Phys. 48, 901 (1970).
   (c) R. H. Ewing and A. M. Mellor, J. Chem. Phys. 53, 2983 (1970).
5. (a) C. D. Jonah, R. N. Zare and Ch. Ottinger, J. Chem. Phys. 56, 263 (1972). (b) In a private communication, one of the authors (RNZ) commented that their molybdenum oven had a capacity to hold barium metal for only about 2 hours in operation.
6. J. L. Margrave, The Characterization of High Temperature Vapors. (John Wiley and Sons, Inc. N.Y. 1967). Table A.1 and Figures A.1, Sheet A, B, and C.
7. N. F. Ramsey, Molecular Beams. (Oxford University Press, London, 1963).
8. (a) D. R. Olander, R. H. Jones, and W. J. Siekhaus, J. App. Phys. 41, 4388 (1970); (b) W. J. Siekhaus, R. H. Jones, and D. R. Olander J. App. Phys. 41, 4392 (1970).
9. N. C. Blais and J. B. Cross, J. Chem. Phys. 52, 3580 (1970).
10. I. Estermann, O. C. Simpson, and O. Stern, Phys. Rev. 71, 238 (1947).
11. G. H. Kwei, UCRL-11966, Lawrence Berkeley Laboratory, Berkeley, Calif., 1965.

12. A. F. Trotmann-Dickenson and G. S. Milne, NSRDS-NBS 9 (1967).

13. C. D. Jonah and R. N. Zare, Chem. Phys. Letters 9, 65 (1971).

APPENDIX A

List of Apparatus Mechanical Drawings and LBL Numbers*

1. Vacuum chambers

A. Collision chamber

main chamber	12N	2746
side flanges (2)	12N	2833
back flange	12N	2843
liquid nitrogen reservoir	12N	2804
liquid nitrogen shield chassis	12N	2784
liquid nitrogen fill tube	12N	2913
side flange liquid nitrogen shields (2)	12N	2863
back flange liquid nitrogen shield	12N	2823
oil diffusion pump baffle (2)	12N	2962
ion gauge flange	12N	2952
chamber support stand	12N	2933
adapter to high temperature oven chamber	12N	2764

B. High temperature oven chamber

main chamber	12N	2754
side flanges (2)	12N	2923
back flange	12N	2794
liquid nitrogen fill flange	12N	2903
liquid nitrogen reservoir	12N	2943
liquid nitrogen shield chassis	12N	2774

*These drawings are filed at the Lawrence Berkeley Laboratory; copies of LBL drawings whose numbers are cited here may be obtained by writing to Lawrence Berkeley Laboratory, Technical Information, Bldg. 90, Rm 3118, Berkeley, Calif. 94720.

side flange liquid nitrogen shields (2)	12N	2893
back flange liquid nitrogen shield	12N	2883
adapter to collision chamber	12N	3812
flange to adapter	12N	3153
pump baffle	12N	2853
chamber support stand	12N	2873
corrosive gas exchanger	12N	3193
liquid nitrogen cold traps (2)	12N	3203

2. Ovens

high temperature oven	12N	4693
oven support copper blocks	12N	4682
ceramic adaptor	12N	4672
gas source oven	12N	3162

APPENDIX B

List of Apparatus Electronic Diagrams and LBL Numbers

System wiring diagram	8S 8405
Dual liquid nitrogen level control	8S 7252
Single vacuum interlock (2)	8S 2803-1A
Hastings gauge dual vacuum interlock	6z 4664E
Hastings gauge dual vacuum interlock	5z 4994-1D
Ion gauge 5 position switching panel	8S 7392
High temperature oven power supply	8S 7351

APPENDIX C

Slush Bath

Beam Materials	Solvents	Temperature, °C
CH_2I_2, ICl, $SnCl_4$, IBr	ice-water*	0 to 20
2-nitropropane, tert-butanol		
I_2, C_2Cl_4, CCl_3Br, CCl_3NO_2		
S_2Cl_2		
CH_2ClBr, CH_2Br_2, iso-amyl nitrite	ice-brine*	0 to -20
Br_2, CCl_4, PCl_3	Carbon tetrachloride	-22.9
$SiCl_4$	ethylene dichloride	-35.6
CH_3I	n-hexanol	-48.0
NOCl	dry ice-acetone*	-78.5
-	methanol	-97.8
-	carbon disulfide	-111.6

*It is simply a mixture of two solvents.

III. REACTIONS OF ALKALINE EARTH ATOMS WITH Br_2 AND Cl_2

A. Introduction

The main subject in the development of crossed molecular beam studies during the past few years has appeared to be either the elucidation of more detailed information of the reaction dynamics of a few simple alkali atom reactions by refining the crossed beam apparatus, or else a "chemical scanning" of the reaction dynamics of various non-alkali atom reactions by means of a suitable mass spectrometer detector. In particular, the introduction of the electron bombardment ionizer-mass spectrometer detector has brought the chemical scope of crossed beam studies of neutral reactions into a new era beyond the "alkali age." This has prompted a number of studies of the halogen atom,[1] the hydrogen atom,[2] and the alkaline earth atom[3] reactions. The present chapter reports results on the reactions of Ba, Sr, Ca, and Mg with Br_2 and Cl_2.

By observing the chemiluminescent spectrum of Ba and Sr reacting with Cl_2, Jonah and Zare[4] showed that both monochloride and dichloride products were responsible for the light emission and the reaction cross section for the formation of BaCl was estimated to be 60 $Å^2$. In this work, we have measured product laboratory (LAB) angular distributions, via an electron-impact ionization process, by crossing two beams with full velocity distributions. Only monohalide ion (MeX^+) mass spectrometer signals are observed in any of these reactions; these peak near the atomic beam direction in the LAB angular distribution. The predominant product for these reactions is considered to be the

monohalide on the basis of an analysis of the angular distributions.

Although alkaline earth monohalides have been known for many years, many of their physical and chemical properties are still uncertain. Recently, however, there has been a growing interest in the study of bond dissociation energies of alkaline earth monofluorides and monochlorides by either mass spectrometry[5] or flame emission.[6] These experimental results are in fairly good agreement with the values evaluated from the Rittner ionic model; thus, Hildenbrand[5a] indicated that an ionic model is likely applicable to BaCl, SrCl, and perhaps to CaCl.

B. Experimental Conditions

As described in a previous chapter, the apparatus used in these experiments consists of three distinct vacuum chambers; the first two chambers act as the alkaline earth atom source chamber ($\sim 2 \times 10^{-6}$ torr) and the collision chamber ($<2 \times 10^{-6}$ torr); this latter chamber also houses the halogen beam source. The two beams are crossed at an angle of 90° with their full velocity distributions. The atom beam is formed by thermal effusion from a resistance-heated oven source with a standard knife-edge slits; the halogen gas is prepared on an external gas line and is chopped at a low frequency ($\sim$ 41 Hz) after emerging from a "crinkly foil" multichannel source array. Table I summarizes the experimental conditions.

The angular distributions of reactive products are measured by means of an electron impact ionizer-massfilter detector and are recorded on a PAR HR-8 lock-in-amplifier referenced to the halogen beam chopping

Table I. Experimental conditions.[a]

System	alkaline earth atom beam				Halogen molecule beam		
	source conditions		speed	distribution[c]	source conditions		flow speed
	T	P^b	α	v_s	T	P	v_s[c]
Br_2 + Ba	1060	0.35	3.1	1.1	340	4-5	1.4
Sr	960	0.4	3.7	1.3	340	2.5-3.3	1.4
Ca	1020	0.3	5.8	1.9	350	3-4	1.4
Mg	820	0.28	6.7	2.2	340	~ 4	1.4
Cl_2 + Ba	1050	0.32	3.1	1.1	340	2	1.7
Sr	960	0.4	3.7	1.3	330	~ 4	2.0
Ca	1010	0.28	5.8	1.9	360	3.0-3.5	2.0
Mg	820	0.28	6.7	2.2	340	2-4	1.7-2.0

[a] Temperature is given in °K, pressure in Torr, and speed in 100 m/sec.

[b] Vapor pressure of alkaline earths is taken from J. L. Margrave, Characterization of High Temperature Vapor. (John Wiley and Sons, Inc. N.Y. 1967), Table A.1 and Figures A.1, sheet A, B, and C.

[c] These values are obtained from the measured beam velocity distributions (see section 4 of previous chapter and Ref. 13).

frequency. These detection elements are housed in a differentially pumped UHV chamber ($< 2 \times 10^{-8}$ torr) which is rotatable in a plane defined by the two intersecting beams. The use of an electron bombardment ionizer detector makes it necessary to consider the fragmentation pattern of the product ion formed in the ionizer. The possible products of the Me + X_2 reactions studied here are MeX_2 or MeX + X. Because X_2 molecule itself produces an X^+ signal upon electron impact, it was impossible to study this family of reactions by monitoring the X^+ mass spectrometer signal. Thus, all of the product angular distribution measurements reported here were obtained with the mass spectrometer tuned to the MeX^+ signal. Although the neutral precursor of this ion might be either MeX or MeX_2, careful mass scans were made for some of these reactions (notably Ba and Mg with Cl_2 and Br_2) but no scattered signals have been observed at the MeX_2^+ mass peaks. Arguments presented in a later section indicate that the MeX^+ signal arose predominately (if not exclusively) from the ionization of MeX rather than MeX_2.

C. Results and Data Analysis

The main object in the beam experiment is to determine the direction and magnitude of the recoil velocity that carries the products away in the CM coordinate system, thereby providing the necessary information for insight into the reaction dynamics. This implies that we have to transform our measured product LAB angular distributions to the CM coordinate system where the restrictions imposed by the conservation laws make it possible to infer the final relative translational energy

of the products as well as the directions in which they recoil.

Since our measured product LAB intensity is limited to a plane defined by two intersecting beams, the LAB intensity, $I_{LAB}(\Theta)$, may be explicitly expressed as

$$I_{LAB}(\Theta) = \int_0^\infty \int_0^\infty \int_0^\infty I_{LAB}(\Theta,v)\ f(v_1)\ f(v_2)\ dv_1\ dv_2\ dv \qquad (1)$$

where $f(v_i)\ dv_i$ is beam number density velocity distribution and v is the product LAB velocity at a given angle, Θ. In this expression, $I_{LAB}(\Theta,v)$ is directly related to the CM differential cross section $Q(\theta,u,V)$ as

$$I_{LAB}\ (\Theta,v) = VQ(\theta,u,V)\ \frac{v}{u^2} \qquad (2)$$

where V is the initial relative velocity and u is the product velocity in the CM coordinate system. Since the product LAB intensity measured from an electron bombardment detector is a number density distribution and since flux density but not number density is conserved in the transformation between two coordinate systems, one power of v has been removed from the Jacobian factor in the above expression. Thus, in favorable cases the CM differential cross section, $Q(\theta,u,V)$, may be accurately determined from the measured quantity $I_{LAB}(\Theta)$.

1. Data analysis.

Both stochastic and SRE (single recoil energy) methods are used in analyzing the experimental data.[7] The stochastic procedure is embodied in Eqs (1) and (2) and is actually the correct data analysis procedure.

It starts from a LAB ← CM transformation, by assuming a form of $Q(\theta,u,V)$ and averaging over the measured velocity distributions of the parent beams to yield $I(\Theta)$ which is subsequently compared with measured value. This comparison is repeated until a satisfactory agreement is achieved by varying $Q(\theta,u,V)$.

Two assumptions are made in the stochastic procedure; they are (1) the factorability of CM angle and product recoil energy and (2) no activation barrier in the reaction channels (i.e., $Q(\theta,u,V) = Q(\theta,u)$). These assumptions have been commonly used in data analysis for alkali atom reactions.[8] The validity of this second assumption is challenged somewhat by the recent observation[9] of the $K + Br_2$, BrCN, and CCl_4 reactions. Employing a supersonic atom beam ($E = \sim 5$ kcal/mole), this experiment showed an increased forward scattering but decreased total reaction cross section with respect to results obtained using thermal beams for these reactions; however, the quantitative validity of some of these thermal beam studies is open to question because of uncertainties in the beam speed distributions so that it is unclear what to make of the results of Ref. 9. Furthermore, results of detailed product velocity analyses experiments on the $K + I_2$ reaction[10] with well defined collision energy, $E = 1.9 - 3.6$ kcal/mole, indicated that the CM scattering pattern is insensitive to the collision energy, although the total cross section decreases rather weakly with increasing energy. Moreover, this study also supports the assumption of separability of the recoil angle and energy distributions because only a weak coupling of these distributions was found for the $K + I_2$ reaction. This weak coupling of

the recoil angle and energy has also been indicated in a few reports of trajectory calculations.[11] As has been pointed out,[12] product internal energy (therefore recoil velocity) distributions seem to arise from the properties of the potential well at small interatomic distance whereas the scattering patterns depend on the details of the potential surface at large reactant separation, so that this weak coupling assumption generally gives a fairly satisfactory result in determining the CM differential cross section.[2b,11a] Accordingly, the CM differential cross section, $Q(\theta,u)$, in the stochastic procedure is simply expressed in terms of the product of two independent functions as $Q(\theta,u) = T(\theta)\ O(u)$ with $T(\theta)$ and $O(u)$ given in the conventional forms[7a]

$$T(\theta) = (1 - C_1)\ \exp\left[-\ln 2\left(\frac{\theta-\theta_1}{H_1}\right)^2\right] + C_1 \qquad (3)$$

and

$$O(u) = 1 \qquad u_1 \leq u \leq u_2 \qquad (4a)$$

$$= \left(\frac{u}{u_1}\right)^{n_1} \exp\left\{\frac{n_1}{m_1}\left[1 - \left(\frac{u}{u_1}\right)^{m_1}\right]\right\} \qquad u < u_1 \qquad (4b)$$

$$= \left(\frac{u}{u_2}\right)^{n_2} \exp\left\{\frac{n_2}{m_2}\left[1 - \left(\frac{u}{u_2}\right)^{m_2}\right]\right\} \qquad u > u_2 \qquad (4c)$$

where symbols with subscripts are constants. Since the low velocity portion of the $O(u)$ distribution is weighted more heavily in the Jacobian factor during the LAB $\leftrightarrow$ CM transformation, the measured LAB angular distribution determines the form of Eq. (4b) more uniquely than that of Eq. (4c). Therefore, for a given $T(\theta)$ distribution, the

LAB angular distribution is, in general, relatively insensitive to the full width of the O(u) distribution and results of our kinematic analysis should provide a fairly good estimate of the T(θ) distribution but only a crude estimate of the O(u) distribution. Because of this lack of sensitivity, the LAB ↔ CM transformation was also performed by employing a simpler procedure, the single recoil energy (SRE) method[7,8] which has been extensively used in analyzing most of alkali atom reactions.

In addition to the assumptions included in the stochastic method, the SRE approximation further assumes that the product recoil velocity may be treated as a delta function and the entire LAB angular distribution arises from a CM angular spread. Thus, the CM angular distribution derived by SRE is anticipated to be broader than that obtained from the stochastic method and is taken as the upper limit on the breadth of the true T(θ) distribution.

2. Reactive scattering.

Figures 1 - 8 show the measured product LAB angular distributions of alkaline earth monohalides and the resultant CM angular distributions and product energy density functions obtained by averaging over the measured beam speed distributions. For all of these reactions, Me + X_2, the only detectable product were MeX^+ ions. The identification of the MeX^+ with MeX rather than MeX_2 is based on the shape of the measured LAB angular distribution. Any MeX_2 formed would have to be directed along the center-of-mass vector ($\vec{C}$) in the LAB. Figures 1 - 2 also show the calculated angular distributions of $\bar{C}$ and clearly indicate

Fig. 1. Product angular distributions and CM recoil functions for the Ba + Cl_2 reaction. The solid data points (one run) show measured LAB angular distribution and the solid curves appeared in the three panels are the best fit found. The CM angular distribution is given as a range (— and ---), derived from the stochastic procedure, within which a satisfactory fit to the data is achieved; the energy density function, P(E'), has been converted from the CM recoil velocity distribution given in Table II (M mode). The upper bound on the CM angular distribution (— · —) is obtained from the SRE method. The calculated number density centroid distribution and kinematic diagram based on the most probable beam velocities for three possible product recoil energies, E', are also shown.

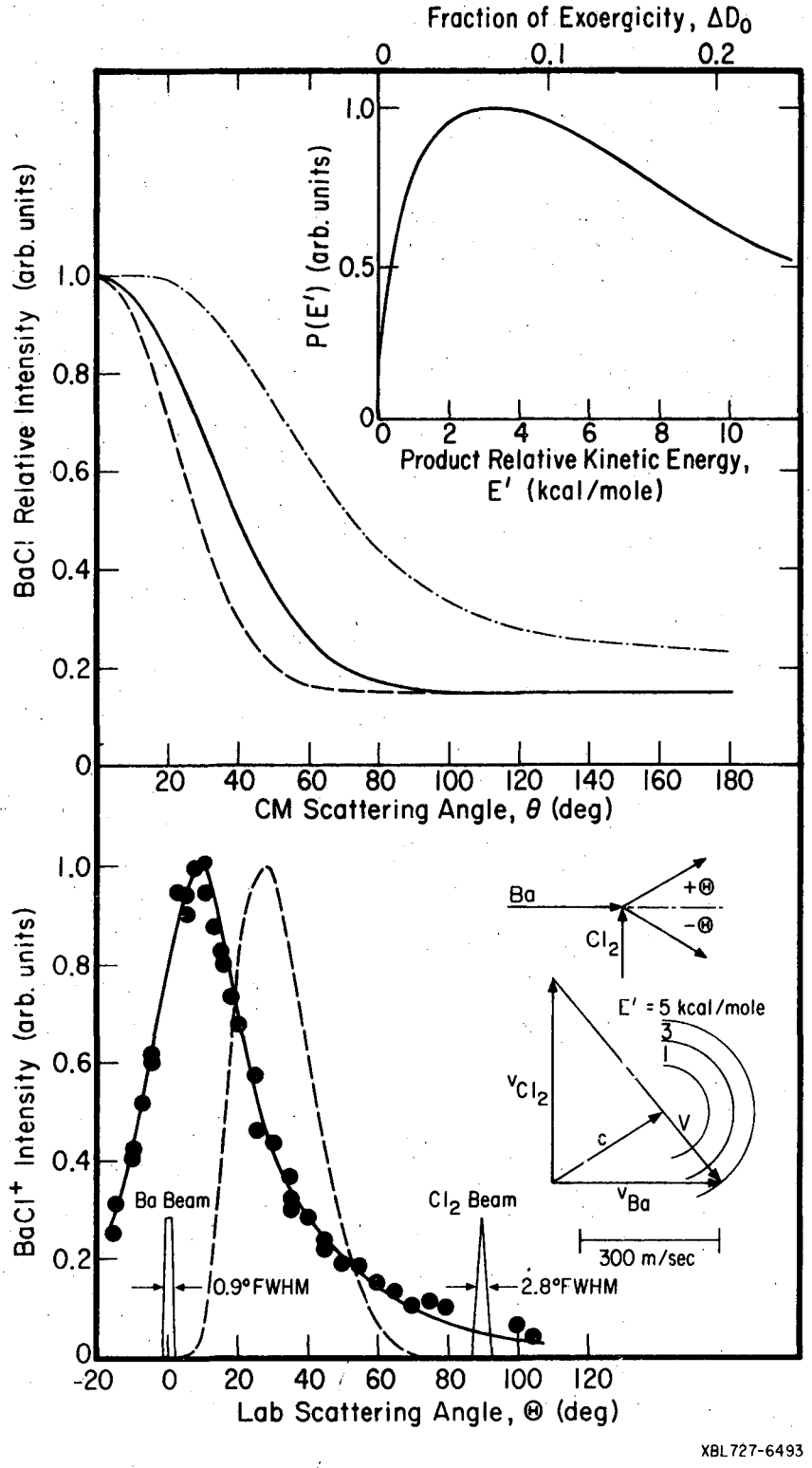
Fraction of Exoergicity, ΔD_0
0
0.1
0.2
1.0
0.5
0
P(E') (arb. units)
0 2 4 6 8 10
Product Relative Kinetic Energy, E' (kcal/mole)
BaCl Relative Intensity (arb. units)
1.0
0.8
0.6
0.4
0.2
0
20 40 60 80 100 120 140 160 180
CM Scattering Angle, θ (deg)
BaCl+ Intensity (arb. units)
Ba
+Θ
-Θ
Cl2
E' = 5 kcal/mole
3
2
1
vCl2
V
c
vBa
300 m/sec
Ba Beam
Cl2 Beam
0.9°FWHM
2.8°FWHM
-20 0 20 40 60 80 100 120
Lab Scattering Angle, Θ (deg)
XBL727-6493

Fig. 1.

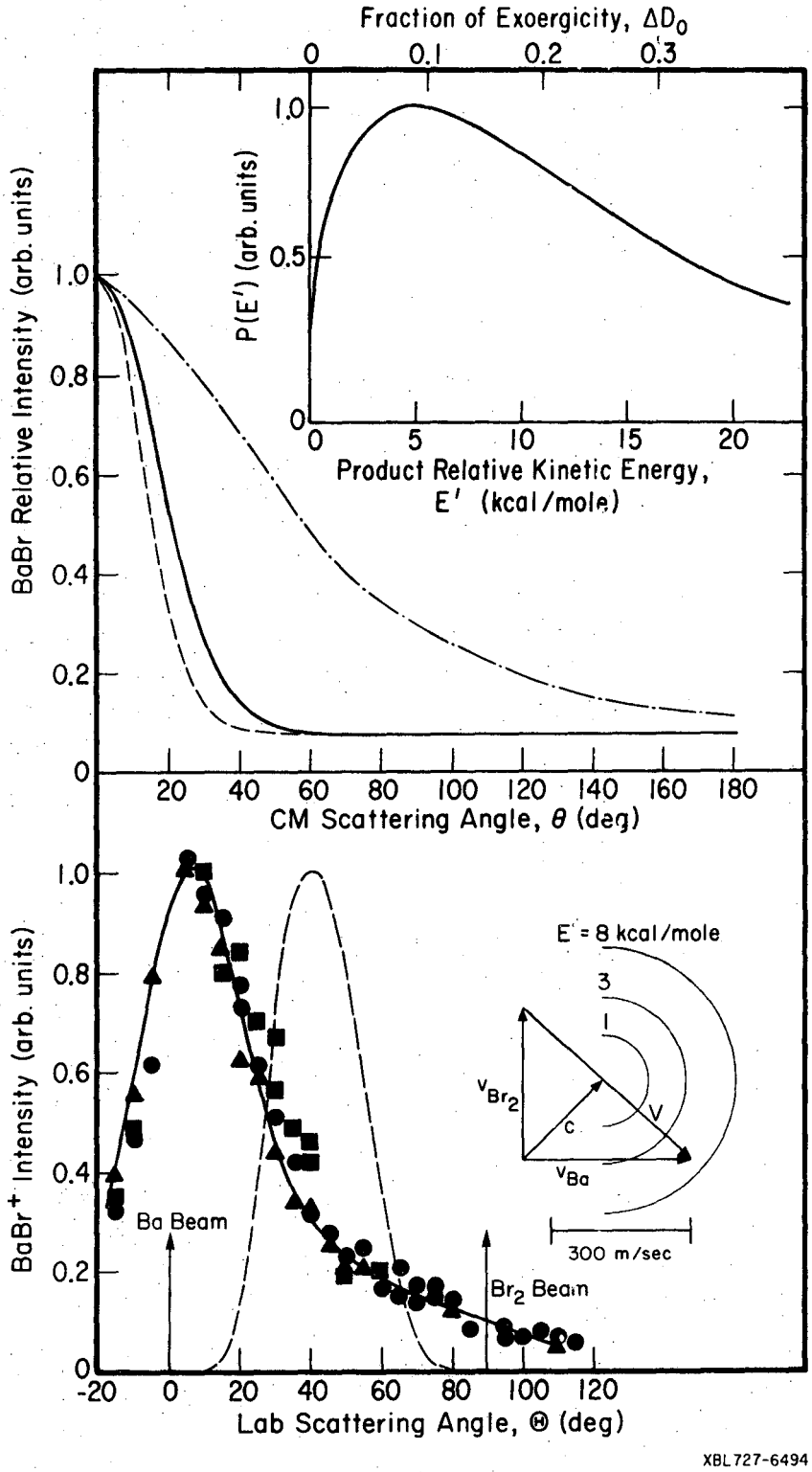

Fig. 2. Product angular distributions and CM recoil functions for the Ba + Br_2 reaction (3 runs). Format is as it was for Fig. 1 hereafter.

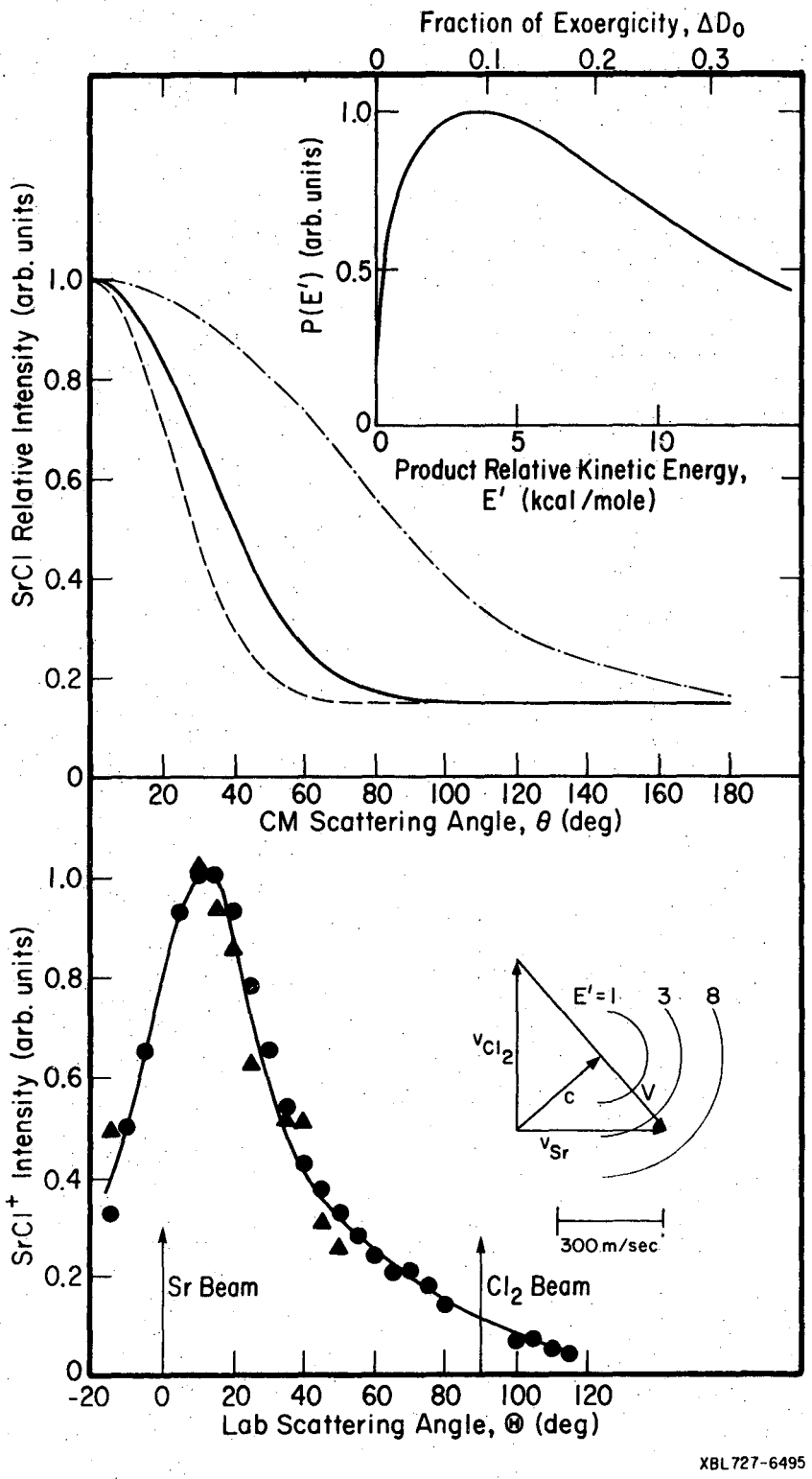

Fig. 3. Product angular distributions and CM recoil functions for the Sr + Cl_2 reactions (2 runs).

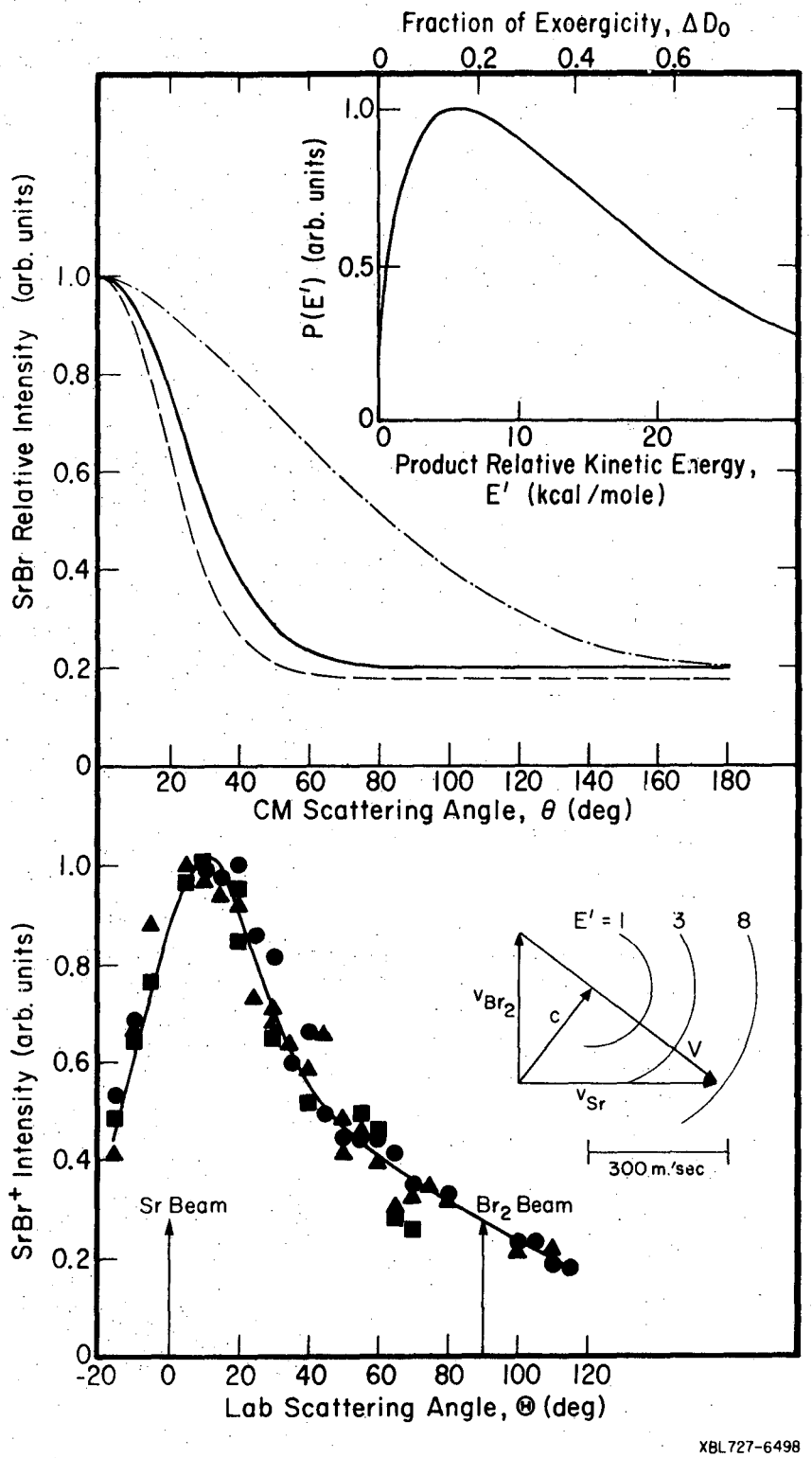

Fig. 4. Product angular distributions and CM recoil functions for the Sr + Br_2 reaction (3 runs).

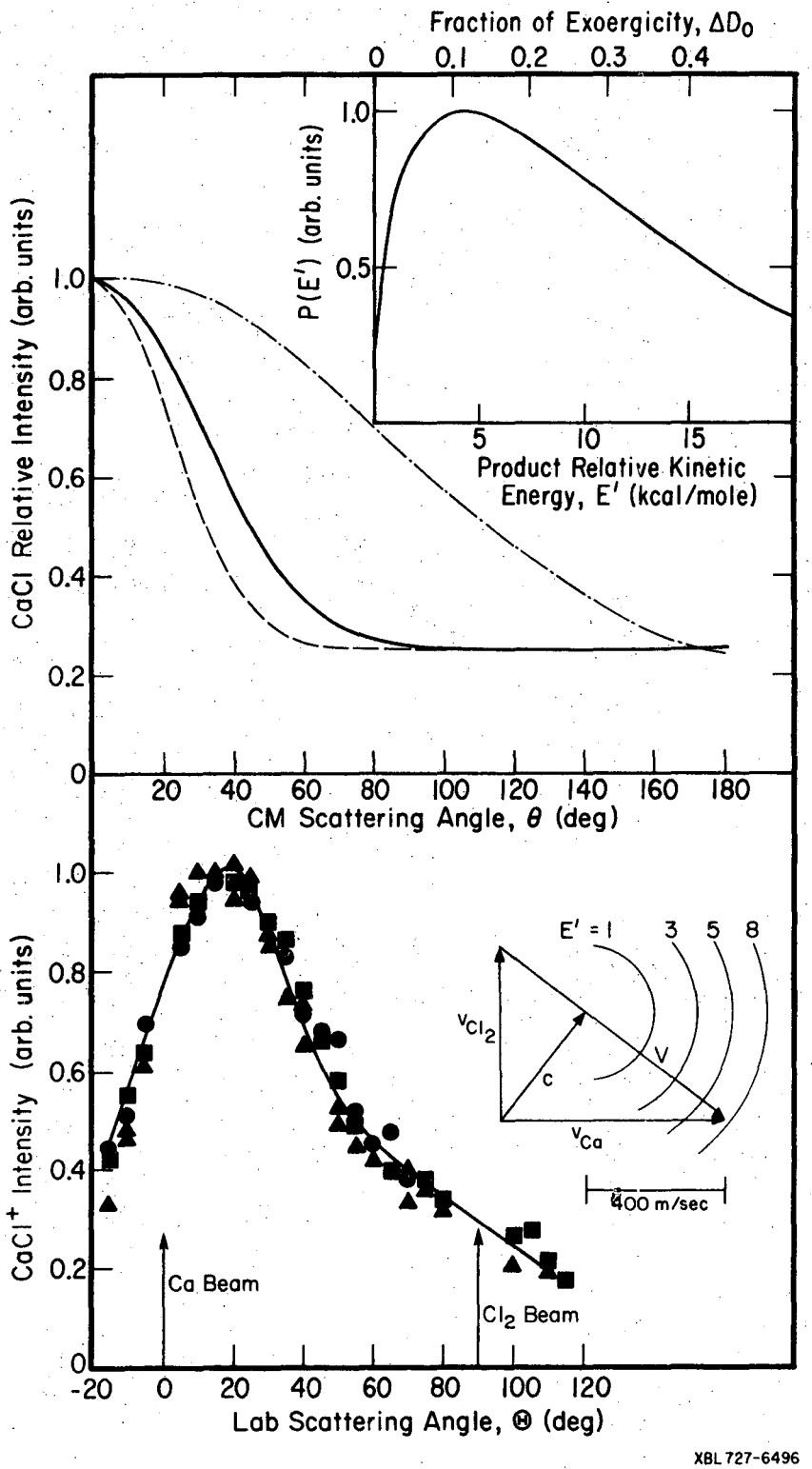

Fig. 5. Product angular distributions and CM recoil functions for the Ca + Cl_2 reaction (3 runs).

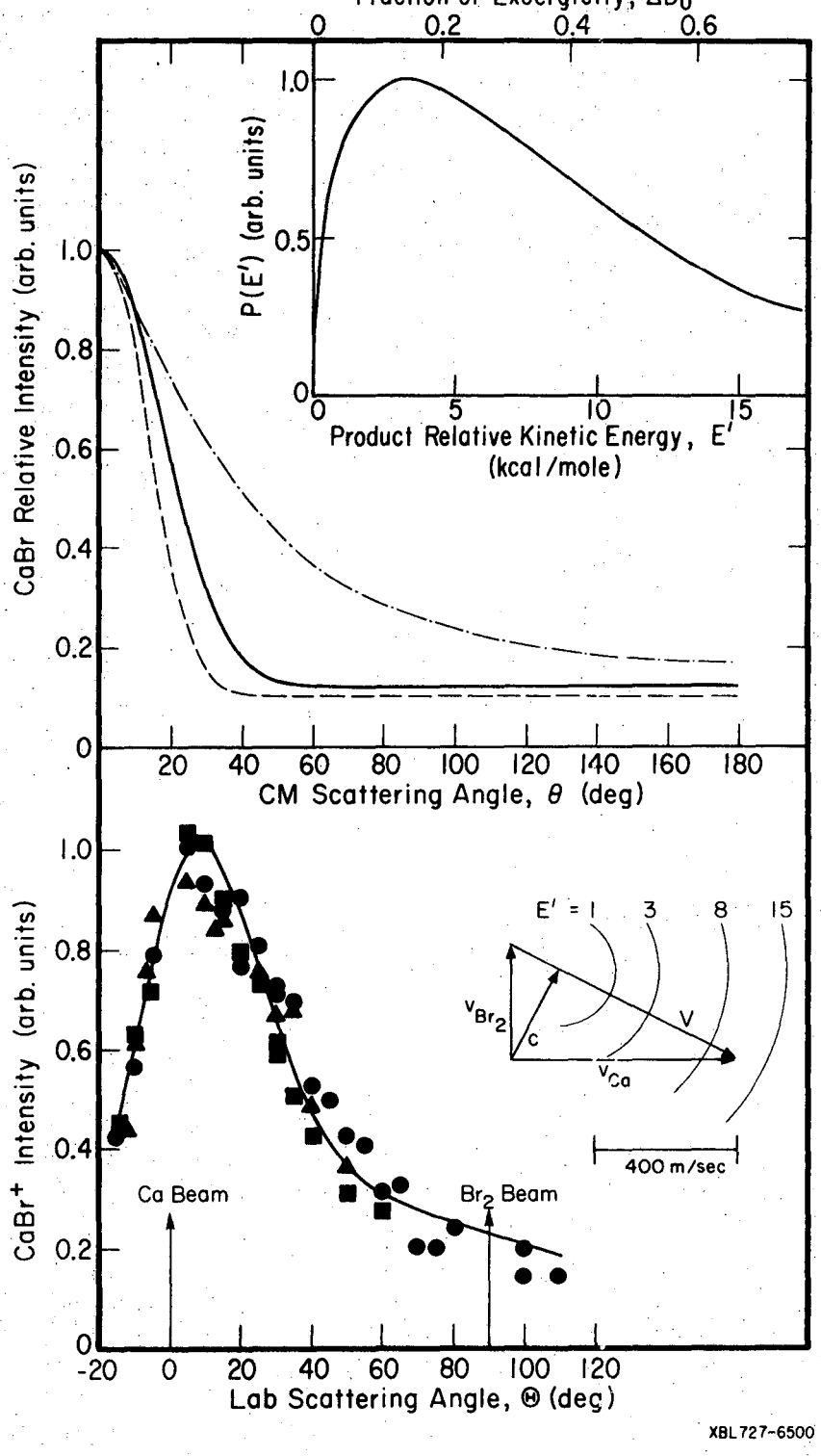

Fig. 6. Product angular distributions and CM recoil functions for the Ca + Br_2 reaction (3 runs).

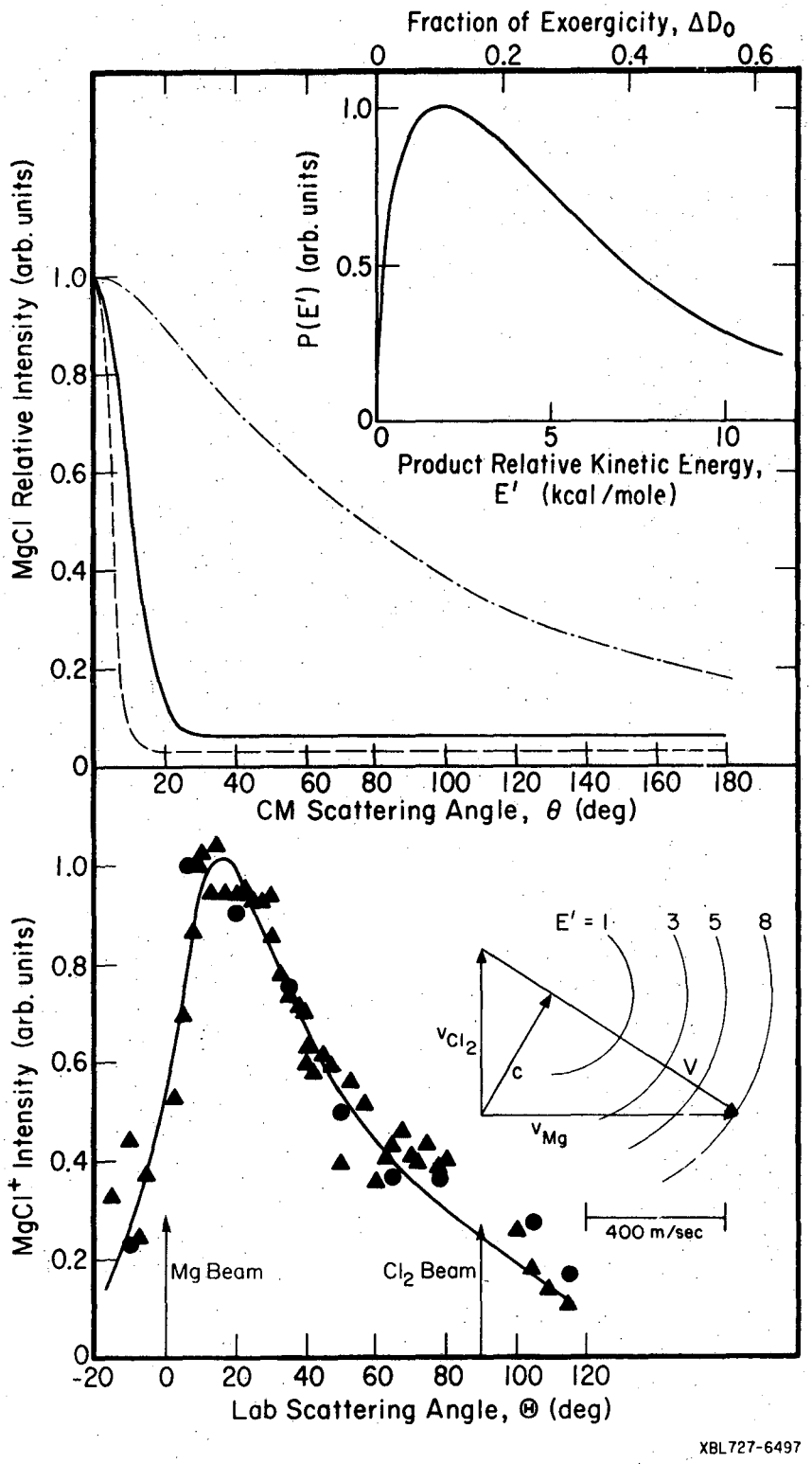

Fig. 7. Product angular distributions and CM recoil functions for the Mg + Cl_2 reaction (2 runs).

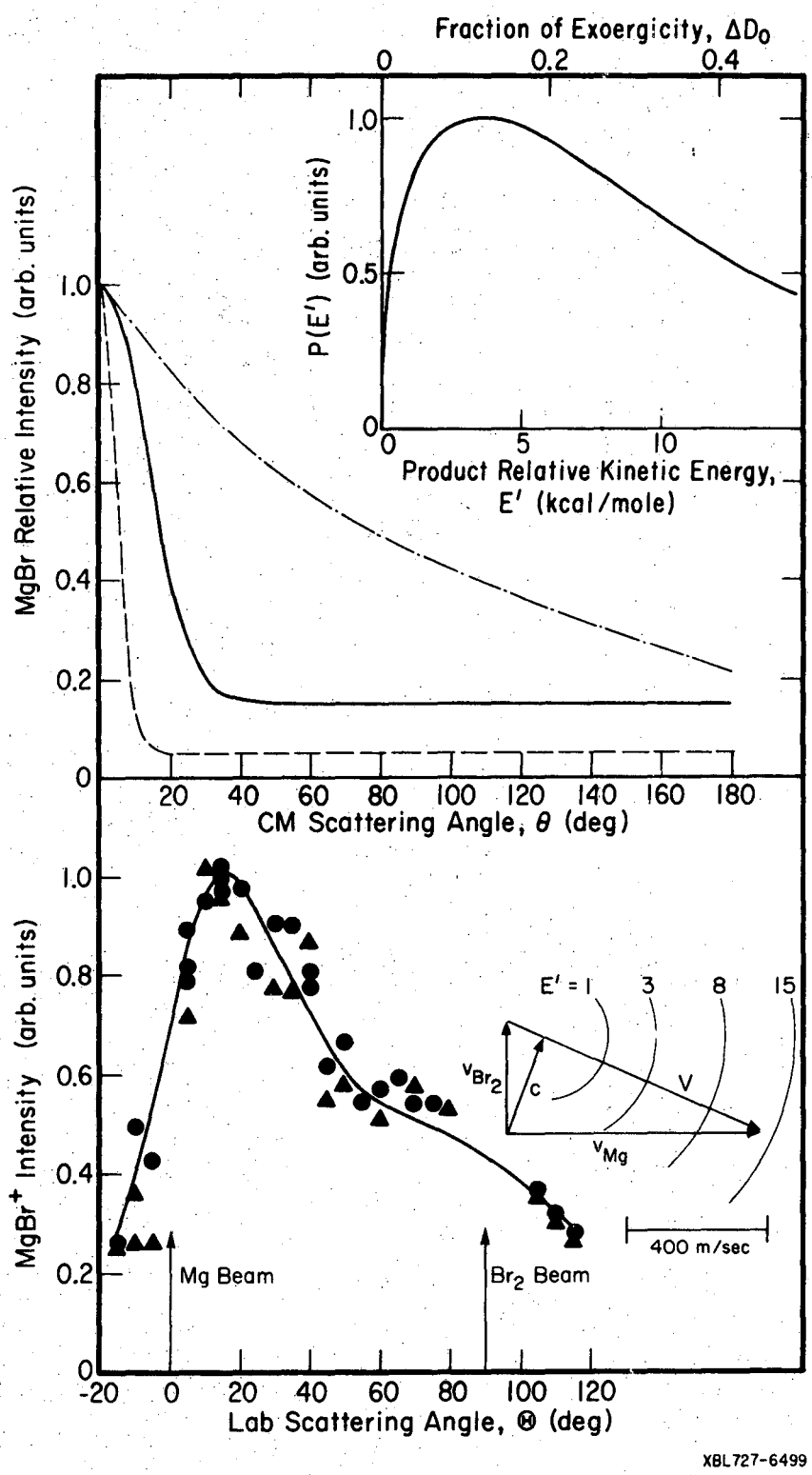

Fig. 8. Product angular distributions and CM recoil functions for the Mg + Br_2 reaction (2 runs).

this is not observed for any of these reactions. Moreover, our results on the Me + ICl reactions,[13] with two distinguishable LAB angular distributions corresponding to product MeI and MeCl, further illustrate that the dihalides are not significantly produced in this family of reactions.

Velocity measurements of parent beams have indicated that our beam velocities were different from the Boltzmann distributions, particularly the crossed beam. Although deviations in the Ba beam were minor, our data analysis used the measured speed distributions which were also fitted by the empirical equation (Eq. 1 described in previous chapter) with $v_s = 1.06 \times 10^4$ cm/sec and the most probable speed, α, corresponding to a calculated temperature, 810°K. We converted this correction to other lighter atoms whose velocity distributions were not measured experimentally by using the same expression and attenuation factor (33%). Detailed discussion of these conversions is given in Ref. 13 and results of these parameters, v_s and α, are listed in Table 1. In practice, results derived from the data analysis procedure are (1) seriously in error if one doesn't recognize the non-thermal behavior of the halogen beam speed distribution, but (2) practically insensitive to recognition of the weaker non-thermal behavior of the alkaline earth beam.

For each reaction, the CM angular distribution is given in a range (the solid and dashed curves) within which the agreement between the calculated LAB angular distribution and the measured values is well satisfied. These two curves are obtained from the stochastic method

and the solid curve is the best fit found. Table II lists the best fit parameters for the CM angular and velocity distributions. The dashed-dot curve is obtained from the SRE method although this provides a less satisfactory fit to the LAB data for some of these reactions. The kinematic diagram shown in the lower panel, constructed from the measured peak beam velocities, illustrates LAB ↔ CM transformation and the product recoil velocities for some of the possible final relative kinetic energy, E', obtained from the relation E' = $\frac{1}{2}$ (m_{MeXX} m_{MeX}/m_X) u^2, for the reaction Me + X_2 → MeX + X; m_{MeXX} is the total mass and m_{MeX} is the mass of theproduct detected. This relation, combined with the expression P(E')dE' = O(u) du, is used to convert the product recoil velocity to the energy density function which appears in the upper panels. The total energy available to the products has to be partitioned between E' and internal excitation W' by

$$E' + W' = E + W + \Delta D_o \quad . \tag{5}$$

where $E = \mu V^2/2$ is the initial relative translational energy, W is the initial internal excitation of the halogen molecules, and ΔD_o is the bond energy difference in alkaline earth monohalide and halogen molecules, measured from the zero-point vibration level. Also shown in Fig. 1 - 2 is the number density centroid distribution calculated from an energy independent collision cross section. Table III summarizes results of our kinematic analysis.

Figure 9 shows a direct comparison of the best fit CM angular distributions among these reactions. For the Cl_2 reactions, we are

Table II. Parameters for recoil angle and velocity distributions.

Mode[a]	System	T(θ)			O(u)[b]		
		θ_1	H_1	C_1	u_1/u_2	n_1/m_1	n_2/m_2
M	Br_2 + Ba	0	20	.08	3.2	2	2
	Sr	0	27	.20	4.3	2	2
	Ca	0	20	.12	6.0	2	2
	Mg	0	15	.15	5.0	2	2
	Cl_2 + Ba	0	35	.15	2.3	2	2
	Sr	0	35	.15	3.5	2	2
	Ca	0	35	.25	5.5	2	2
	Mg	0	10	.06	4.5	2	2
T	Br_2 + Ba	-10	30	.15	3.0	2/1	4/2
	Sr	0	30	.35	4.0	2/1	4/2
	Ca	-10	25	.15	6.0	2/1	2/2
	Mg	0	15	.20	4.0	2/1	4/2
	Cs[c]	0	35	.20	2.5	2/1	4/2
	Cl_2 + Ba	0	30	.25	2.0	2/1	4/2
	Sr	0	40	.30	3.0	2/1	4/2
	Ca	0	30	.45	4.5	2/1	4/2
	Mg	0	10	.13	3.5	2/2	4/2
	Cs[c]	0	25	.10	2.0	2/1	4/2

[a] M refers to measured beam velocity distributions and T to thermal beams

[b] Parameters with subscripts 1 and 2 are taken as equal when only one value is given.

[c] These parameters were found in this work; LAB data were taken from J. H. Birely, et al. J. Chem. Phys. 47, 993 (1967) for Br_2 and R. Grice and P. B. Empedocles, J. Chem. Phys. 48, 5352 (1968) for Cl_2.

Table III. Kinematic results[a]

System	Energetics[b] E	W	ΔD_o[c]	stochastic E'[d]	Q_f[e]	SRE E'[d]	Q_f[e]	r_x[f]	MeX_2[g]
Br_2 + Ba	2.50	1.06	55	4.8	0.67	5.5	0.73	5.4	b
Sr	2.39	1.06	35	5.6	0.62	5.0	0.68	4.6	1
Ca	2.71	1.09	45	6.3	0.62	6.5	0.67	4.0	1
Mg	2.26	1.06	30	3.5	0.56	4.8	0.63	2.8	1
Cl_2 + Ba	2.13	0.88	48	3.1	0.71	3.5	0.70	5.1	b
Sr	2.22	0.88	39	3.5	0.71	3.5	0.71	4.4	b
Ca	2.56	0.95	37	4.2	0.64	4.0	0.65	3.9	1
Mg	2.21	0.88	18	1.9	0.58	3.5	0.67	2.8	1

[a]All energies are given in kcal/mole.

[b]The initial kinetic energy, E, is calculated from the measured peaked velocities in the two beams and the internal energy, W, is the sum of the classical rotor and of the excess vibrational energy of the halogen; spectroscopic constants were taken from G. Herzberg. Molecular Spectra and Molecular Structure I. Spectra of Diatomic Molecules. (D. Van Nostrand, Inc. Princeton, N.J., 1950). These estimated internal energies may be higher than the actual values since the possible relaxation of internal degree of freedom during an isentropic expansion would compress the range of these internal energy states of molecules in the gas beam.

[c]Bond dissociation energies were taken from: for Br_2 and Cl_2, R. J. Leroy and R. B. Bernstein, Chem. Phys. Letters 5, 42 (1970); for MeCl, D. L. Hildenbrand, J. Chem. Phys. 52, 5751 (1970); for MeBr, A. G. Gayton, Dissociation Energies and Spectra of Diatomic Molecules (3rd. Ed.) (Chapman and Hall Ltd. London, 1968).

[d]These are the most probable E' values, obtained from the peaks in the P(E') distributions shown in the upper panels in Fig. 1-8.

[e]Fraction of products scattered into forward hemisphere, where

$$Q_f = \int_o^{\pi/2} T(\theta) \sin\theta d\theta / \int_o^{\pi} T(\theta) \sin\theta d\theta$$

[f]These are the crossing radius (Å) between the covalent and the ionic potential surfaces of Me + X_2, given by $r_x = e^2/(I(Me) - E(X_2))$; the electron affinity of X_2 ($E(X_2)$) is taken from W. A. Chupka and J. Berkowitz, J. Chem. Phys. 55, 2724 (1971) and ionization potential for the metal (I(M)) is given in K. S. Krasnov and N. V. Karaseva, Optics and Spectro. 19, 14 (1965). These crossing distances are probably a little too large since the adiabatic electron affinity for Br_2 and Cl_2 was used in calculating them.

[g]These are given in L. Whaston, R. A. Berg, and W. Klemperes, J. Chem. Phys. 39, 2023 (1963); b refers to bend molecules and l to linear molecules.

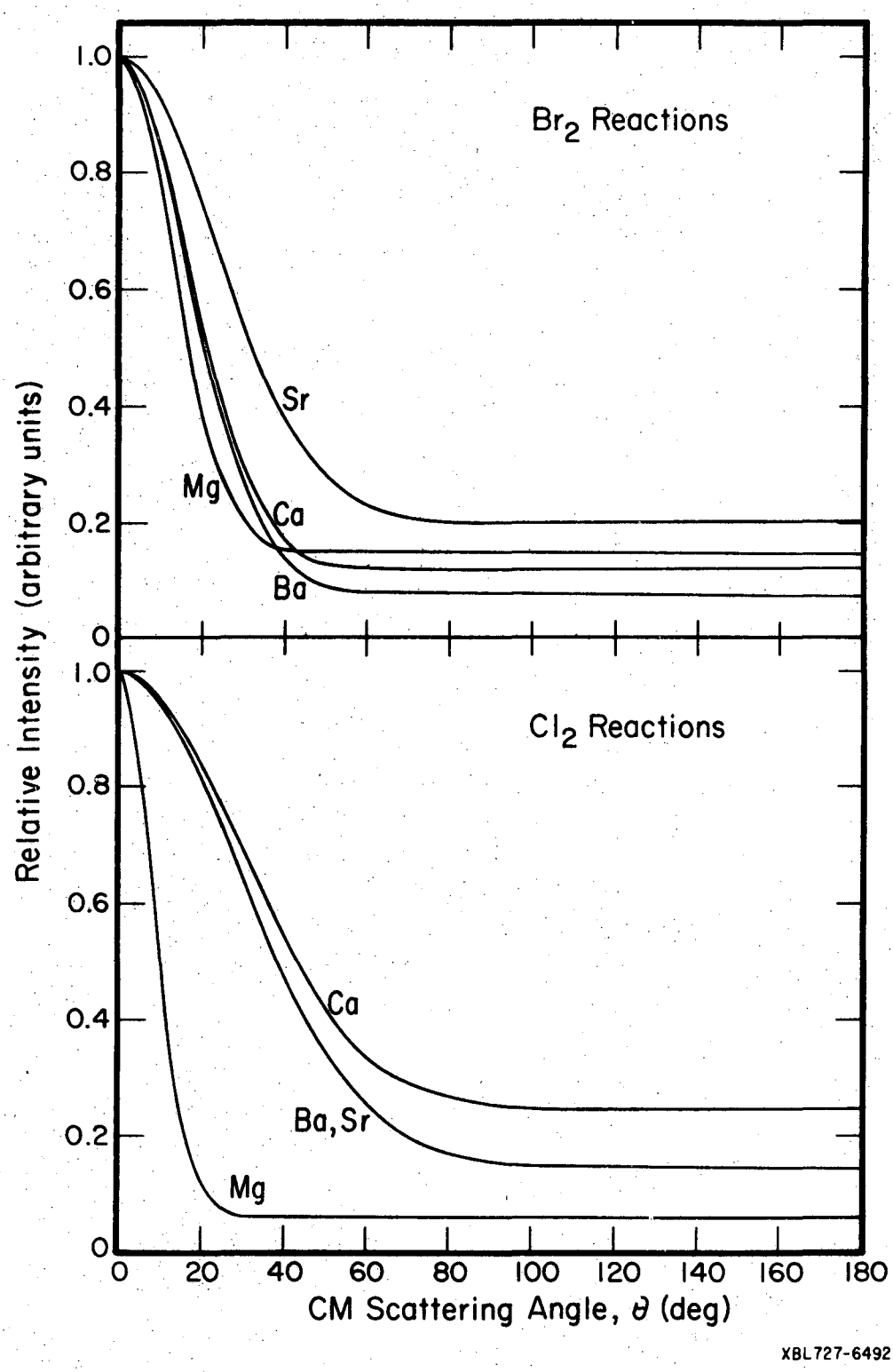

Fig. 9. Product CM angular distributions of Me + X_2 reactions; these distributions are corresponding to the solid curves shown in the middle panel of Fig. 1-8 and their parameters are listed in Table II (M mode).

able to use the same set of CM angular distribution to fit both the Ba and Sr reactions. when this set of parameters is taken to the Ca + Cl_2 reaction, we find that a smaller breadth of the LAB angular distribution occurs, mainly due to a small intensity at Θ larger than 30°. Consequently, our best-fit CM angular distribution for Ca + Cl_2 has a larger fraction at wide angle, θ, than does the Ba and Sr with Cl_2 reactions. For the Mg + Cl_2 reaction, this best fit CM angular distribution found for Ba and Sr + Cl_2 results a LAB angular distribution peaking at large Θ with too much intensity at small Θ in comparison with the measured values; this results remains almost the same for a wide range of O(u) distributions. Thus we have to decrease the H_1 and C_1 values in order to shift the peaking position to small Θ and the CM angular distribution appears to have a strong forward scattering pattern. Since its forward contribution is mainly confined at $\theta < 30°$, the fraction of MgCl scattered into the forward hemisphere is actually smaller than that for the heavier atoms. This is easily seen by integrating the differential cross section to its total reaction cross section in the form

$$Q_f = \int_o^{\pi/2} T(\theta)\, \sin\theta d\theta \;/\; \int_o^{\pi} T(\theta)\, \sin\theta d\theta.$$

Results of these calculations are also given in Table III. It clearly illustrates that this forward contribution decreases with decreasing mass of the reacting atom.

As we discussed earlier, the LAB angular distribution is generally more sensitive to the parameters of the CM angular distribution, $T(\theta)$,

but less sensitive to the full width of the velocity distribution, O(u), due to the Jacobian factor shown in Eq. (2). In order to show the sensitivity of the CM angular distribution to the measured LAB data, we have also tried to vary the backward contribution by increasing the CM angular distribution at large θ (i.e., θ = 91° - 180°); here, we modified Eq. (3) so that the $T(\theta)$ distribution remained the same at θ = 0° - 90° but was replaced by $(C_2 - C_1) \exp\{-\ln 2[(\theta - 180)/H_1]^2\} + C_1$ at θ = 91° - 180°. Thus, for a given set of C_2 and C_1 ($C_2 > C_1$), the $T(\theta)$ distribution first decreases until θ = 90° and then starts to slowly increase to C_2 at θ = 180°. For all of the Cl_2 reactions, the results of these calculations show that the difference between C_2 and C_1 can not be more than 0.1 without blowing up the intensity at large Θ. For the Ba + Cl_2 reaction, we have also tried to move the CM peaking angle to θ greater than 0° by either using a sideway peaking or a plateau extending from 0° to large θ; results show that a similar good fit is achieved by either extending θ_1 = 0°-10° or θ_1 = 15° combined with the best set of parameters, H_1 = 35° and C_1 = 0.15; for the latter case, a peak reflected through θ_1 = 15° is used for θ = 0°-30°.

For the Br_2 reactions, no given trend in its CM scattering pattern could be made among these reactions as shown in Fig. 9; Sr + Br_2 has a larger values of H_1 and C_1 than Ba and Ca + Br_2 reactions. A direct comparison in the product LAB angular distribution also shows that Sr + Br_2 has a breadth broader than that of Ba and Ca + Br_2. However, as with the chlorides, this system exhibits a decreasing order from

Ba to Mg in its forward contribution despite the variation in the CM angular distribution; here again, the difference between C_2 and C_1 is also less than 0.1. In all cases, the Br_2 reactions give a less forward contribution but larger ratio of $E'/\Delta D_o$ for a given atom in comparison with the Cl_2 reactions.

Finally, we like to comment on results derived from the SRE method as shown in Table III and Fig. 1 - 8 (—·— curves in the middle panels). Since this procedure removes the flexibility in the O(u) function, the T(θ) function has not been restricted to the form of Eq.(3). In favorable cases where the mass ratio of MeX/X is small, this procedure gives a good fits as well as the stochastic method. As a result, this procedure has a better fit for Mg + Cl_2 among the Cl_2 reactions and with a given Me, it is better for Br_2 than Cl_2; this particularly happens at small θ and large θ. For instance, it tends to give a small intensity at both tails of LAB angular distribution for Ba + Cl_2 which is the worst case.

3. Effect of non-thermal beam velocity distributions.

To understand the importance of non-thermal beam velocity distributions, we have also analyzed the data by assuming thermal beam distributions; results are listed in Table II (mode T) and their CM angular distributions are shown in Fig. 10. In all cases, these functions weight more at large θ for T(θ) distributions and small u for O(u) distributions when no velocity correction is made. This effect may be seen from the transformation diagram shown in Fig. 1 - 8 and the number density centroid distributions in Fig. 1 - 2. Since the

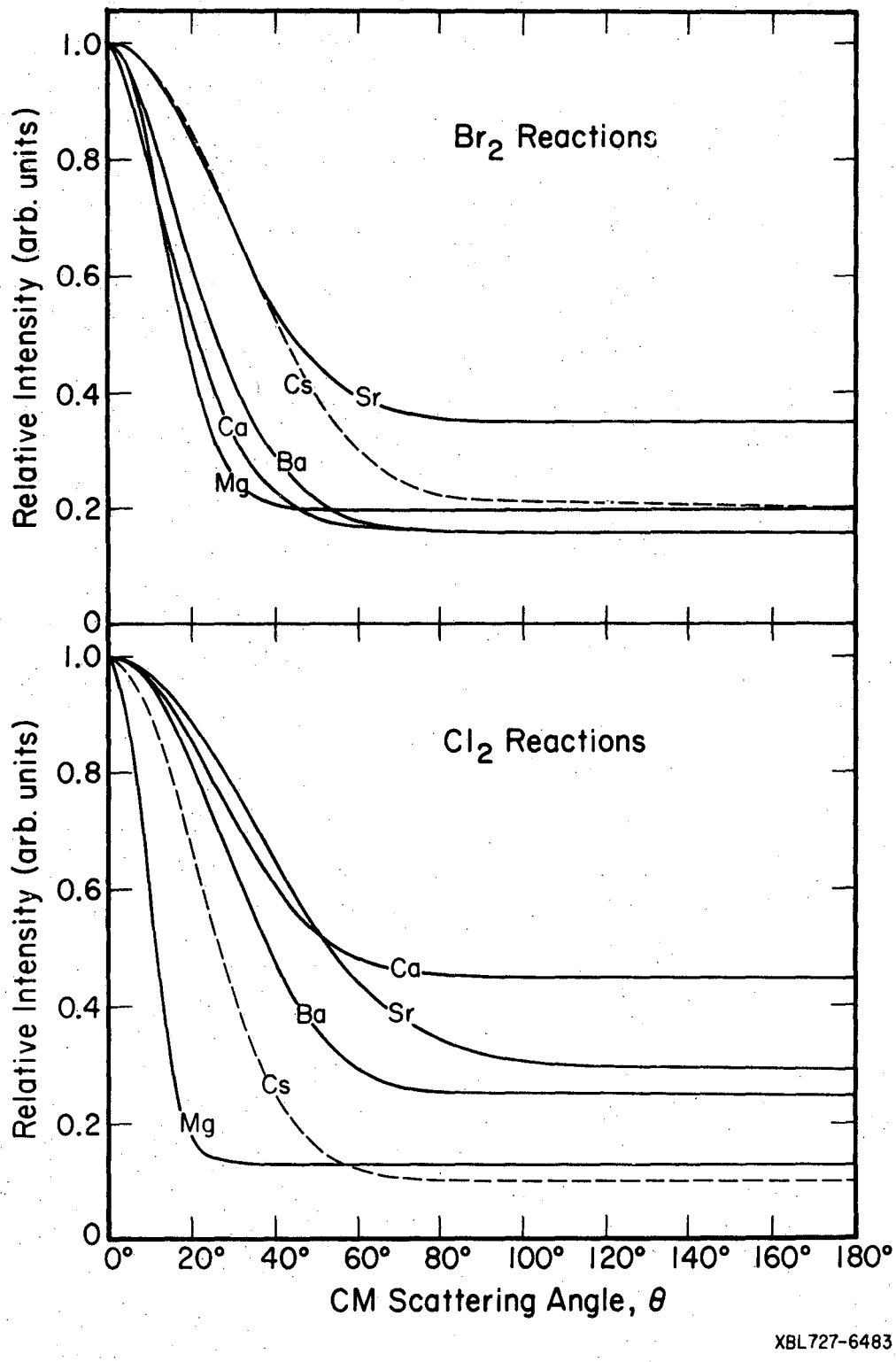

Fig. 10. Product CM angular distributions of Me + X_2 reactions, obtained using thermal beam velocity distributions. Also shown are the Cs + Br_2 and Cl_2 reactions; their parameters were found from this work and are given in Table II.

centroid distribution has become narrower and has shifted toward large Θ due to the upward shift of velocity enhancement for both parent beams, an increase in the product recoil velocity with a simultaneous decrease in $T(\theta)$ distribution at large θ is necessary to compensate this deficit for a LAB angular distribution peaking at small Θ when these velocity corrections are made.

At this point, we would like to comment on the early studies of alkali atoms with halogen reactions whose results were derived without this correction for non-thermal beam speed distributions. Although there was no indication of how large a gas pressure was used, their apparatus conditions were similar to ours so that similar non-thermal beam velocity distributions seem likely to have existed. Therefore, we believe, qualitatively, that a decrease in the wide angle contribution and an increase in the product recoil velocity would result if this beam velocity correction was taken into account. More detailed discussion of alkali system is deferred to the next section.

4. Total reaction cross section.

The Sr^+ angular distribution of scattering of Sr off of Br_2 was also measured; its behavior was similar to that of the non-reactive scattering of Li atoms[8] from Br_2 at narrow angles, but it fell off less rapidly at larger scattering angles. However, some of this Sr^+ signal might have arisen from ionization of SrBr rather than Sr; the possibility precludes any inferences regarding the elastic scattering in the collisions studied here. This inability to study the elastic scattering as well as unknown detector response factors also precludes

the determination of total reaction cross sections; order-of-magnitude estimates suggest $Q_r \sim 10 - 100$ Å^2 for Ba + Br_2 and Q_R for Mg reactions about 25% of those for Ba reactions. Jonah and Zare[4] reported $Q_r = 60$ Å^2 for Ba + Cl_2.

D. Discussion

Table III lists the fraction of the MeX product scattered into the forward hemisphere. Although present to some extent in the SRE results as well, the following trends in Q_f evaluated from the more reliable stochastic results are apparent: (1) for a given alkaline earth atom, the Cl_2 reaction produces somewhat more forward scattering than does the Br_2 reaction; (2) for a given X_2, the forward MeX scattered component increases in the sequence Mg, Ca, Sr, Ba; and (3) Sr + Br_2 more closely resembles Ca + Br_2 whereas Sr + Cl_2 more closely resembles Ba + Cl_2. The first two trends are also observed in the reactions of the alkali atoms with halogen molecules.[14] The third trend correlates with the geometries (linear vs. bent) of the ground electronic states of the alkaline earth dihalides,[15] although it is not clear how much significance should be assigned to this correlation because of the many other uncertain parameters associated with these reactions (e.g., precise forms of $T(\theta)$, reliable values for D_o(MeBr), and the absence of trajectory studies).

As Hildenbrand[5a] indicated, the Rittner ionic model yields reasonably accurate dissociation energies for BaCl and SrCl, fairly good for CaCl, but less accurate for MgCl; this trend is probably true

for monobromides as well. We thus argue on the basis of this ionic model that the electron transfer mechanism, which has been widely used to interpret the alkali and halogen reactions, may be also appropriate to describe the reactions reported here. In its simple form, the electron transfer model states that the neutral reactants approach each other on a covalent potential surface which is crossed by an ionic surface at large internuclear separation; in the vicinity of crossing point, an electron transfer from the alkaline earth atom to the halogen molecules takes place and the reaction becomes essentially an ion recombination. Since the van der Waals attraction is rather weak at separations larger than this crossing radius, it may be given in terms of the ionization potential of the atom, I(Me), and the electron affinity of the halogen molecules, $E(X_2)$, by

$$e^2/r_x = I(Me) - E(X_2) \qquad (6)$$

Here r_x refers to the crossing radius which is given in Table III. In its crudest form, this model predicts the total reaction cross section of πr_x^2.

In the interest of comparison between reactions of Group IA and of Group IIA atoms with halogen molecules, a brief discussion based on results of crossed beam studies will be presented here. As with our studies here, most of the alkali atom reactions[8] have been conducted by crossing two beams with full velocity distributions; results were then analyzed by either the SRE method or the stochastic procedure.

Although little information could be achieved by comparing our results, which have been derived for the actual beam velocity distributions, with those reported for the alkali atom reactions where a thermal beam distribution was always assumed, a qualitative idea may be obtained if we compare all results obtained by assuming thermal beams distributions. Thus, we have chosen two "prototype" reactions, $C_s + Br_2$ and Cl_2, to compare with Ba atom reactions which, as we discussed earlier, are considered to be closely related to the alkali atom reactions. Since the kinematic results reported for $C_s + Br_2$[16] and $C_s + Cl_2$[17] are not perfectly matched with the measured values, we have re-analyzed their data using the stochastic procedure. Figure 11 exemplifies results for $C_s + Br_2$ reaction. The solid curves are the best-fit found in this work with their parameters listed in Table II while the dashed and dashed-dot curves are taken from Ref. 7-a and 16, respectively. This best fit CM angular distribution is also shown in Fig. 10 (dashed curve); also included, is the "best-fit" data for $Cs + Cl_2$. A direct comparison shows that $Cs + Br_2$ has a broader scattering pattern than $Ba + Br_2$ whereas a reverse order occurs for Cs and $Ba + Cl_2$ reactions. This comparison, although not rigorous, further indicates that reactions for Ba atom and halogen molecules are indeed very similar to the Cs reaction rather than the Li reactions.[14] This observation is somewhat surprising because the electron transfer model would suggest that Li (I = 5.4 eV) and Ba (I = 5.2 ev) are likely to react within a similar range of impact parameters; it may indicate a high sensitivity of the product angular distributions in these electron

Fig. 11. Product angular distributions and CM recoil energy function for the Cs + Br_2 reaction. The solid data points and the dashed-dot-curve were taken from Ref. 16. The solid curves appeared in three panels were the "best-fit" found in this work while the dashed curves were given in Ref. 7-a. All of these calculations were made by assuming a thermal velocity distributions for both beams.

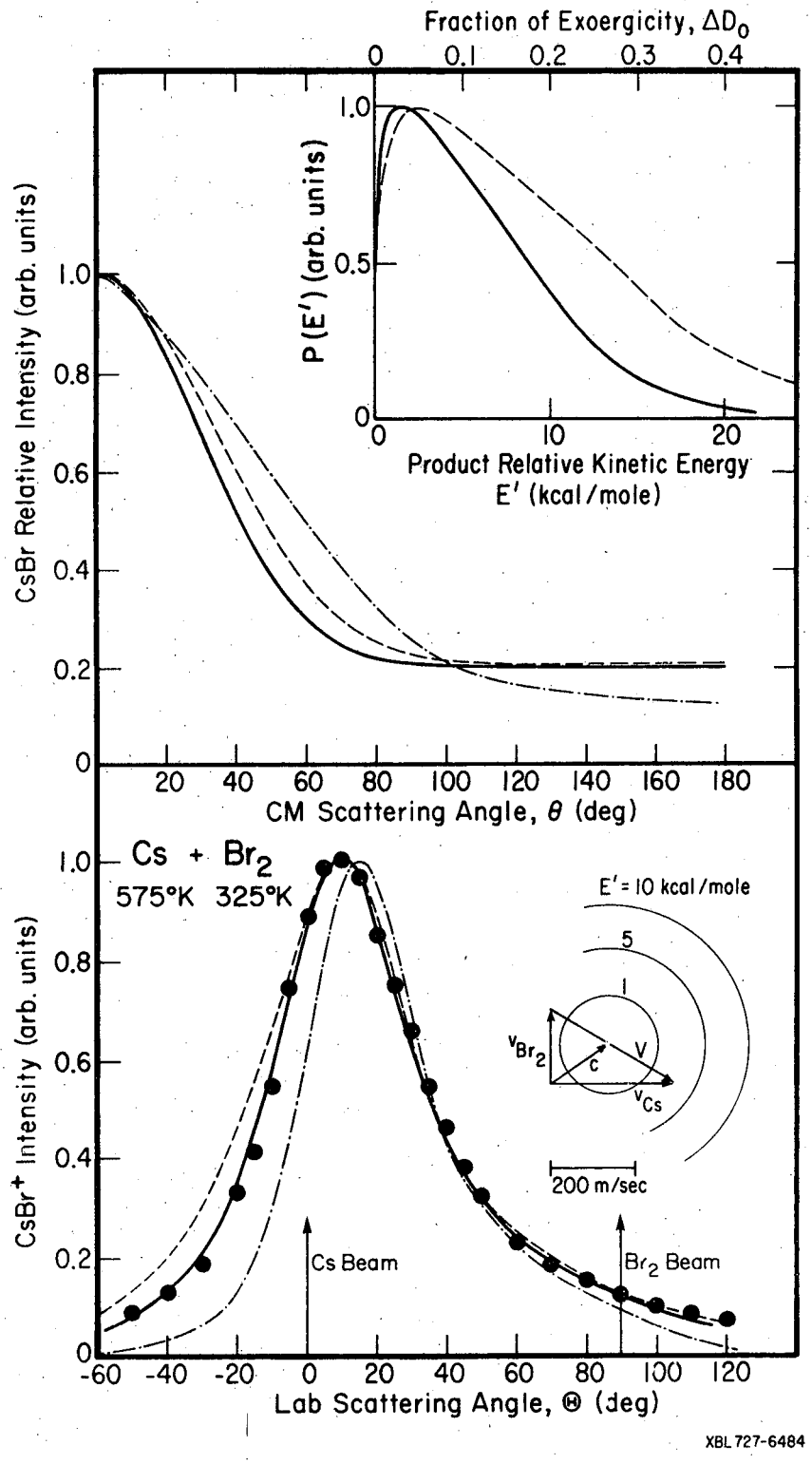

Fig. 11.

transfer reactions to the mass of the attaching atom. Existing trajectory calculations[18] do not support this conjecture, although these calculations have not extensively studied the influence of changing reactant masses.

In view of the deep chemical wells in the potential hypersurfaces for the alkaline earth reactions which are associated with the stability of the alkaline earth dihalides, this similarity between the reactions of alkali atoms and the heavier alkaline earth atoms (notably Ba) is striking. Studies of the reactions of alkali atoms with alkali halides[19] clearly indicate that the presence of a well corresponding to a stable intermediate can result in a long-lived collision complex reaction mechanism; on the other hand, the direct product scattering observed in the Li + NO_2 reaction[20] indicates that this need not always be true. Co-linear trajectories of attack of the Ba atom on the halogen molecule might be expected to lead to reaction without assuming intermediate configurations which felt the presence of this well; in terms of the electron transfer model, these reactive trajectories, at least, would be expected to resemble those characteristic of alkali reactions. Furthermore, the metal atom (alkali or alkaline earth) cannot transfer its totally symmetric valence electron into the vacant σ_u orbital (the lowest unfilled orbital) of X_2 in the case of the broadside approach along the C_{2v} symmetry axis because these two orbitals transform as different irreducible representations of the C_{2v} point group; this symmetry restriction is likely to favor the co-linear approach trajectory in reactive collisions.[21] Moreover,

even if the BaX_2 well were sampled in a significant fraction of the reactive trajectories, a crude RRK estimate indicates that, owing to the large reaction exoergicity, the lifetime of the complex would probably not exceed its rotational period.

The ionization potentials of Ba, Sr, Ca, and Mg are 5.2, 5.7, 6.1, and 7.6 ev, respectively. Thus, reactions of this family of atoms should show the transition from a reaction forming an ionic bond, where the potential surface exhibits long-ranged reactant attraction due to an electron transfer, to a reaction forming a covalent (more precisely, less ionic) bond, where the potential surface leading from reactants to products is more short-ranged and is, presumably, traversed more quickly. In view of this, it is perhaps surprising that the CM reactive cross sections given in Table III and Fig. 1-8 don't exhibit more variation for changing reactants. The stochastic MgCl angular distribution from Mg + Cl_2 which is shown in Figs. 7 and 9 is striking; this reaction especially warrants further study, with product velocity measurements, to quantitatively determine the CM cross section. While the wide-angle isotropic product scattering is likely to arise from small impact parameter collisions, the sharp forward spike in the product angular distribution for this reaction is suggestive of a spectator stripping mechanism. Although the true reaction trajectories are unlikely to be quite this simple, the spectator stripping model might approximate them because of rapidly reacting force in the reaction. Similar ideas have been advanced[16] in discussion of the forward product scattering seen in the Cl + Br_2 reaction.

In constrast to our kinematic result, however, the CM angular distribution of Ba + Cl_2 reaction reported by Bernstein and his coworkers[3a] is relatively broad despite a product LAB angular distribution of BaCl (8/13/71 data) very similar to ours. Owing to the randomly scattered data, Bernstein and his coworkers actually provided four different combinations of CM angular distribution and product recoil energy function; for all cases, they used a broader CM angular distribution and a narrower P(E') distribution to fit their experimental data. Among them, our best-fit product recoil energy function is essentially identical to their reported curve A and our upper limit of CM angular distribution found from SRE procedure is somewhat similar to their curve A at $\theta = 0° - 100°$. We have used their proposed four different sets of $T(\theta)$ and P(E') to analyze our data either on the basis of our measured beam velocities or by assuming thermal beam distributions; the latter was apparently used in their data analysis. All of their CM fits give too little intensity at Θ greater than 40° or 60°, and the predicted peaking angle is almost acceptable if one assumes thermal beams while a 5° - 15° shift toward large Θ occurs when the measured beam velocities are used. Because of the lack of sensitivity inherent in the kinematic analysis when the product detected is much heavier than its counter partner, their widely dispersed LAB angular distribution confined at Θ less than 60° would prevent them in choosing a more representative $T(\theta)$ and P(E') distributions. Nevertheless, their results (e.g., curve D corresponding to $Q_f = 0.72$) do agree that the reactively scattered product, BaCl, is predominantly confined in the forward hemisphere with a small

fraction of exoergicity appearing as the product recoil energy.

Results of this work may be summarized as: (1) most of the reaction exoergicity ($\gtrsim$ 80%) appears as internal excitation of the products rather than as product recoil energy; (2) the CM angular distribution of products is anisotropic: with respect to the incoming Me atoms, the Cl_2 reaction produces more forward scattering than does the Br_2 reaction for a given alkaline earth atom and for a given X_2, the forward MeX scattered component increases in thesequence Mg, Ca, Sr, Ba; (3) the Ba atom reactive cross sections, Q_R, are qualitatively much more similar to those of the Cs reactions rather than the Li reactions; order-of-magnitude estimates suggest $Q_R \sim$ 10-100 Å for Ba reactions and Q_R for Mg reactions about 25% of those for Ba reactions; and (4) experimental evidence gives no indications of a dihalide product (MeX_2) and the formation of MeX_2 can not account for more than a small fraction ($\lesssim$ 5%) of the reactive collisions.

REFERENCES

1. (a) Y. T. Lee, J. P. McDonald, P. R. LeBreton, and D. R. Herschbach, J. Chem. Phys. 49, 2447 (1968); 51, 455 (1969).

   (b) D. Beck, F. Engelke, and J. H. Loesch, Ber. Bunsenger Physik Chem. 72, 1105 (1968); 75, 736 (1971).

   (c) N. C. Blais and J. B. Cross, J. Chem. Phys. 52, 3580 (1970).

   (d) J. B. Cross and N. C. Blais, J. Chem. Phys. 55, 3970 (1971).

2. (a) T. P. Schafer, P. E. Siska, J. M. Parson, F. P. Tully, Y. C. Wong, and Y. T. Lee, J. Chem. Phys. 53, 3385 (1970).

   (b) J. D. McDonald, P. R. LeBreton, Y. T. Lee, and D. R. Herschbach, J. Chem. Phys. 56, 769 (1972).

   (c) J. Geddes, H. F. Krause, and W. L. Fite, J. Chem. Phys. 52, 3296 (1970).

   (d) J. Grosser and H. Haberland, Chem. Phys. Letters 7, 442 (1970).

3. (a) J. A. Haberman, K. G. Anlauf, R. B. Bernstein, and F. J. Van Itallie, WIS-TCI-482X, Wisconsin, July, 1972.

   (b) C. A. Mims, S. M. Lin, and R. R. Herm, to be published (J. Chem. Phys., 1972).

4. C. D. Jonah and R. N. Zare, Chem. Phys. Letters 9, 65 (1971).

5. (a) D. L. Hildenbrand, J. Chem. Phys. 48, 3657 (1968); 52, 5751 (1970).

   (b) K. F. Zmbov, Chem. Phys. Letters, 4, 191 (1969).

6. (a) K. Schofield and T. M. Sugden, Trans Far. Soc. 67, 1054 (1971)

   (b) L. V. Gurvich and V. G. Ryabova, High Temp. USSR, 2, 190 (1964); 3, 604 (1964).

7. (a) E. A. Entemann, Ph.D. thesis, Harvard University, 1967.
(b) E. A. Entemann and D. R. Herschbach, Disc. Far. Soc. 44, 289 (1967).

8. D. D. Parrish and R. R. Herm, J. Chem. Phys. 51, 5467 (1969); and references cited therein.

9. J. C. Whitehead, D. R. Hardin, and R. Grice, Mol. Phys. 23, 787 (1972).

10. K. T. Gillen, A. M. Rulis, and R. B. Bernstein, J. Chem. Phys. 54, 2831 (1971).

11. (a) T. B. Borne and D. L. Bunker, J. Chem. Phys. 55, 4861 (1971).
(b) P. J. Kuntz, M. H. Mok, E. M. Nemeth, and J. C. Polanyi, Disc. Far. Soc. 44, 229 (1967).

12. N. C. Blais and D. L. Bunker, J. Chem. Phys. 39, 315 (1963).

13. C. A. Mims, Ph. D. thesis, University of California, Berkeley, 1972.

14. For a review, see J. L. Kinsey, Chapt. 6, "Molecular Beam Reactions," in Biennial Rev. of Sci. Tech. and Med. vol. 9, Reaction Kinetic, MTP, Oxford (1972).

15. L. Wharton, R. A. Berg, and W. Klemperer, J. Chem. Phys. 39, 2023 (1963).

16. J. H. Birely, R. R. Herm, K. R. Wilson, and D. R. Herschbach, J. Chem. Phys. 47, 993 (1967).

17. R. Grice and P. B. Empedocles, J. Chem. Phys. 48, 5352 (1968).

18. (a) N. C. Blais, J. Chem. Phys. 49, 9 (1968).
(b) P. J. Kuntz, M. H. Mok, and J. C. Polanyi, J. Chem. Phys. 50, 4623 (1969).

19. (a) W. B. Miller, S. A. Safron, and D. R. Herschbach, Disc. Far. Soc. 44, 108 (1967).

(b) G. H. Kwei, A. B. Lees, and J. A. Silver, J. Chem. Phys. 55, 456 (1971).

20. D. D. Parrish and R. R. Herm, J. Chem. Phys. 54, 2518 (1971).

21. P. B. Foreman, G. M. Kendall, and R. Grice, Mol. Phys. 23, 127 (1972).

IV. REACTIONS OF ALKALINE EARTH ATOMS WITH SIMPLE ORGANIC COMPOUNDS

A. Introduction

This chapter presents our results on alkali earth atom reactions with CH_3I, CH_2I_2, $C\,Cl_4$, CF_3I, $C\,Cl_3NO_2$, and $(CH_3)_2\,CHNO_2$. Measurements of all product LAB angular distributions reported here have been obtained with the mass spectrometer tuned to the MeX^+ (X = I and Cl) signal for the first five reactants and MeO^+ for $(CH_3)_2\,CHNO_2$. These six reactants have been found to show a marked variation in chemical behavior; in the CM coordinate system, they vary from forward scattering for CH_2I_2, $C\,Cl_3NO_2$, and $(CH_3)_2\,CHNO_2$ to backward scattering for CH_3I, with intermediate behaviors for $C\,Cl_4$ and CF_3I.

In previous molecular beam studies of alkali atom reactions, these three prototype direct reaction mechanisms[1] have also been found; in general, the transition from forward scattering, to sideway peaking, to backward scattering occurs as the magnitude of the reaction cross section decreases. Of the six organic reactants studied here, reactions of CH_3I with alkali atoms have been most extensively investigated in both crossed molecular beam studies[2] and model calculations;[3] these reactions yielded products scattered mainly into the backward hemisphere and proved to be the typical example of rebound scattering. In constrast to CH_3I, the recent study of CH_2I_2 with Cs and K reactions[4] showed broad forward product scattering with large reaction cross sections ($\tilde{>}$ 150 A^2). Measurements of crossed beam product angular distributions from $C\,Cl_4$ + alkali atoms,[5,6] on the other hand, indicated that these reactions are intermediate between

the backward and forward scattering behaviors; moreover, a strong coupling between the CM recoil angle and velocity distributions has also been reported for this system.[7] Although no previous measurements of product angular distributions for the other three reactants, CF_3I, $C Cl_3NO_2$, and $(CH_3)_2 CHNO_2$, have been reported, a number of crossed beam studies of alkali + CH_3NO_2 reactions have been published by Herm and his associates.[8] In these studies, they have assigned the alkali nitrite as the scattered product from a detailed analysis of magnetic and electric deflection experiments. The steric effect for CF_3I reacting with K atoms has been demonstrated recently in the crossed beam studies;[9] this result and the early flame experiments[10] indicate that KI is the principal reaction product.

B. Experimental Conditions

Experimental conditions are essentially the same as in the study of the Br_2 and Cl_2 reactions. Velocity measurements have been made for the CH_3I, CH_2I_2, $C Cl_4$, and $(CH_3)_2 CHNO_2$ beams; they also show a upward shift in the velocity distributions with respect to thermal beams and are fitted by the same equation described in chapter II but with various flow speed, v_s. Since the dependence of v_s on source pressure is similar for a number of gases studied, we have interpolated v_s values for CF_3I and $C Cl_3NO_2$ from the calculated v_s values of other gases. Although the beam velocity spectra for $(CH_3)_2 CHNO_2$ have been measured at several pressures, the high velocity portions were not measured because of the speed limitations of our small velocity selector. We are thus unable to determine v_s at its high pressure

limit so that an interpolated value is used here as well. Details of these pressure dependences of the flow speeds are discussed in Ref. 11.

In this work, not all of the alkaline earth atoms have been observed to react with these six reactants. Although it varies somewhat from system to system, we estimate that the sensitivity of our apparatus is such that we would observe reaction product if the reaction cross section were as large as ~ 1-5 $Å^2$. For Mg atoms, no product has been found when crossing with CH_3I molecules; since the reaction cross sections for Mg are apparently smaller than those for heavier atoms and since there existed a high background noise at low massnumber in our massfilter, no further attempts were made to study reactions of Mg with other reactants. Table I summarizes the reactions studied and Table II lists the experimental conditions for those reactions where product angular distributions have been measured.

C. Data Analysis

The same procedures, the stochastic and the single recoil energy (SRE), used in analyzing the Br_2 and Cl_2 data are employed here. In the stochastic procedure, the CM angular distribution is expressed as

$$T(\theta) = (1-C_1)\exp\left[-\ln 2\left(\frac{\theta-\theta_1}{H_1}\right)^2\right] + C_1 \qquad \theta > \theta_1 \qquad (1a)$$

$$= 1 \qquad \theta_1 \geq \theta \geq \theta_2 \qquad (1b)$$

$$= (1-C_2)\exp\left[-\ln 2\left(\frac{\theta-\theta_2}{H_2}\right)^2\right] + C_2 \qquad \theta < \theta_2 \qquad (1c)$$

Table I. Summary of reactions studied[a]

	Alkaline earth atom (Me)				
Molecules	Ba	Sr	Ca	Mg	Mass peak detected
CH_3I	R	R	R	NR	MeI^+
CF_3I	R	NS	NS	NS	BaI^+, BaF^+
CH_2I_2	R	R	R	NS	MeI^+
CH_2Br_2	NS	NS	F	NS	$CaBr^+$
CH_2BrCl	F	NS	NS	NS	$BaBr^+$
CCl_4	R	I	NR	NS	$BaCl^+$
CCl_3Br	NS	NS	NR	NS	
CCl_3NO_2	NS	NS	R	NS	$CaCl^+$, CaO^+
$(CH_3)_2CHNO_2$	R	R	NR	NS	MeO^+
$(CH_3)_2CH(CH_2)_2ONO$	NS	F	NR	NS	SrO^+, $SrNO^+$, $C_5H_{11}OSr^+$
$(CH_3)_3COH$	NR	NS	NS	NS	

a. R = product angular distributions reported here

NR = no reaction

NS = not studied

F = product observed, but meaningful angular distribution not obtained

I = interference from a mass peak of reactant beam.

Table II. Experimental conditions.[a]

System	Alkaline earth atom source				gas source		
	Source Conditions		Speed	Distribution	Source	Conditions	flow speed
	T	P	α	v_s	T	P	v_s
CH_3I + Ba	1030	0.26	3.1	1.1	360	3.3 - 3.9	1.7
Sr	980	0.6	3.7	1.3	330	3.0 - 3.5	1.7
Ca	1050	0.6	5.8	1.9	370	3.4	1.7
CH_2I_2 + Ba	1050	0.32	3.1	1.1	330	0.6	0.67
Sr	970	0.5	3.7	1.3	340	0.3 - 0.6	0.6
Ca	1030	0.4	5.8	1.9	330	0.4	0.4
$C_3H_7NO_2$ + Ba	1020	0.2	3.1	1.1	390	2.6	1.8
Sr	960	0.4	3.7	1.3	350	2.8	1.8
CCl_3NO_2 + Ca	1020	0.4	5.8	1.9	320	3.8	1.7
CCl_4 + Ba	1040	0.28	3.1	1.1	370	3	1.6
CF_3I + Ba	1060	0.35	3.1	1.1	330	3.5 - 4.1	1.4

[a]Temperature is given in °K, pressure in Torr, and speed in 100 m/sec.

For each reaction, this expression enables us to determine a forward scattered component (Eq. 1-a, b), a backward scattered component (Eq. 1-b, c), or a sideway peaking (Eq. 1-a, b, c). The O(u) distribution used here is of the same form as that described in the previous chapter. Table III lists our best-fit parameter, obtained from the stochastic analysis, for the T(θ) and O(u) distributions.

D. Results and Discussion

Owing to the various chemical behaviors among these six reactants, detailed kinematic results for reactively scattered products are discussed separately.

1. CH_3I with Ca, Sr, and Ba.

Figures 1-3 show kinematic results for CH_3I reactions with the same conventional format designated for the halogen reactions reported in the previous chapter. A backward scattering in the CM angular distribution with a substantial amount of reaction exoergicity appearing as the product recoil energy is found for all three reactions; both the T(θ) and P(E') distributions show an increase in their breadth and peaking recoil energy from Ca to Ba with Sr as the intermediate case. Table IV lists results of data analysis of the CH_3I reactions.

For Ca + CH_3I, there is a tendency to give too little intensity at small θ ($\lesssim 20°$) for both the stochastic and SRE methods. We have also tried to modify Eq. 1-c, as described in the previous chapter, to give a fraction of 50% at $\theta = 0°$ from the best set parameters found for Ca + CH_3I in the stochastic procedure; however, results of this calculation show no increasing intensity at $\theta < 15°$, but give too large

Table III. Parameters for CM recoil angle and velocity distributions.[a]

System	T(θ)				O(u)	
	θ_1/θ_2	H_1/H_2	C_1/C_2	u_1/u_2	n_1/n_2	m_1/m_2
CH_3I + Ba	180/140	80	0.3	1.4	6	2
Sr	180	60	0.1	1.6	6	2
Ca	180	40	0.1	1.9	6	2
CH_2I_2[b] + Ba	0	100	0.3	1.2	2	2
Sr	0	100	0.3	1.2	2	2
Ca	0	100	0.5	1.0	2	2
$C_3H_7NO_2$ + Ba	0	30	0.15	3.5	2	2
Sr	5/0	10	0.15	4.3	2	1/2
CCl_3NO_2 + Ca	5/0	15	0.2	7	2	1/2
CCl_4 + Ba	30	60/30	0.2/0.5	4.0	2	2
CF_3I + Ba	90/70	45/15	0/0.8	2.5	6	6

[a]Parameters with subscripts 1 and 2 are taken as equal when only one value is given.

[b]Subsequent to the data analyses reported here, a further computation has indicated that for this family of reactions, a reasonable fits can also be achieved by an even narrower T(θ) distribution coupled with a broader O(u) distribution;

	T(θ)				O(u)	
	θ_1/θ_2	H_1/H_2	C_1/C_2	U_1/U_2	n_1/n_2	m_1/m_2
Ba	0	10	.2	1.2	2	1/2
Sr	0	10	.2	1.2	2	1/2
Ca	0	10	.4	1.25	2	1/2

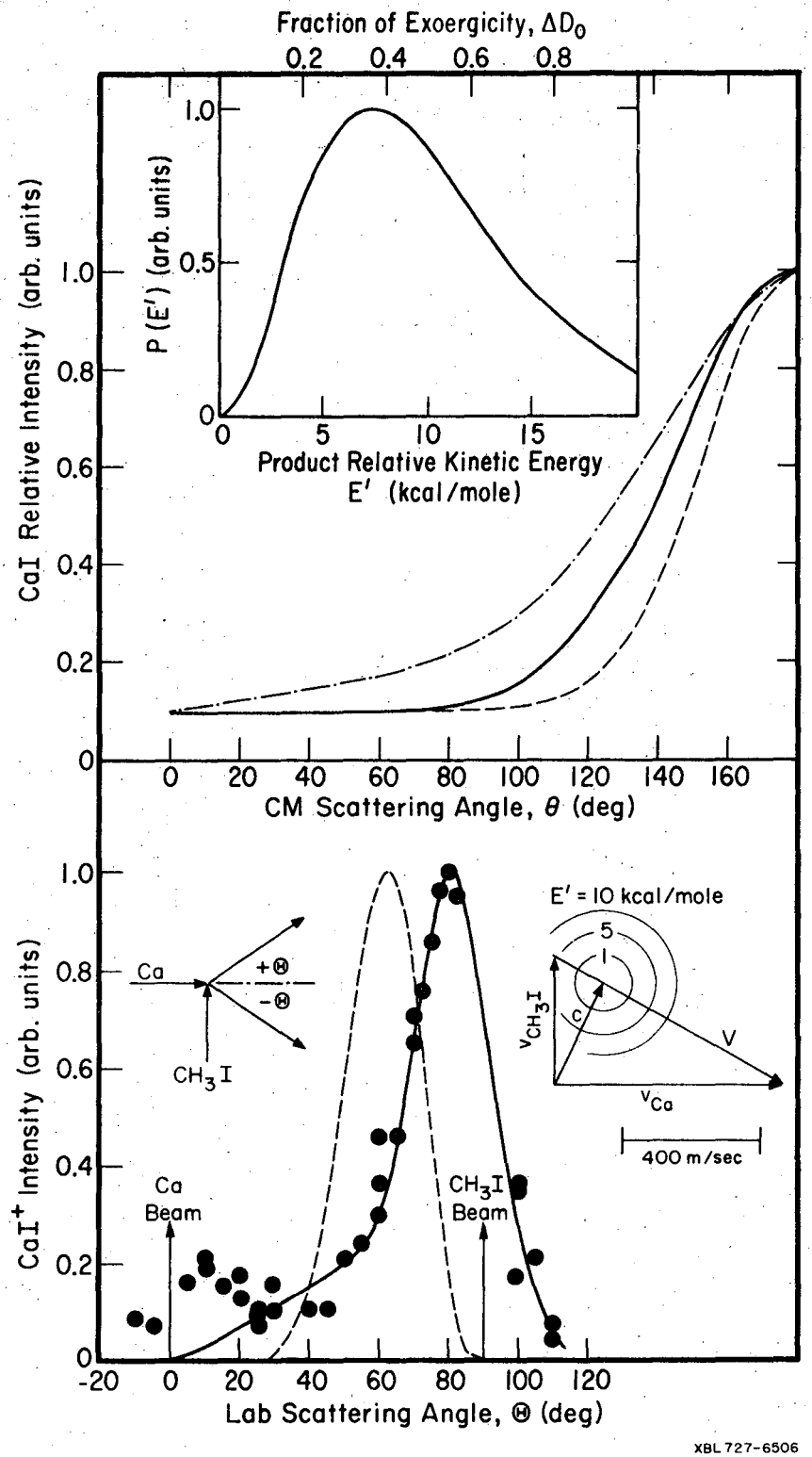

Fig. 1. Product LAB angular distributions and CM recoil functions for the Ca + CH_3I reaction (one run). Format is as it was described for Fig. 1. in the previous chapter.

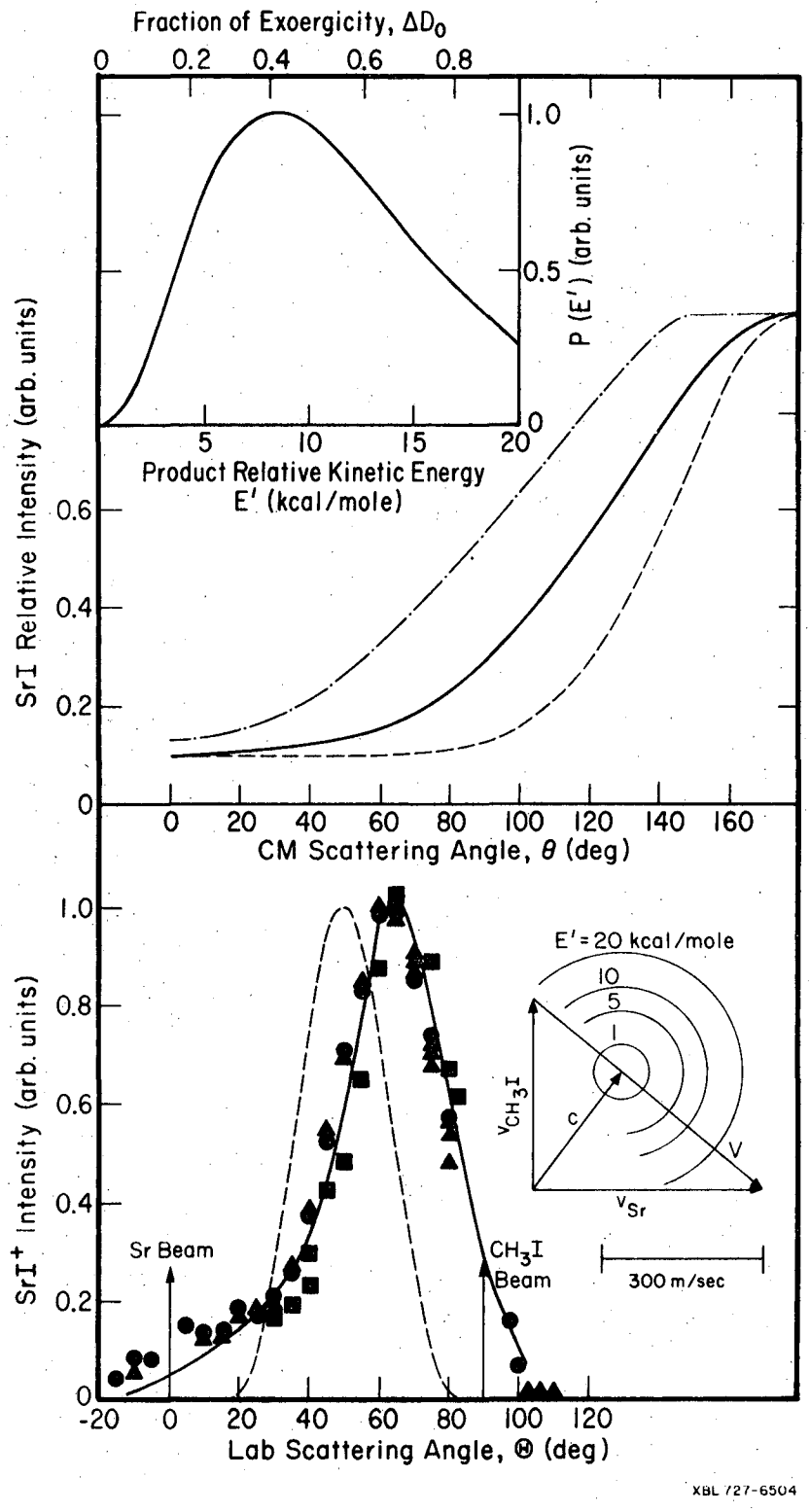

Fig. 2. Product LAB angular distributions and CM recoil functions for the Sr + CH_3I reaction (3 runs).

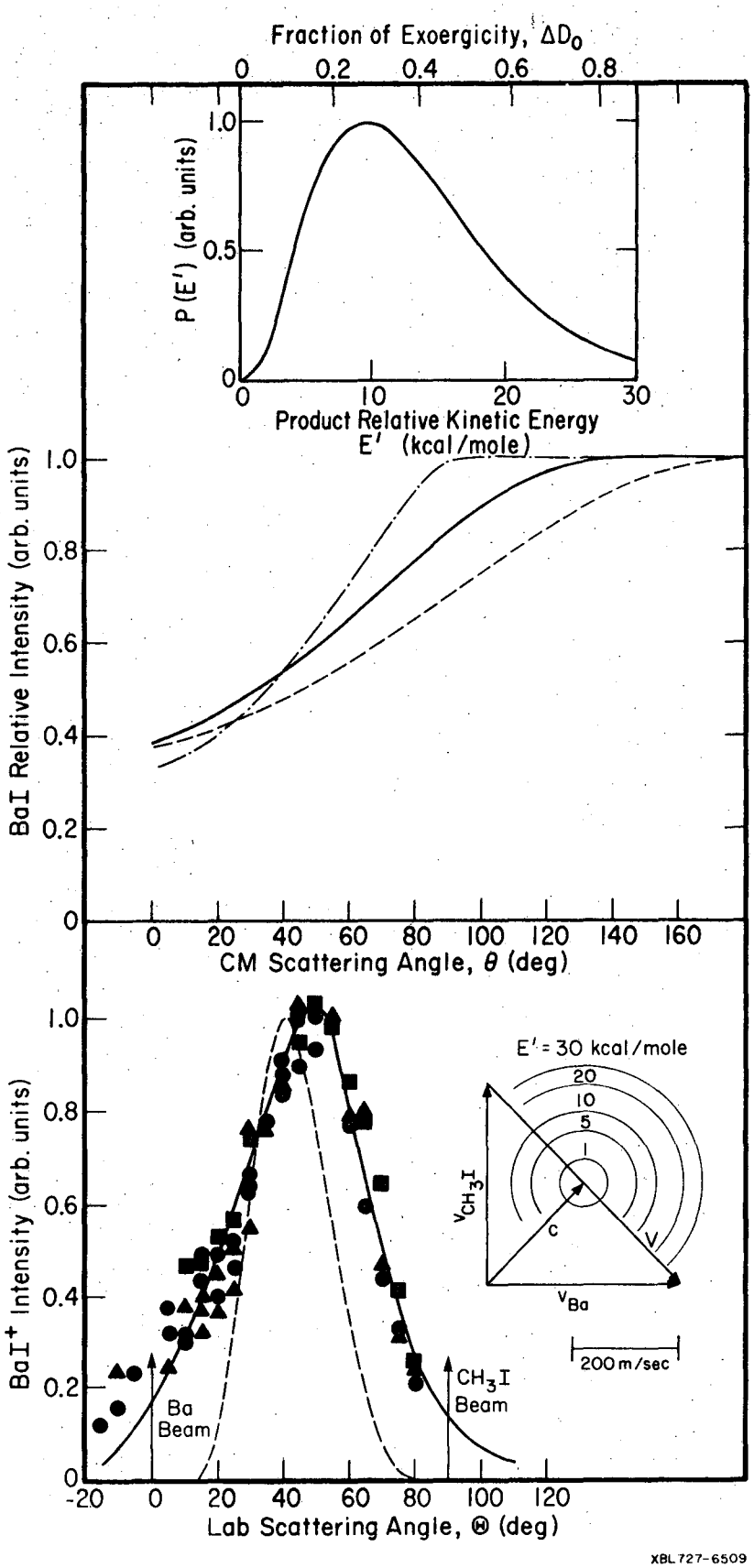

Fig. 3. Product LAB angular distributions and CM recoil functions for the Ba + CH_3I reactions (3 runs).

Table IV. Results of data analysis of the CH_3I reactions.[a]

	Ca	Sr	Ba	K	C_s
E[b]	2.8	2.5	2.6		
ΔD_o[c]	23	26	34		
E'[d]	7.1(8)	8.1(10)	9.3(10)		
Q_b[e]	0.78(0.74)	0.77(0.70)	0.59(0.58)		
MU[f]	286(318)	305(342)	332(370)	332(398)	449(573)

[a]Energies are given in kcal/mole. Momentum given 10^4 gm-cm/sec/mole.

[b]E is the characteristic initial relative kinetic energy, calculated for the most probable beam speeds.

[c]Bond strengths are taken from: for MeI, A. G. Gayton, Dissociation Energies and Spectra of Diatomic Molecules. 3rd ed. (Chapman and Hall Ltd., London, 1968); for CH_3I, B. de B. Darwent, Bond Dissociation Energies in Simple Molecules. Natl. Bur. Std. U. S. Report NSRDS-NBS 31, 1970.

[d]Product recoil energies are calculated from the P(E') distributions obtained from the stochastic method; values in the parenthesis are obtained from the SRE approximation.

[e]The backward contribution, Q_b, is calculated from $Q_b \equiv \int_{\pi/2}^{\pi} T(\theta) \sin\theta d\theta / \int_o^{\pi} T(\theta) \sin\theta d\theta$ for both stochastic and SRE methods; the latter is quoted in parenthesis

[f]CM momentum of product detected. These values are calculated from the peaks in either the P(E') or O(u) distribution; the latter are represented in parenthesis. For comparison, we also present the experimental data for K and C_s + CH_3I reactions from both P(E') and O(u) distributions (E. A. Entemann and D. R. Herschbach, Disc. Far. Soc. 44, 289, (1967)). Model calculations predict 456 and 453 × 10^4 gm-cm/sec/mole for K + CH_3I and C_s + CH_3I, respectively (see D. D. Parrish, Ph.D. thesis, University of California, Berkeley, Ca. 1970).

an intensity at Θ = 20°-60°. Experimentally, no impurity was observed in the CH_3I beam; however, product CaI^+ signal was so small that those data taken at Θ less than 25° were measured at a longer time constant (τ = 3 sec and 12 db) so that the small hump at Θ near the atom beam is presumably due to an experimental error.

The normal modes calculations[3] which were made to correlate the family of reactions of Cs with alkyl iodides indicate that a large fraction (19 kcal/mole) of the reaction exoergicity is required to be initially dissipated as repulsive in the I-C bond during the course of reaction. Accordingly, one may expect that an activation barrier may exist for this family of reactions which are characterized by reaction at small impact parameters (therefore small reaction cross section); indeed, we have observed no detectable product for Mg + CH_3I where the reaction exoergicity is nearly neutral (ΔD_o = 1 ± 10 kcal/mole, see references listed in Table IV). This model calculation also predicts that a larger reaction cross section may be expected for the reaction which has the larger exoergicity. These features combined with the trend that a small cross section would faster the backward scattering are in good agreement with the results reported here.

A recent study of the K + CH_3I[2] reaction shows a strong energy dependence of the reaction cross section at the energy E = 0.1 - 1.0 ev studied; the measured total reaction cross section rises to a maximum at E = 0.18 ± 0.03 ev, beyond which it decreases continuously. We have

used this reported reaction cross section function, Q(E),* to calculate the LAB distribution with our best fit parameters of $T(\theta)$ and $O(u)$ distributions; however, results of these calculations show no conceivable change for all three reactions. This behavior that $T(\theta)$ and $O(u)$ distributions are relatively insensitive to collision energy is also indicated in the $K + CH_3I$ reaction.[2]

According to the impulsive limit model developed in Ref. 3, the product CM momentum would remain almost constant regardless of the mass of attacking atom. A possible explanation for the slight decrease of the product CM momentum with decreasing mass of reacting atoms which is shown in Table IV is that the lighter atoms interact in a more complex manner, thereby deviating further from the impulsive limit than would be the case for the heavier atoms.

2. CH_2I_2 + Ca, Sr, and Ba.

In this family of reactions, the only product detected in the mass spectrometer is the monoiodide ions. However, since symmetry arguments allow transfer of two iodine atoms, we have analyzed the data for both monoiodide and diiodide products. The difference between these two products is the restriction imposed by the conservation law of linear monentum in the CM system, i.e., that for a given product recoil energy, the magnitude of the radical recoil velocity is dependent on

---

*It was approximated from Fig. 10 of Ref. 2 as

$$Q(E) = 2.357\ E^{1/2} \qquad E \leq E^* = 0.18 \text{ e.v.}$$

$$= 0.25 + \exp(-49.328\ E^3) \qquad E > E^*$$

which iodide compound is produced. Consequently, the same set of $T(\theta)$ and $O(u)$ distributions produce the same data fit regardless of which product (monoiodide or diiodide) is assumed. Results are shown in Fig. 4-6 and Table III.

Forward scattering is found for all three reactions. The same set of $T(\theta)$ and $O(u)$ distributions gives an equal good fits to both the Ba and Sr reactions but too much intensity at small Θ for Ca. When this $T(\theta)$ distribution is retained, the calculated LAB intensities always exhibit a little too small a breadth for Ca with its peaking position dependent of the parameters used for the $O(u)$ distribution. As a result, the $T(\theta)$ distribution for Ca possesses a larger fraction at large θ than does that for Ba and Sr. Although the same set of $O(u)$ distributions is used for both diiodides and monoiodides, there is a tremendous difference in the $P(E')$ distributions; these are shown in the upper panels.

The SRE results shown in Fig. 4-6 indicate a sideway peaking ($\theta = 50°$) with a smaller fraction at $\theta = 0°$ for Ca than Ba and Sr. However, this sideway peaking is less significant for Ba and Sr. When $T(\theta)$ is made flat from $\theta = 0°$ to $50°$, reasonable fits are also achieved for Ba and Sr but a significant shift toward small Θ with a smaller breadth near the peak is observed for Ca. However, as indicated in Table III, the subsequent calculations by assuming a narrower $T(\theta)$ distribution coupled with a broader $O(u)$ distribution (i.e., more weight at low velocity portion) also show a reasonably good fits to our measured values. Thus, the actual CM scattering patterns are only

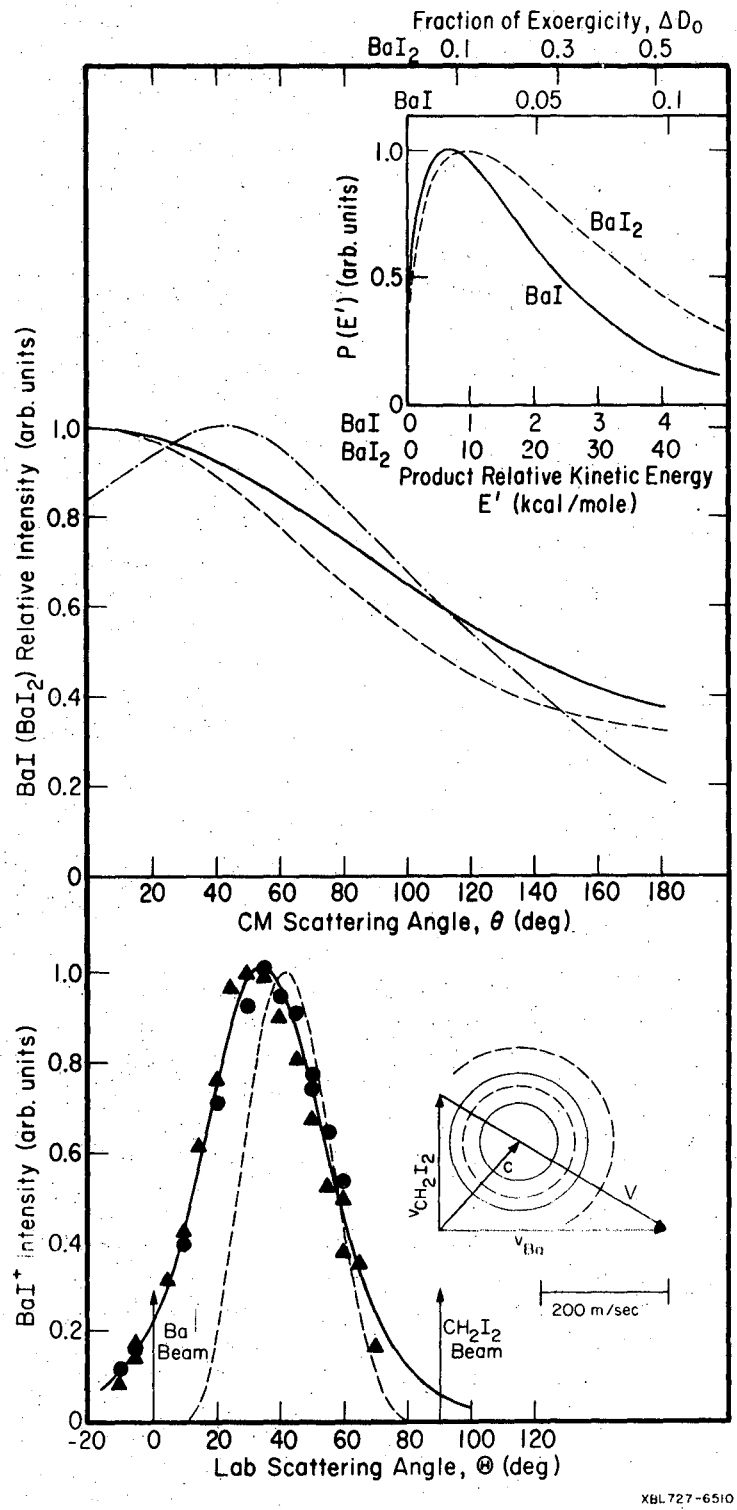

Fig. 4. Product LAB angular distributions and CM recoil functions for the Ba + CH_2I_2 reaction (2 runs). The Newtonian diagram shown at the bottom panel is shown for both BaI (solid circles for E' = 0.3 and 1 kcal/mole) and BaI_2 (dashed circles for E' = 10 and 30 kcal/mole).

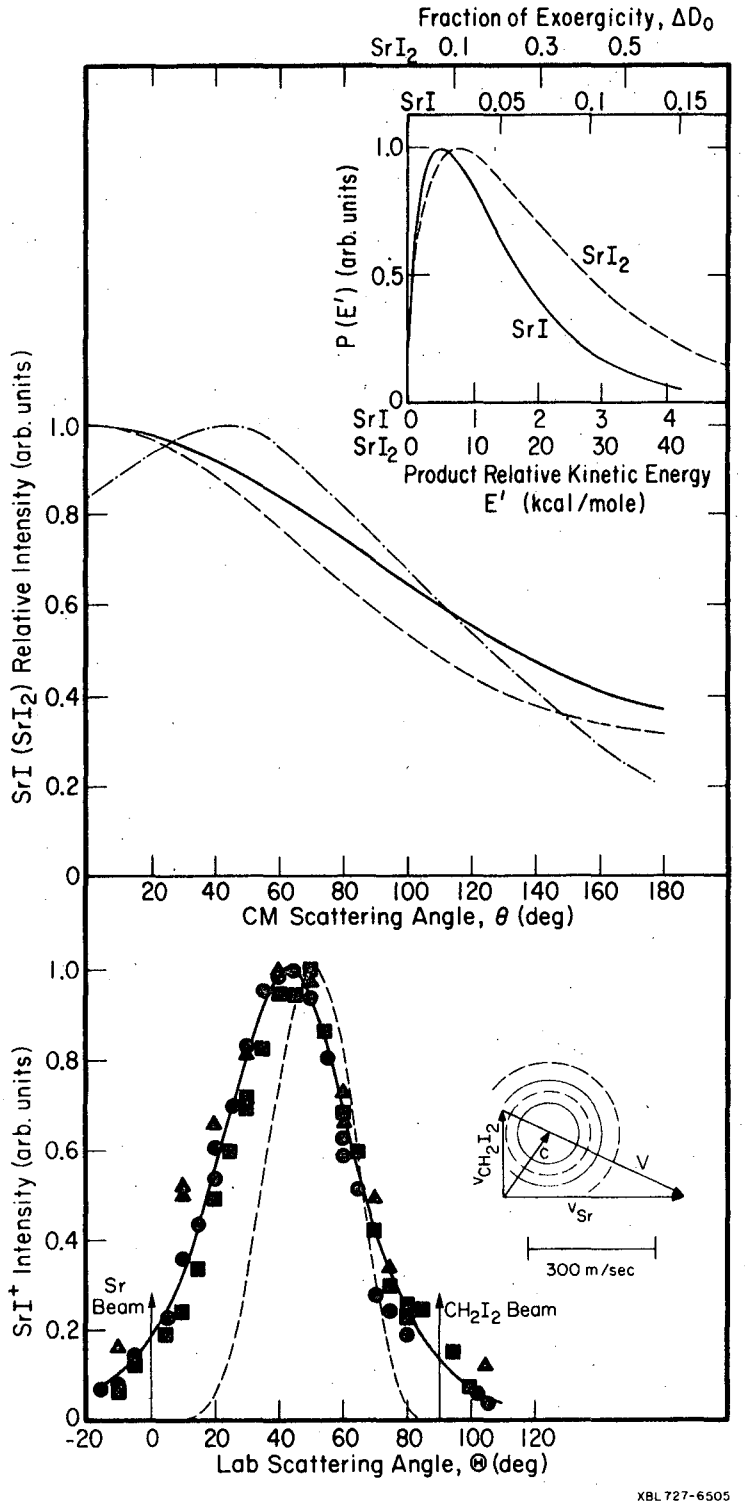

Fig. 5. Product LAB angular distributions and CM recoil functions for the Sr + CH_2I_2 reaction (3 runs). The Newtonian diagram is shown for SrI (solid circles for E' = 0.3 and 1 kcal/mole) and SrI_2 (dashed circles for E' = 10 and 30 kcal/mole).

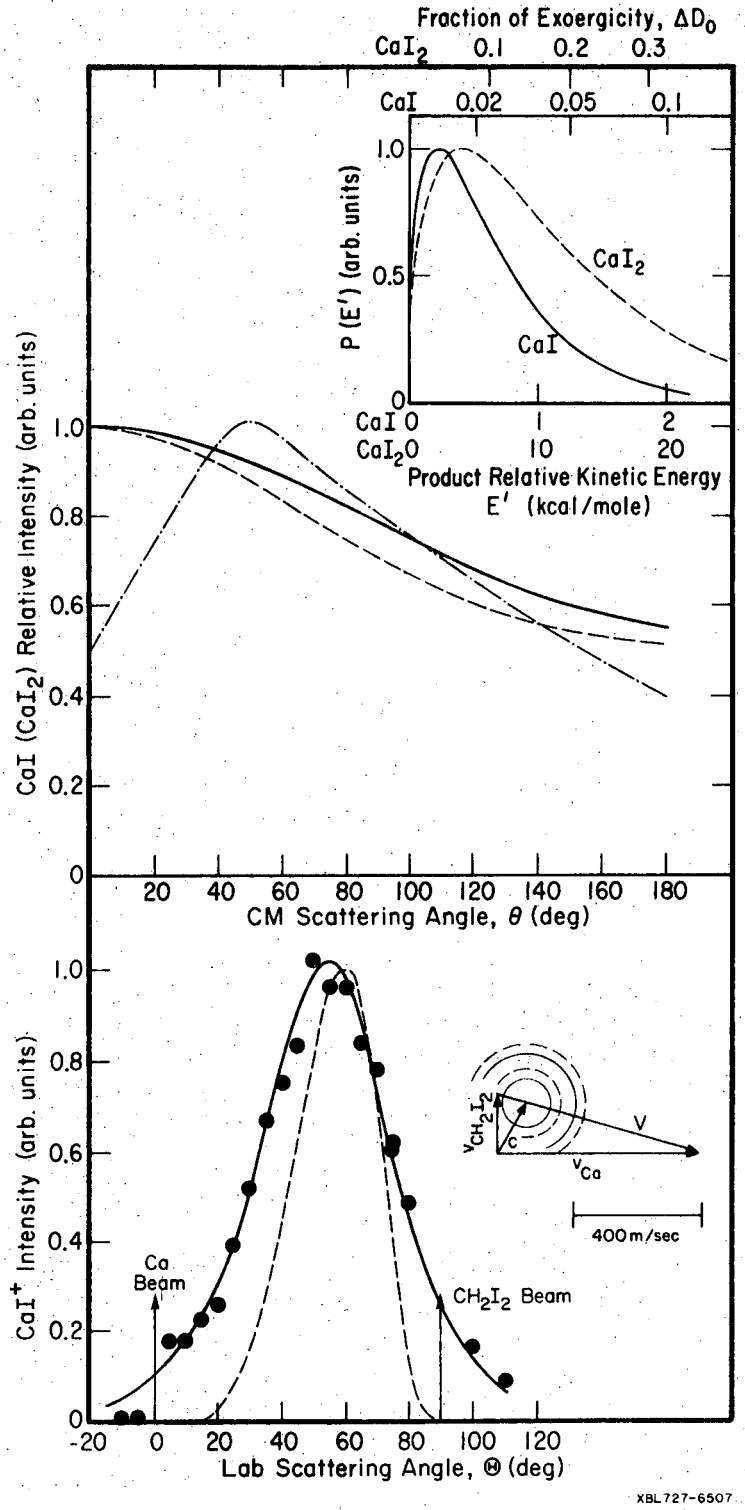

Fig. 6. Product LAB angular distributions and CM recoil functions for the Ca + CH_2I_2 reaction (1 run). The Newtonian diagram is shown for CaI (solid circles for E' = 0.2 and 1 kcal/mole) and CaI_2 (dashed circles for E = 8 and 25 kcal/mole).

poorly characterized by the measured LAB angular distribution alone so that further quantitative comparisons could be misleading. Nevertheless, results from the two extreme scattering patterns, shown in Table V, clearly indicate that the forward contribution for Ca does indeed decrease in comparison with that for Ba and Sr.

The product recoil energies shown in Table V are extremely small if the products are the monoiodide, this small product recoil energy has never been previously observed in crossed beam studies. Moreover, the electron capture experiment[12] on $CH_2I_2 + e^- \rightarrow CH_2I + I^-$ at A.P. (appearance potential) = 0 ev shows that 4.2 kcal/mole of the total available energy (21.6 kcal/mole) appears to be the translational energy of recoil products. Thus, for a more exothermic reaction, one would not expect E' to be much smaller than this value. In light of this argument, the formation of the diiodide product seems more likely for these reactions. Moreover, the MeI_2 product which would form in these reactions would be very highly excited and would be expected to form MeI^+ ion in the mass spectrometer.

To complete this section, we would like to make some remarks on the experimental evidence found for molecules closely related to CH_2I_2: CH_2Br_2 and CH_2BrCl. Product angular distributions have been measured for the Ca + CH_2Br_2 reaction. Because the product yield ($CaBr^+$ ion) is smaller than the case for Ca + CH_2I_2, the scattered data are rather noisy and only a qualitative comment will be given here. The LAB angular distribution is very broad and peaks around $\Theta \sim 40°$-$110°$ (subject to large experimental error). By comparing with the centroid

Table V. Results of data analysis for forward and sideway scatterings.[a]

System	E[b]	ΔD_o[c,d]	E'[d]		Q_f[e]	
			stochastic	SRE	stochastic	SRE
CH_2I_2[f] + Ba	2.39	37(70)	0.64(9.5)	0.7(10)	0.61	0.64
Sr	2.31	29(59)	0.46(7.3)	0.6(8)	0.61	0.64
Ca	2.63	26(54)	0.20(3.8)	0.3(5)	0.57	0.59
$(CH_3)_2CHNO_2$ + Ba	2.44	80	3.4	3	0.68	0.69
Sr	2.32	45	1.4	2.5	0.56	0.61
CCl_3NO_2 + Ca	2.77	26	1.8	3	0.57	0.63
CCl_4 + Ba	2.65	37	4.0	10	0.69	0.72
CF_3I + Ba	2.61	31	9.0	6	0.58	0.56

[a] Energies are given in kcal/mole.

[b] E is the characteristic initial relative kinetic energy, calculated for the most probable beam speeds.

[c] Bond strengths are taken from: for MeI and MeO, A. G. Gayton, Dissociation Energies and Spectra of Diatomic Molecules 3rd Ed. (Chapman and Hall Ltd., London, 1968); for MeI_2, L. Brewer, Chem. Rev. 63, 111 (1963); for MeCl, P. L. Hildenbrand, J. Chem. Phys. 52, 5751 (1970); for CH_2I_2, S. Furuyama, et.al. Intern. J. Chem. kinetics, 1, 283 (1969); for $(CH_3)_2CHNO_2$, CCl_3NO_2 (estimated from CH_3NO_2 and CCl_4, respectively), CF_3I, and CCl_4, V. I. Vedeneyer, et.al. Bond Energies, Ionization Potentials and Electron Affinities (Edward Arnold Ltd., London,1966).

[d] The values indicated in parenthesis refer to the diiodide products.

[e] $Q_f \equiv \int_o^{\pi/2} T(\theta) \sin\theta d\theta / \int_o^{\pi} T(\theta) \sin\theta d\theta$

[f] In accord with the remarks made in Table III, the Q_f value calculated from the stronger forward scattering pattern is 0.53, 0.53, and 0.51 and the corresponding E', 0.33 (4.9), 0.23 (3.7), and 0.17 (3.0) kcal/mole for Ba, Sr, and Ca, respectively; the values denoted in parenthesis for E' are again for the diiodide products.

distribution (which peaks at $\Theta = 60°$), one may expect the ratio of forward/backward contribution in the CM coordinate system to be comparable, suggestive of a sideway peaking (or an isotropic distribution). This feature of a decrease in the forward contribution for CH_2Br_2 relative to CH_2I_2 has also been observed for alkali reactions.[4] For CH_2BrCl, we have observed a very weak $BaBr^+$ signal, but no $BaCl^+$, in the Ba + CH_2BrCl reaction. These results are well in accord with the cross sections reported for C_s and K reactions:[4] $Qr(CH_2I_2) > Qr(CH_2Br_2) \gg Qr(CH_2Cl_2)$.

3. $\underline{C\ Cl_4,\ CF_3I + Ba}$.

Figure 7 shows the kinematic results for the Ba + $C\ Cl_4$ reaction. Using the stochastic procedure, the best-fit $T(\theta)$ distribution peaks sideway at $\theta = 30°$; however, a reasonably good fits is also achieved with a forward peaking. On the other hand, the SRE procedure can only yield a sideway peaking at $\theta = \sim 50°$; in this method, the LAB angular distribution is so sensitive to the peaking angle of $T(\theta)$ that a shift of 10° toward either direction fails to produce a good fits to the measured values. Moreover, in the range $E' = 5$-15 kcal/mole, a second peak in the LAB distribution at $\Theta \simeq -25°$ always appeared in the SRE method even for a $T(\theta) = 0$ at $\theta = 0°$, which is in constrast to the stochastic method from which no double peaks occurred. Since there is an indication[7] of a strong coupling between $T(\theta)$ and $O(u)$ distributions for the alkali + $C\ Cl_4$ reactions, the quantitative $T(\theta)$ form can not be determined from the measured LAB angular distribution alone, because of the possibility that this coupling also happens in the Ba reaction studied here.

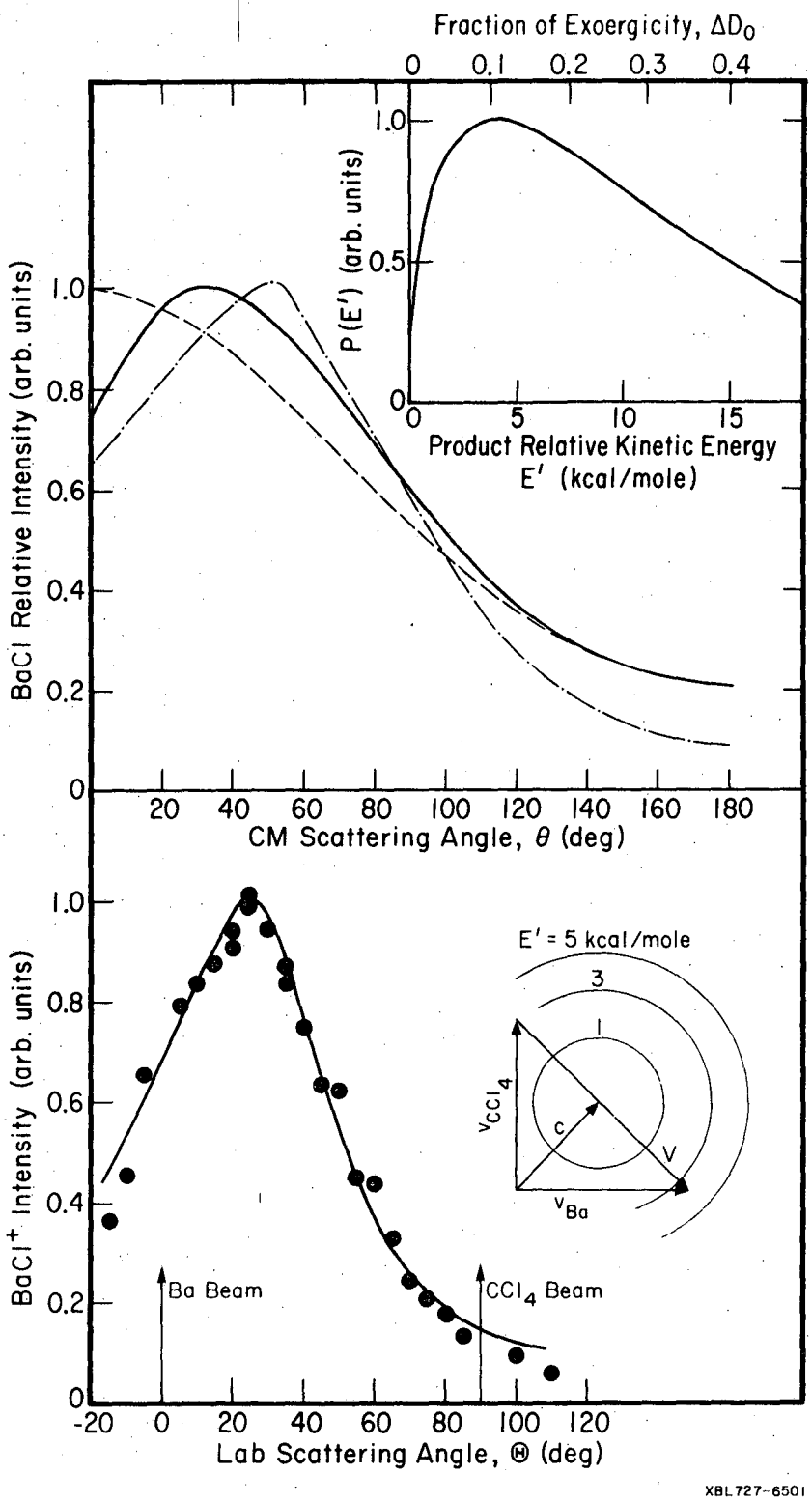

Fig. 7. Product LAB angular distributions and CM recoil functions for the Ba + C Cl_4 reaction (one run).

Experimentally, we have not observed a product $BaCl_2^+$ mass peak for the Ba + C Cl_4 reaction; an earlier discussion made in the previous chapter, however, pointed out that this does not preclude a $BaCl_2$ product. If the product $BaCl_2$ is assumed here, the product recoil energy E' = 6.9 kcal/mole is expected for a reaction exoergicity ΔD_o = 80 kcal/mole whereas the T(θ) distribution remains the same as we discussed in the last section. Besides Ba, we have also tried to react C Cl_4 and C Cl_3Br with Ca; however, neither a $CaCl^+$ nor a $CaBr^+$ mass peak has been detected. It should also be pointed out that the failure to observe a $SrCl^+$ mass peak (m = 122) from Sr + C Cl_4 might have resulted from the mass interference of C Cl_3^+ (m = 117) which resulted from ionization of the C Cl_4 beam; the latter produced a background about two order of magnitude higher than the expected $SrCl^+$ signal level. In the present apparatus where the detection system is referenced to the chopping frequency of the gas beam mass differences of 6 amu or less cannot be completely resolved if the two species have the same modulation.

For CF_3I + Ba, there are four possible channels leading to an exoergic reaction: BaI, BaF, BaF_2, and BaIF.[13] Experimentally, in addition to a bimodal LAB angular distribution of BaI^+ product signal, we have also observed a very weak BaF^+ signal at LAB angle Θ = 10°-30°. Moreover, there was a large background noise around the BaF^+ (m = 156) mass peak and it increased with increasing Θ (i.e., toward the crossed beam) suggesting a mass interference from CFI^+ (m = 158). The ratio of product intensity of BaF^+/BaI^+ observed is smaller than 1:10 at

Θ = 10° and essentially becomes zero at Θ = 30°, one would expect that for the Ba + CF_3I reaction, the products BaI + CF_3 should be more favorable than the other three reaction channels. Moreover, measurements of the dependence of the reaction cross section on orientation of CF_3I molecules for the K + CF_3I reaction[9] indicate that the favorable configuration for reaction to take place is for the K atom to initially approach the more electronnegativity of the F atom according to the electron transfer model. In connection with this model, one would also expect that the small yield of BaF^+ might arise from the product BaF or BaF_2 rather than BaIF.

Figure 8 shows the bimodal LAB angular distribution of BaI^+ product signal and the kinematic results obtained by postulating that this BaI^+ signal is due to ionization of a BaI. The CM angular distribution exhibits a sideway peaking at θ = 60°-90°. In the stochastic method, any $T(\theta)$ distribution peaking outside of this range would result in a LAB angular distribution with a single peak around the centroid. Also, we have to use a rather narrow O(u) distribution in order to produce the bimodal structure of the measured angular distribution.

4. $(CH_3)_2$ $CHNO_2$ and CCl_3NO_2.

Measurements of product angular distributions have been attempted for $(CH_3)_2$ $CHNO_2$ with Ba, Sr, and Ca. For Ba and Sr, product angular distributions have been collected for BaO^+ and SrO^+ detector signal, respectively; no other product ions have been seen in the mass scans. For Ca, we have not observed any product signal. Although the formation

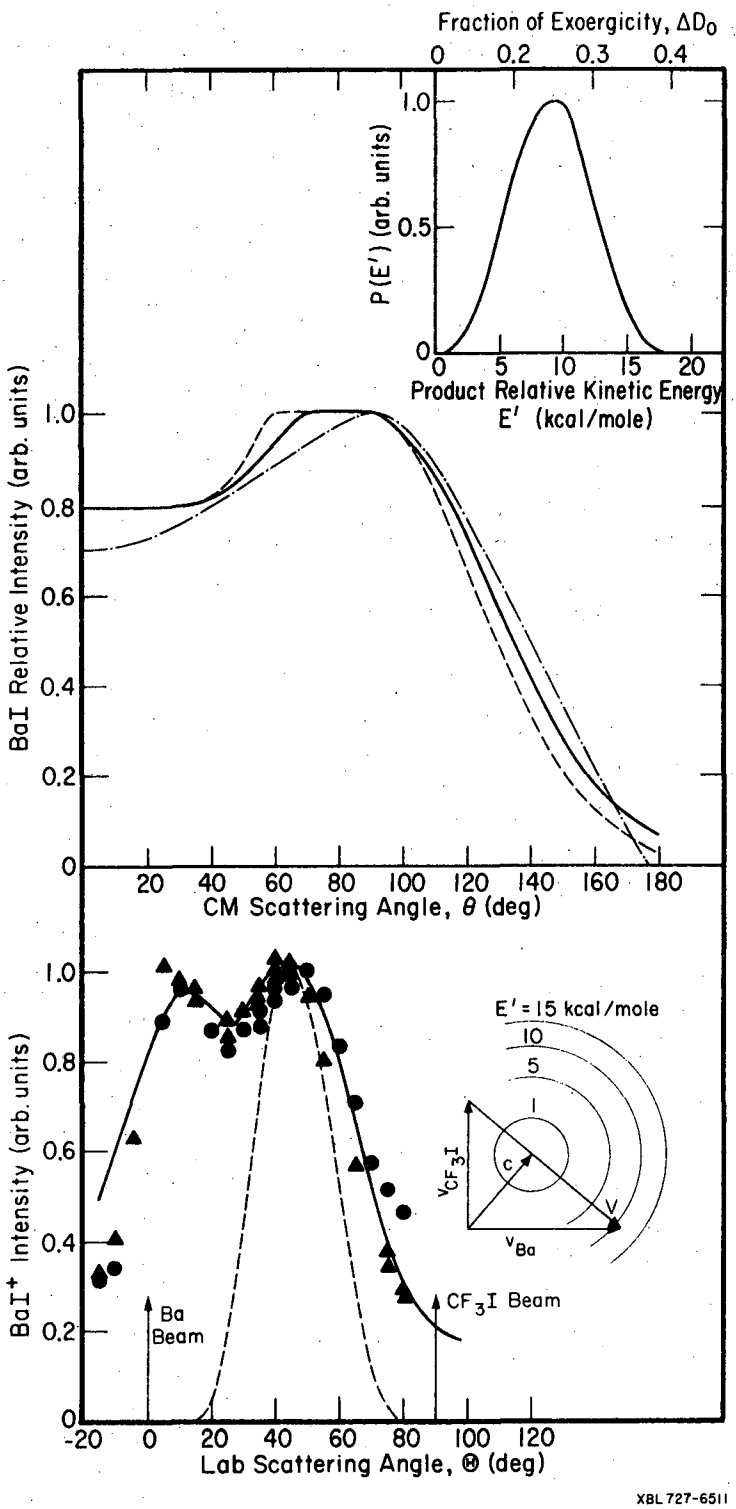

Fig. 8. Product LAB angular distributions and CM recoil functions for the Ba + CF_3I reaction (2 runs).

of $MeNO_2$ is probably an exoergic reaction, the formation of the oxide product is expected to be more exoergic. Moreover, the steric effect also favors formation of the oxide product because reaction occurs instaneously when Ba or Sr approaches to the perimeter of the - NO_2 group. All analyses presented here proceed by considering that the MeO^+ signal comes directly from MeO rather than $MeNO_2$. Figures 9 and 10 show the kinematic results. For this family of reactions, both product LAB angular distributions and CM recoil functions have a great similarity to results found for the Cl_2 and Br_2 reactions, i.e., a sharp CM forward scattering pattern with relatively low recoil energies of the reaction exoergicity. Accordingly, one would expect that a reaction mechanism similar to that of the halogen molecules also occurs here.

This result is in constrast to the results for the Li and K + CH_3NO_2 reactions.[8] These studies indicated a $LiNO_2$ and KNO_2 product on the basis of information provided by magnatic and electric deflection analysis and the product CM angular distribution yielded a comparable intensity in the forward and backward hemispheres. In these studies, the kinematic analysis was handicapped by the large mass ratio of the product detected and the free radical, which made the KNO_2 CM angular distribution rather insensitive to the relative motion of the products. These considerations led to the choice of $(CH_3)_2$ $CHNO_2$ rather than CH_3NO_2 for our alkaline earth studies.

For Ca + C Cl_3NO_2, we have observed both $CaCl^+$ and CaO^+ mass signals. However, the CaO^+ signal is not large enough to scan the

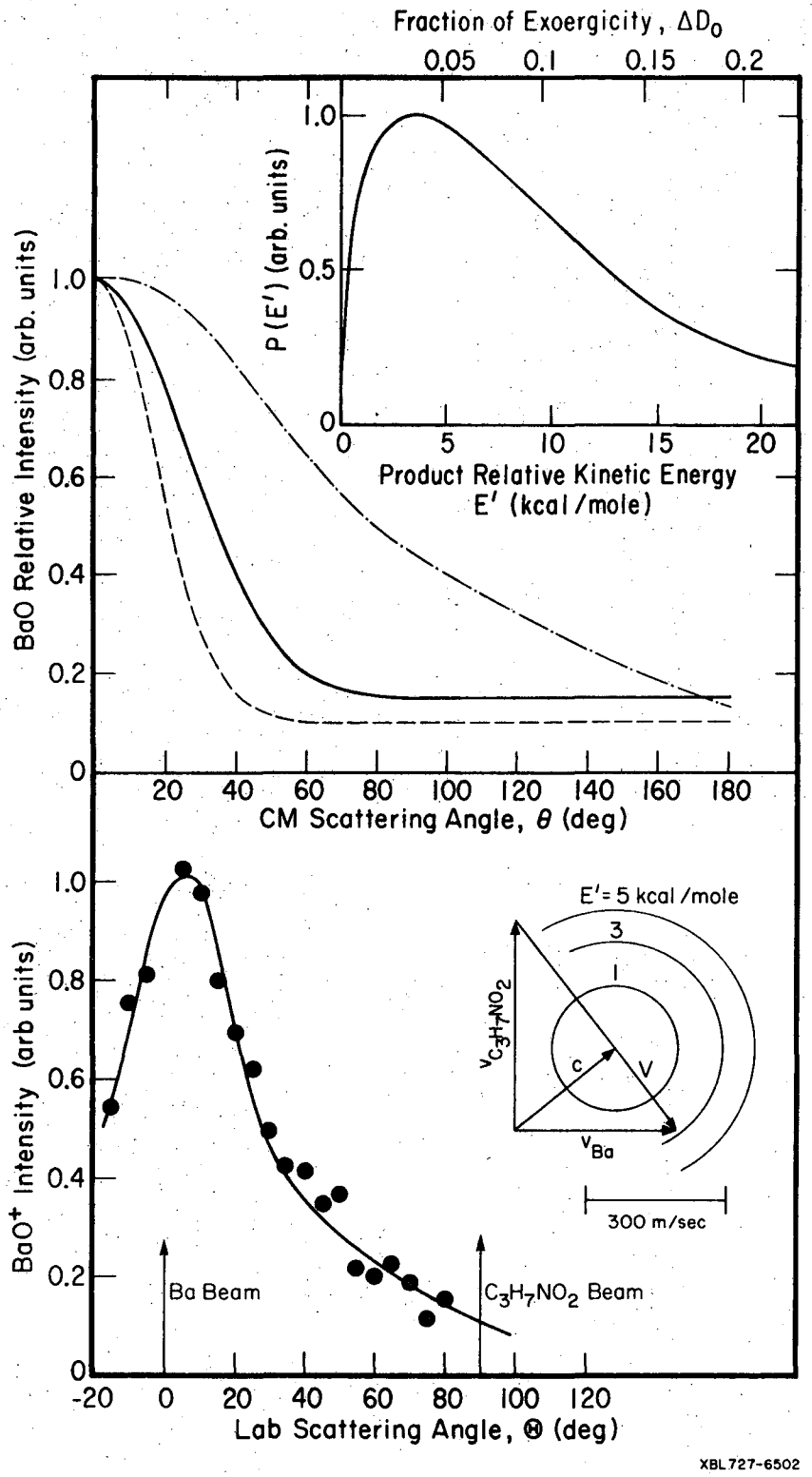

Fig. 9. Product LAB angular distribution and CM recoil functions for the Ba + $(CH_3)_2CHNO_2$ reaction (one run).

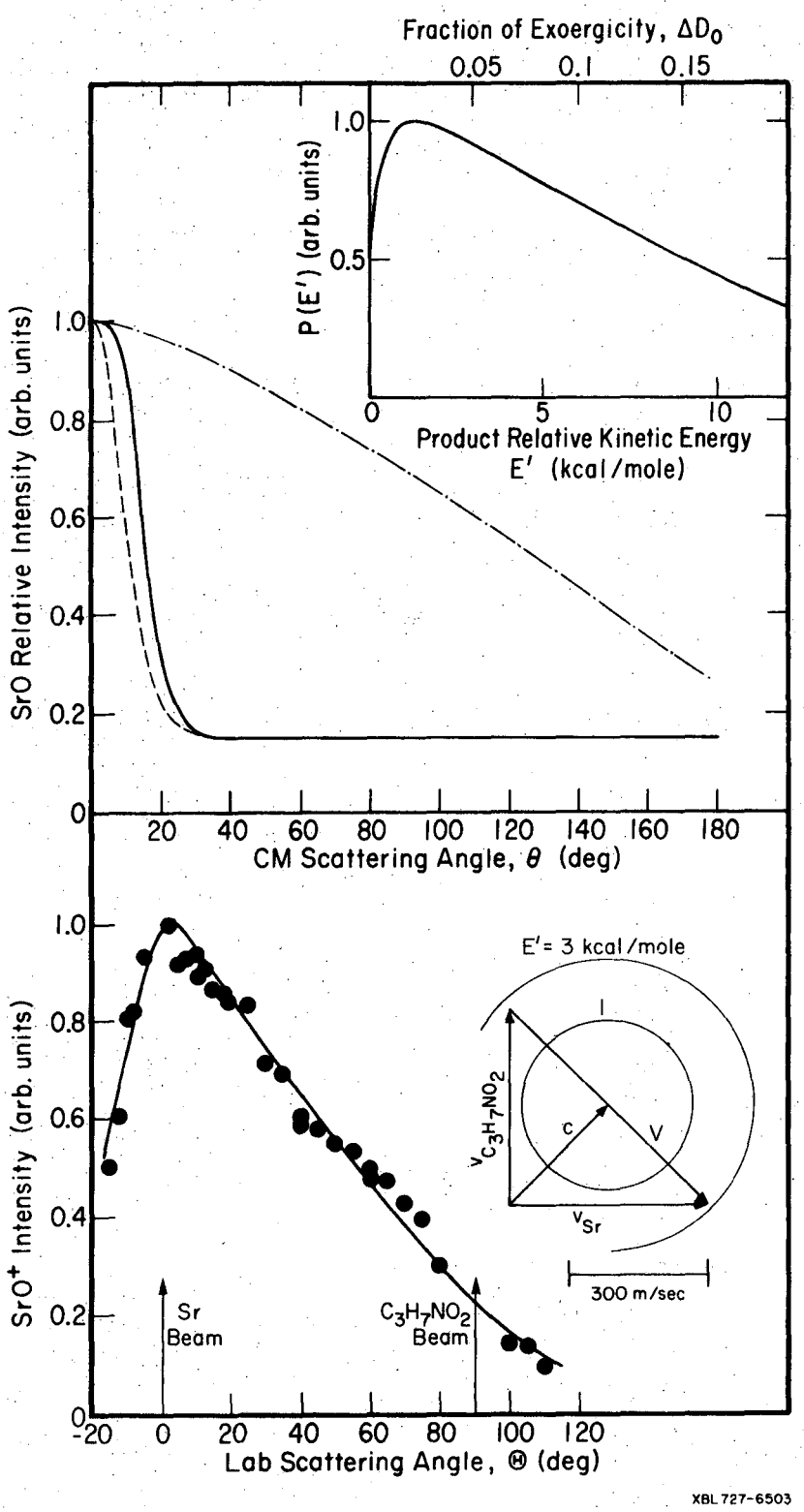

Fig. 10. Product LAB angular distribution and CM recoil functions for the Sr + $(CH_3)_2CHNO_2$ reaction (one run).

angular distribution; for Θ from -10° to 20°, it was measured to be largest at Θ = 5°, the same peaking angle observed for the Ba and Sr with $(CH_3)_2$ $CHNO_2$ reactions. Figure 11 shows the kinematic results for the $CaCl^+$ product. Here again, the CaCl product is predominantly confined in the forward hemisphere with a small fraction of the reaction exoergicity appearing in the product recoil energy. These also resemble results found for the halogen molecule reactions.

We have also measured the scattering from Sr + iso-pentyl nitrite, $(CH_3)_2$ CH $(CH_2)_2$ ONO. Product signals were observed at mass peaks corresponding to SrO^+, $SrNO^+$, and $C_5H_{11}O$ Sr^+; yields of the first two products were comparable and larger than the yield of $C_5H_{11}O$ Sr^+. However, iso-pentyl nitrite is so unstable that the pressure in the collision chamber increased drastically during the experiment; consequently, none of these three product angular distributions has been transformed into the center-of-mass system. Qualitatively, the SrO^+ angular distribution for Θ from -15° to 80° is very similar to the SrO^+ observed for the Sr + $(CH_3)_2$ $CHNO_2$ reaction.

For Ba + tert - butyl alcohol, on the other hand, neither $BaOH^+$, $t\text{-}C_4H_9O$ Ba^+, nor any other scattered product signal was observed although formation of both products, BaOH and $t\text{-}C_4H_9OBa$, is probably exoergic from the reported D_o of 39.1[14] and 104[15] kcal/mole for the C-OH and CO-H bonds, respectively.

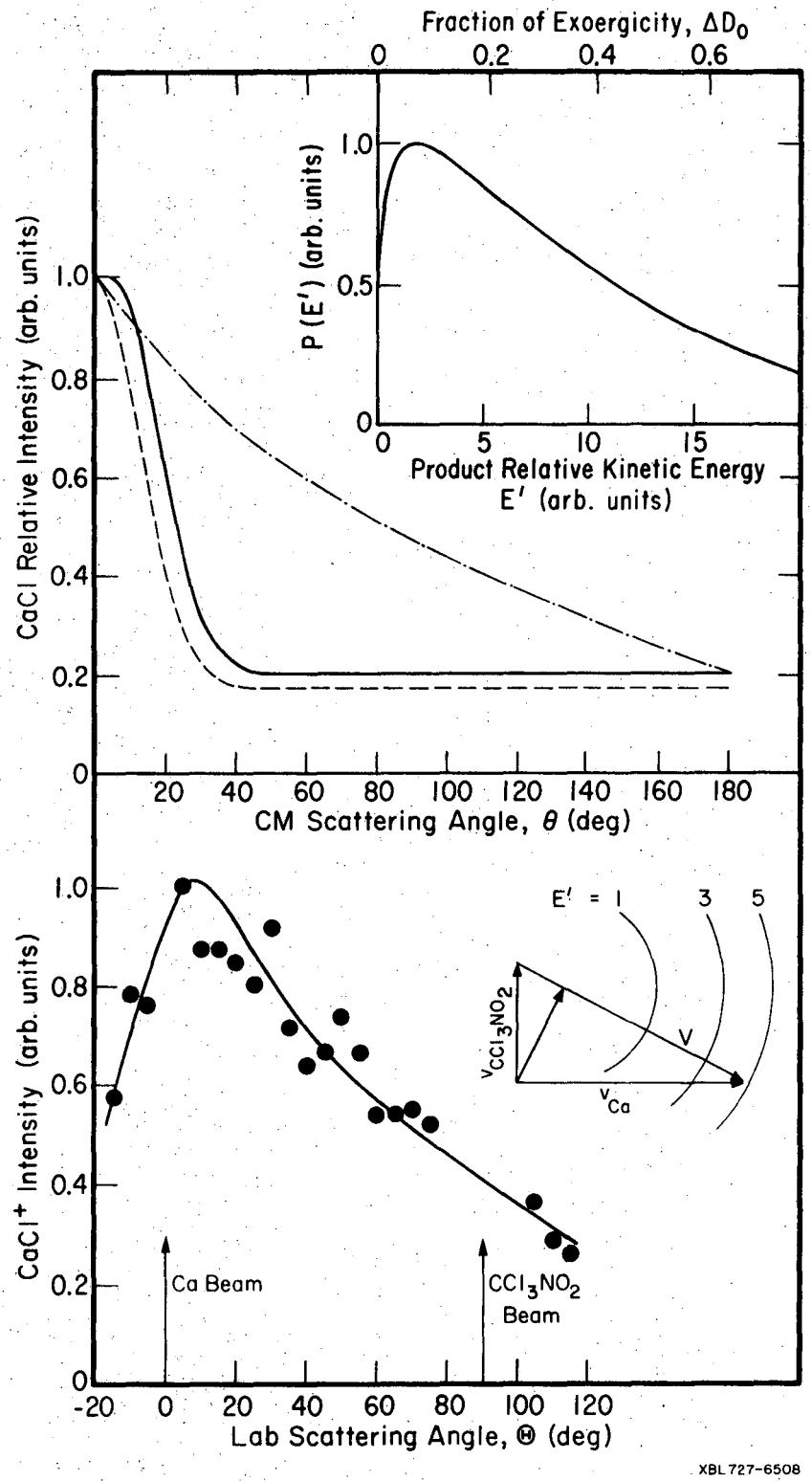

Fig. 11. Product LAB angular distributions and CM recoil functions for the Ca + C Cl_3NO reaction (one run).

E. Summary

For all reactions studied here, an anisotropic angular distribution in the CM coordinate system has been found: a backward scattering for CH_3I, a forward scattering for CH_2I_2, C Cl_3NO_2, and $(CH_3)_2$ $CHNO_2$ and a sideway peaking for C Cl_4 and CF_3I. The main features are summarized as follows:

(1) For the reactions of CH_3I with Ba, Sr, and Ca, a backward scattering in the CM angular distribution with a substantial amount of reaction exoergicity (~ 30-40%) appearing as the product recoil energy is found for all three reactions; this backward scattered component increases in the series Ba, Sr, and Ca. The product CM momentum of MeI is nearly constant for these reactions; this is consistant with the trend predicted by the impulisve limit model calculations.[3]

(2) Experimentally, a large yield at the MeI^+ ion signal in the mass spectrometer was observed for the reactions of CH_2I_2 with Ba, Sr, and Ca. An argument on the magnitude of product recoil energy estimated by postulating that this ion signal arose from either a diiodide or a monoiodide product upon an electron-impact ionization process, however, indicates that the diiodide product seems more likely for these reactions. Since a reasonably good fits to the measured LAB angular distributions is found for a large number of combinations of the CM angle and recoil velocity distributions, the actual CM scattering patterns are only qualitatively achieved. Nevertheless, results suffice us to conclude a forward scattering with relatively low recoil energies (15% of the reaction exoergicity if diiodide product and $< 2\%$ if

monoiodide) for this family of reactions.

(3) For the Ba + C Cl_4 reaction, the product LAB angular distribution was measured for the $BaCl^+$ mass peak. A sideway peaking but possessing a large ratio of forward/backward scattered contribution is found regardless whether this $BaCl^+$ ion signal is due to the ionization of a BaCl or a $BaCl_2$ product. For Ba + CF_3I, a bimodal LAB angular distribution of BaI^+ product signal was observed; in addition, a little BaF^+ mass peak was also found. The kinematic results obtained postulating that the BaI^+ signal has arisen from the reaction product BaI indicate a sideway peaking in the CM coordinate system.

(4) Both $CaCl^+$ and CaO^+ ion signals have been observed for the Ca + CCl_3NO_2 reaction; LAB angular distribution was only measured for the $CaCl^+$ signal since the CaO^+ signal was not large enough to allow a complete scan of angular distribution. A strong forward scattering with low recoil energy was found for the CaCl product. No product signal was observed for Ca + $(CH_3)_2$ $CHNO_2$, however. For Ba and Sr with $(CH_3)_2$ $CHNO_2$, no product signals other than MeO^+ have been found and their kinematic results showed a forward scattering for both reactions.

REFERENCES

1. For an extensive review, see; J. L. Kinsey, Chapt. 6, "Molecular Beam Reactions," in Biennial Rev. of Sci. Tech. and Med. vol. 9, Reaction Kinetic, MTP, Oxford (1972).

2. M. E. Gersh and R. B. Bernstein, J. Chem. Phys. 56, 6131 (1972); and references cited therein.

3. D. D. Parrish and R. R. Herm, J. Chem. Phys. 53, 2431 (1970); and references cited therein.

4. E. A. Entemann, J. Chem. Phys. 55, 4872 (1971).

5. K. R. Wilson and D. D. Herschbach, J. Chem. Phys. 49, 2676 (1968).

6. J. C. Whitehead, D. R. Hardin, and R. Grice, Mol. Phys. 23, 787 (1972).

7. D. R. Herschbach, a private communication.

8. (a) D. D. Parrish and R. R. Herm, J. Chem. Phys. 54, 2518 (1971). (b) R. R. Herm and D. R. Herschbach, J. Chem. Phys. 52, 5783 (1970).

9. R. R. Brooks, J. Chem. Phys. 50, 5031 (1969).

10. J. W. Hodgins and R. L. Haines, Can. J. Chem. 30, 473 (1952).

11. C. A. Mims, Ph.D. thesis, University of California, Berkeley, Ca. 1972.

12. J. J. DeCorpo, D. A. Bafus, and J. L. Franklin, J. Chem. Phys. 54, 1592 (1971).

13. ΔD_o is estimated to be 22, 45, and 46 kcal/mole for product BaF, BaF_2, and BaIF, respectively. D_o is taken from: for CF_3-I and F-CF_2I, S. W. Benson, J. Chem. Ed. 42, 502 (1965); for BaF, D. L. Hildenbrand, J. Chem. Phys. 48, 3647 (1968); for BaF_2 and BaIF (the

latter is evaluated from the expression $\varepsilon = (\varepsilon_{BaF_2}\ \varepsilon_{BaI_2})^{1/2}$), L. Brewer, Chem. Rev. 63, 111 (1963). For product BaI, see Table V.

14. V. I. Vedeneyev, L. V. Gurvich, V. N. Kondratyev, V. A. Medvedev, and Ye. L. Frankevich, Bond Energies, Ionization Potentials, and Electron Affinities (Edward Arnold Ltd. London, 1966).

15. P. Gray and A. Williams, Chem. Rev. 59, 239 (1959).

V. THE FRANCK-CONDON PRINCIPLE AND PHOTODISSOCIATION OF DIATOMIC MOLECULES

A. Introduction

The distributions of spectral intensities in electronic transitions of diatomic molecules have been extensively investigated in terms of the Franck-Condon (FC) principle. Classically, the basic assumption of the FC principle is that the electronic transition takes place essentially instantaneously with respect to the motion of nuclei. Therefore, a molecule undergoing a transition must proceed vertically upward or downward on the potential energy diagram so as to conserve relative internuclear separation and momentum. The quantum mechanical formulation of the FC principle assumes that the transition probability is merely proportional to the square of an overlap integral between the two vibrational states involved; this principle is arrived at by assuming that the matrix element of the electronic transition moment is independent of the internuclear separation. Through this sudden approximation, the spectral intensity distribution of either a molecular band system or a continuous spectrum within an electronic transition is simply the square of the overlap integral or the so-called FC factor.

The FC factor has often been evaluated approximately, if one of the two electronic states involved in the transition belongs to a continuum, by replacing the vibrational wavefunction for this continuum state by a delta function (δ - approximation) located at the classical truning point.[1] Consequently, the δ - approximation provides a FC factor which is simply given by the probability density function of

the bound state. This δ - approximation has been applied to many continuous transitions in diatomic spectroscopy. In the 1930's, Coolidge and James and their associates[2] extensively analyzed the continuous emission spectra of H_2 and of D_2 for the transition $1s\sigma\ 2p\sigma\ {}^3\Sigma_u^+ \leftarrow 1s\sigma\ 2s\sigma\ {}^3\Sigma_g^+$ and concluded that the δ - approximation gives fairly satisfactory results without the detailed summation over rotational states. On the other hand, Doyle[3] in 1968 pointed out that the neglect of rotational dependence of the dipole moment for the H_2 molecules (with the wide spacing of the rotational level) is a major source of error when several rotational states are populated in those states.

Although the δ - approximation has been widely used to extract the repulsive potential of diatomic halides from the measurements of their absorption spectra[4] and atomic resonance line fluorescence,[5] detailed analysis for the validity of this approximation has not apparently reported yet.* The present chapter compares exact and

---

*Subsequent to the work reported here, the author became aware of a recent article (G. H. Dunn, Phys. Rev. 172, 1, 1968) demonstrating that the δ - approximation provides a good estimates of FC factors at low vibrational levels of H_2^+ and D_2^+ molecules if the proper energy normalization is used. Furthermore, E. A. Gislason of the Univ. Illinois--Chicago Circle campus (private communication) has developed an exact series expansion for FC factors, subject only to the assumption of a linear dependence of potential on internuclear distance in the continuum state; the first term in this exact series expansion is the (properly energy normalized) δ - function approximation.

"δ - approximation" of the FC factors for the photodissociation of HI and of NaI molecules. Results are used to construct repulsive potentials. Errors introduced by the δ - approximation are interpreted in terms of the nature of the oscillatory wavefunctions of the continuum state and their positions relative to the bound vibrational wavefunctions. The rotational angular momentum was included in the calculations for HI molecule, but was found to have no significant influence on the distribution of relative intensities. Results from $\bar{r}$-centroid analysis confirmed the applicability of the FC approximation to the HI and NaI transtiions examined here.

B. Computation Methods

Since the FC principle assumes that the variation of the matrix element of the electronic transition moment, $\mu e(r)$, is small that $\mu e(r)$ may be replaced by an average value, $\bar{\mu}e(r)$, the intensity absorbed in an electronic transition is given by[2a]

$$I = CN \left|\bar{\mu}e(r)\right|^2 \nu f \qquad (1)$$

where N is the population of the initial state, ν is the frequency of the transition and C is a proportionality constant. The FC factor, f, for a transition between two states, one of which is a continuum state, may be expressed as

$$f = \left|\langle \varepsilon \mid vj \rangle\right|^2 \qquad (2)$$

where v and j are bound vibrational and rotational quantum numbers; ε, measured from the asymptotic energy of the two atoms which correlate with the repulsive molecular state, is given as

$$\varepsilon = h\nu + \hbar\omega\,(v + \tfrac{1}{2}) - D_e - E^* \qquad (3)$$

In this equation, ω refers to the circular vibrational frequency of the bound state, D_e to its dissociation energy and E^* to the product atomic excitation energy. In order to determine the theoretical distribution of transition probabilities we first have to solve the radial Schroedinger equation for the vibrational wavefunctions for both upper and lower states and then evaluate the overlap integral shown in Eq. (2). The wavefunction of each vibrational-rotational level of the bound state, $|\, vj \,\rangle$, is computed by replacing the radial Schroedinger equation by an equivalent difference equation which is then solved numerically.[6] The radial Schroedinger equation is expressed in the form $d^2\phi/dr^2 = A\phi$ if length and energy are given in dimensionless units. The quantity A is equivalent to $V(r) - \varepsilon$ divided by the unit of energy $\hbar N_o/4\pi c\mu a_o^2$, where $\hbar = 1.05450 \times 10^{-27}$ erg·sec, $No = 6.02257 \times 10^{23}$ mol^{-1}, $c = 2.997925 \times 10^{10}$ cm/sec and μ is the reduced mass. The internuclear separation, r, is in atomic unit (a_o). A program[7] written in machine language IBM 7090 was used in this computation.

For the δ - approximation, the FC factor for a transition to a given eigenvalue of the continuum state, ε, is simply equivalent to the square of $|\, vj \,\rangle$, for that value of r corresponding to the ν given

by Eq. (3). We thus obtain the theoretical transition probability as the product of this probability density function multiplied by the vibrational population and the frequency factor, ν, from Eq. (1).

For the exact evaluation of the FC factors, the vibrational wavefunctions of the continuum state were obtained from a one-dimensional, box (energy) normalized solution to the radial Schroedinger equation for a given trial potential. This box (energy) normalized solution is formulated by assuming that the particle is not free to the entire space but is confined in a box with rigid walls at large distance. It is so large that the physical situation under consideration is not sensibly affected and the continuum states are then replaced by a discrete infinity of energy states. Using the summed form of the Numerov method,[8] the computation of non-normalized continuum wavefunctions was carried out to a distance of $\sim 12\ a_o$, where the wavelength and peak amplitude had reached a constant value and the wavefunction itself essentially behaved as a sine wave. This asymptotic peak amplitude was normalized to unity and the final energy normalized wavefunction[2a] was obtained by dividing this function by the square root of the energy density of the continuum state (i.e., $\varepsilon^{1/4}$).

A program was written to compute the FC factors and the distribution of transition probabilities from either the δ - approximation or the exact FC calculation; it was run on the CDC 6600 computer at the Lawrence Berkeley Laboratory. The step size used in the computation was $0.0040\ a_o$ for HI and $0.0045\ a_o$ for NaI.

C. Bound State Wavefunctions

1. HI Molecules.

The ground state potential was calculated from the RKR (Rydberg-Klein-Rees) procedure.[9] The spectroscopic constants were taken from Ref. (4-c). Figure 1 shows the potential curves generated from the RKR method and the Dunham power series[10] for a rotationless vibrator of HI molecules; a third potential computed from the simple Morse function is also shown in the figure. The RKR potential function is derived from the classical turning point as a function of vibrational quantum number and the Dunham potential was calculated from coefficients a's given for J = 4 in Ref. (4-c) and corrected back to the J = 0 using the formula listed in Table III of Ref. 10. Although the Dunham potential shows the same behavior for $v < 3$ (more than 99.9% of the HI molecules are in the state v = 0 at room temperature), the RKR potential was used to calculate the bound state wavefunctions. A direct numerical integration[7b] was used in this calculation.

2. NaI Molecules.

For a very polar bond such as occurs on the alkali halides, the Rittner classical ionic model[11] has been successfully used in computing the ground state potential near the equilibrium internuclear separation. This potential is given as

$$V(r) = Ae^{-r/\rho} - \frac{e^2}{r} - \frac{e^2(\alpha_+ + \alpha_-)}{2r^4} - \frac{C_6}{r^6} - \frac{2e^2\alpha_+\alpha_-}{r^7} \qquad (4)$$

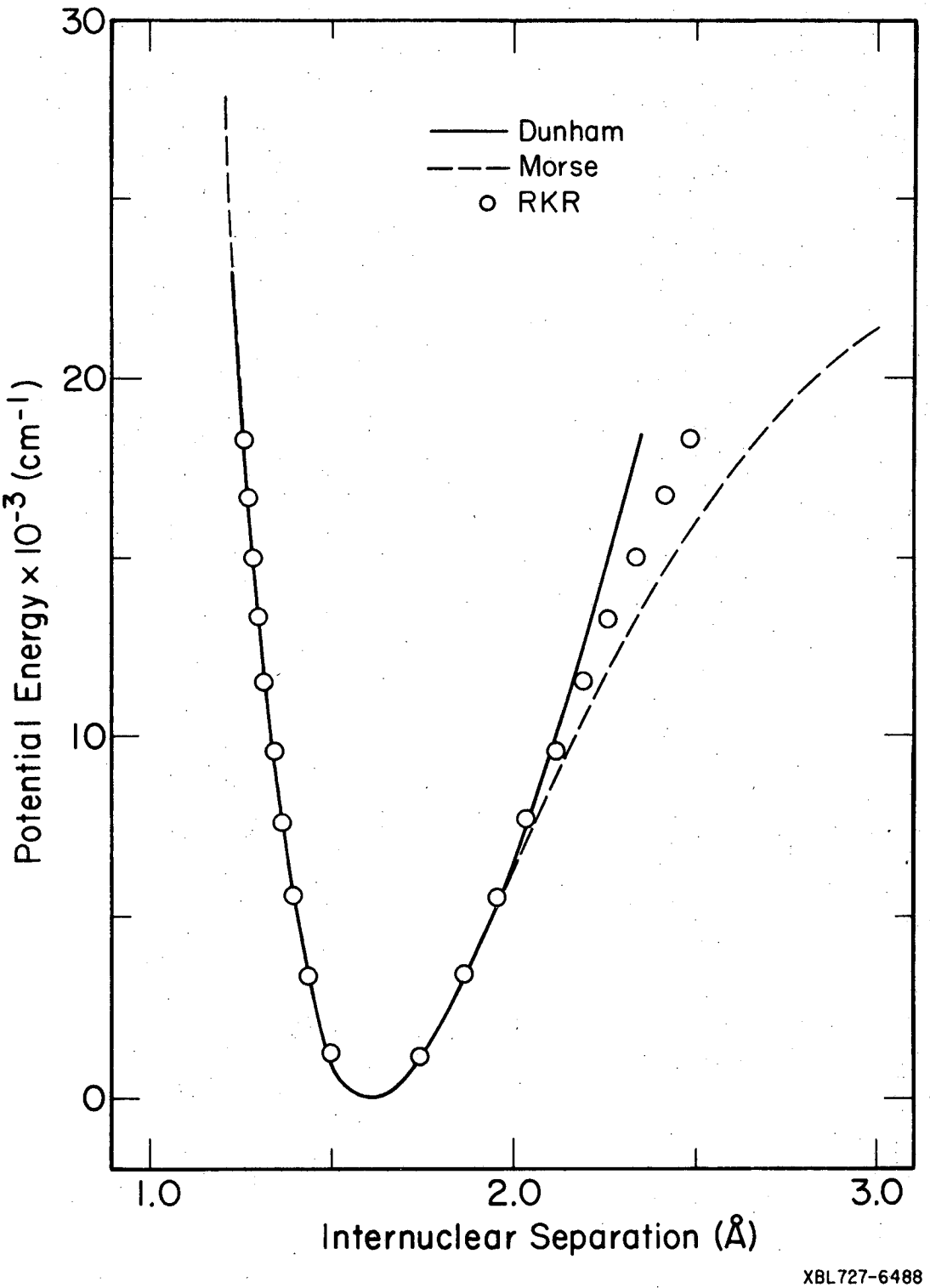

Fig. 1. Ground state potential of HI molecule, calculated from RKR, Dunham and Morse potential functions for a rotationless vibrator.

The successive terms in Eq. (4) describe the short range repulsion, the Coulombic attraction, the ion-induced dipole interaction, the van der Waals attraction and the induced dipole-induced dipole interaction, respectively. The van der Waals force constant, C_6, was calculated from the Slater-Kirkwood approximation[12] for polarizabilities of Na^+ and I^- taken as $\alpha_+ = 0.15$ Å^3 and $\alpha_- = 7.0$ Å^3[13] respectively. The repulsion constants A and ρ were evaluated by requiring that at $r = r_e$ the first derivative of the potential vanish and its second derivative be twice the force constant of the bond (obtained from the reported[14] vibrational frequency). At the temperature employed in measurements of the NaI photodissociation (see Ref. 15 - Appendix A), 633-705°C, vibrational levels up to about v = 9 are thermally populated (~ 1% for v = 9). Calculations for the NaI molecule included transitions from the first 10 vibrational levels but the effect of rotational energy was ignored by restricting the calculations to the J = 0 levels.

D. Results and Discussion

1. HI Molecules.

Figure 2 shows the results computed from a fixed repulsive potential given in Ref. (4-c). This repulsive potential was obtained in Ref. (4-c) by fitting the observed HI continuous absorption spectrum using the δ - approximation with the ground state potential generated from the Dunham power series. It should be noted here that in our calculation the ground state potential was generated from the RKR procedure and only v = 0 and $j_{mp} = 4$ were used to calculate the

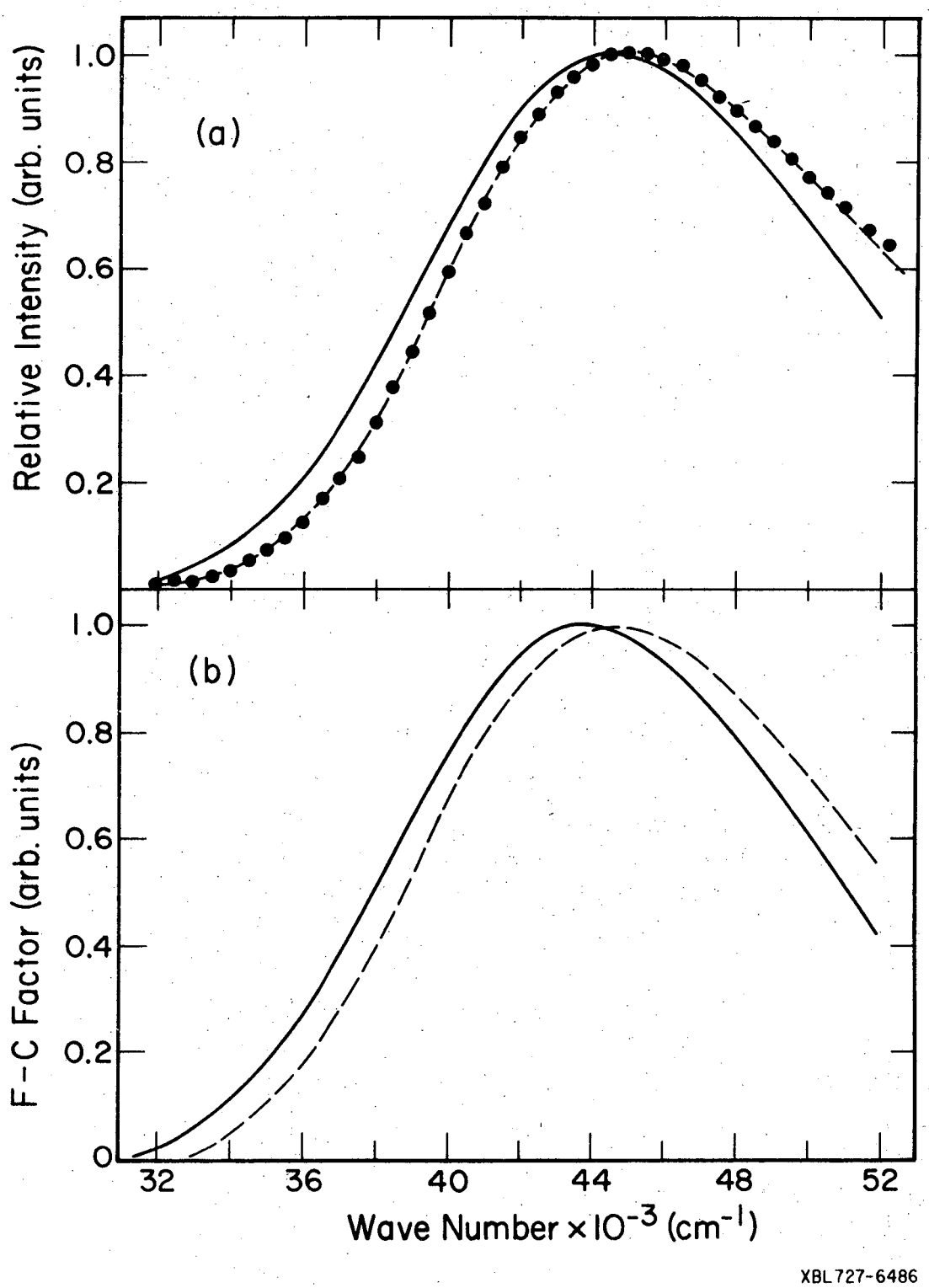

Fig. 2. (a) Absorption spectrum of HI molecule (● ● ●) and its transition probabilities obtained from the exact FC calculation (——) and the δ-approximation (- - -). (b) The corresponding FC factors calculated from the two methods.

theoretical intensity distribution. As shown in panel (a), the distribution of total relative intensity obtained from the δ - approximation gives a satisfactory agreement with the measured absorption spectrum (the solid circles, taken from Ref. 4-c); however, results obtained from the exact FC calculation for this same potential shift to small wavenumber, ν. This discrepancy is seen most clearly if one directly compares the FC factors, f, shown in panel (b). This illustrates that the exact calculations shift the entire curve toward small ν by an amount of $\sim$ 1000 cm^{-1} and also produce a faster decrease at large ν. In other words, the δ - approximation weights large ν too heavily. The origin of this distortion introduced by the δ - approximation may be seen by considering a very steep repulsive potential with the classical turning points at or near r_e, the equilibrium internuclear separation of bound state. In this case, f has its maximum at an energy corresponding to a transition originating from $v = 0$ in the lower state to an upper state energy, ε, such that the classical turning point for this upper state is only very slightly less than r_e. Now, as ε is increased beyond this optimum value, the successive loops of $|\ \varepsilon\ \rangle$, which have an opposite sign for every second loop, start to have a cancellation effect on the overlap integral. Therefore, exact evaluations of f yields a relatively large value for small ε but a faster drop off at large ε values. On the other hand, the δ - approximation provides f estimates which remain almost constant for a broad range in ε. For the HI molecules in the range studied, the absorption spectrum peaks at 45,000 cm^{-1} corresponding to $\varepsilon \sim$ 20,445 cm^{-1}

if the repulsive HI state dissociates into two ground state atoms, $H(^2S) + I(5p\ ^2P_{3/2})$. At this energy, the breadth of $|\ \varepsilon\ \rangle$ over which f is appreciable is smaller than the breadth which the δ - approximation would estimate simply by reflecting $|\ vj\ \rangle^2$ through the upper state potential because the cancellation due to the second loop in the continuum wavefunction seems to be important.

Although the rotational effect on the FC factor has been shown to be very important for both continuous[3] and band spectra[16] of the H_2 molecules, Ogilvie[4c] shows that it is minor for HI. This is largely due to the fact that for HI here only v = o is important. Results of the FC calculation with j = 0, 4, and 8 (about 80% of the HI molecules have $J \leqslant 8$) confirmed his indication: only a slight shift toward smaller ν for j = 8 and larger ν for J = 0 in comparison with the Jmp = 4. This insensitive j-dependence was also reported for the O_2 molecules.[17]

By means of the trial and error method, a best-fit repulsive potential was constructed to fit the HI absorption data reported in Ref. (4-c) and Ref. 18 by using exact evaluation of the FC factors. This potential, shown as the solid curve in Fig. 3, is about 1000 cm^{-1} higher than the one proposed by Ogilvie[4c] for HI using the δ --approximation. Ogilvie also reported an absorption spectrum for the DI molecules. Using the δ - approximation, he was unable to fit the DI absorption spectrum by the same potential employed to fit the HI absorption spectrum. This disconcerting aspect of Ogilvie's work was the original motivation for our interest in HI, as we felt that the δ - approximation employed by

Fig. 3. Potential energy diagram for HI molecules. The solid repulsive potential was constructed from the exact FC calculation and the dashed curve from the delta approximation; the ground state potential was generated from the RKR procedure. Also shown are (1) unnormalized ground vibrational wavefunctions of the ground HI and DI molecules, (2) continuum wavefunction for a selected vibrational energy of the solid repulsive potential, and (3) two asymptotic energy levels of H + I ($5p\ ^2P_{3/2}$) and H + I^* ($5p\ ^2P_{1/2}$). Notice that different energy scaling for the two potential curves is used.

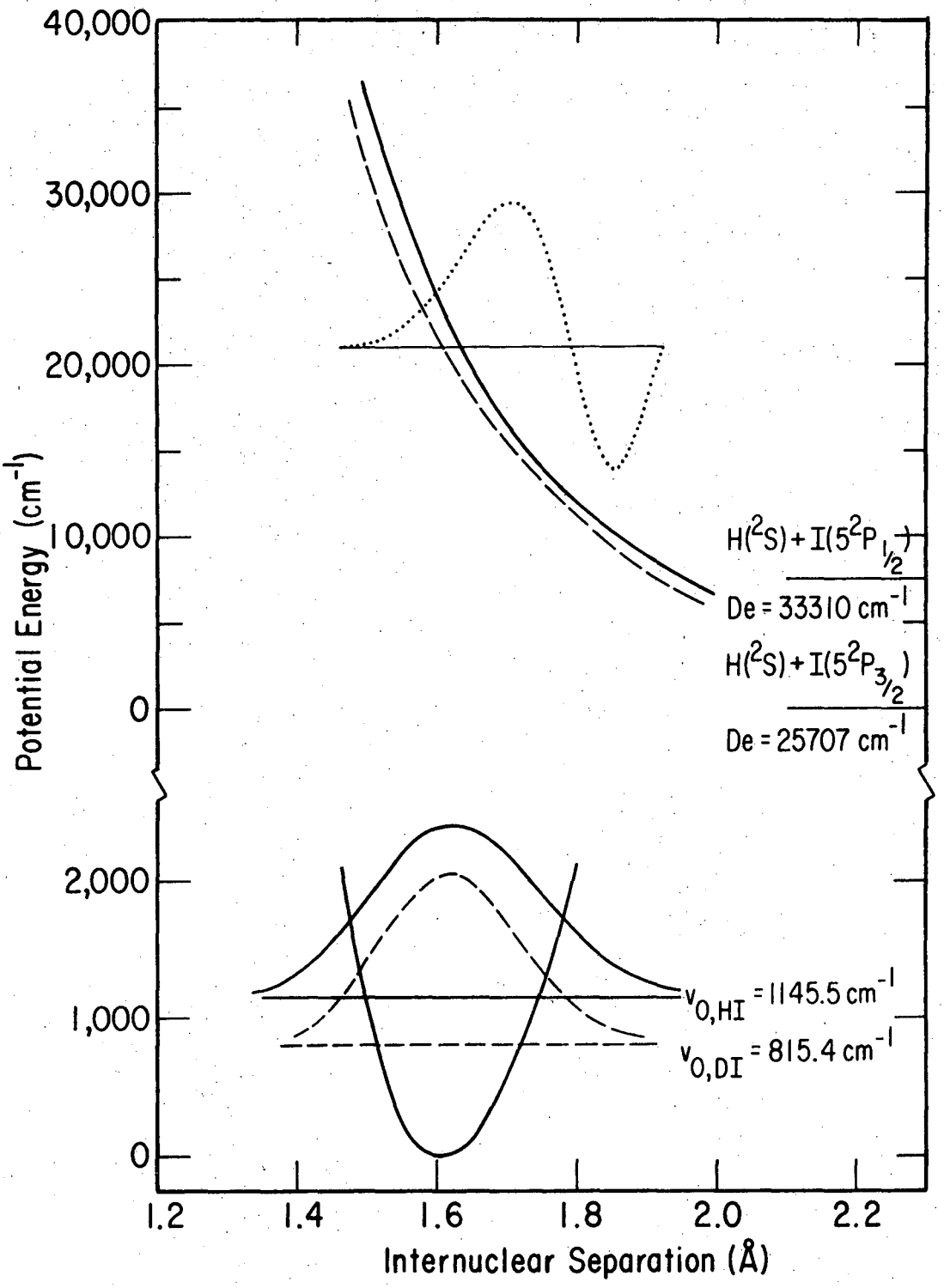
40,000
30,000
20,000
10,000
0
2,000
1,000
0
Potential Energy (cm⁻¹)
H(²S) + I(5²P1/2)
De = 33310 cm⁻¹
H(²S) + I(5²P3/2)
De = 25707 cm⁻¹
v0,HI = 1145.5 cm⁻¹
v0,DI = 815.4 cm⁻¹
1.2
1.4
1.6
1.8
2.0
2.2
Internuclear Separation (Å)
XBL727-6479

Fig. 3.

Ogilvie would provide a bad estimate of the FC factors because of the very steep nature of the repulsive HI potential. However, we found that the potential which best accounts for the HI spectrum using exact calculation of FC factors (i.e., the solid curve in Fig. 3) also fails to reporduce the reported[4c] DI absorption spectrum. Results are presented in Fig. 4; the solid curve shows the calculated intensity distribution for HI and the dashed curve for DI. The absorption spectra were taken from Ref. 4-c (●, ○) and Ref. 18 (▲). The comparable, calculated intensity for both HI and DI at $\nu \simeq 45000\text{-}52000$ cm^{-1} corresponding to $r \simeq 1.64 - 1.56$ Å appears to be closely related to the approximately equal amplitude of $|\, vj \,\rangle$ for these molecules in that region, as illustrated in Fig. 3. On the other hand, the fast drop of $|\, vj \,\rangle$ for DI around 1.8 Å shown in Fig. 3 produces the low intensity at smaller ν shown in Fig. 4. Although Ogilvie[4c] proposed several possibilities for his inability to fit the HI and DI absorption curves by a single potential, none of them seemed very probable to us. Mullikan[19] indicated in 1937 that three lowest excited states of the HI molecules might be involved in this transition process: these states are $^3\Pi_1$, $^1\Pi$ and $^3\Pi_{o+}$. The first two states dissociate into ground iodine $I(5p\ ^2P_{3/2})$ and the third one into excited iodine $I(5p\ ^2P_{1/2})$ with the hydrogen atoms in the ground state $H(^2S)$ for all three cases. Mullikan concluded that either (a) $^3\Pi_1 \leftarrow X\ ^1\Sigma^+$ and $^1\Pi \leftarrow X$ much exceed $^3\Pi_{o+} \leftarrow X$ or (b) $^3\Pi_1 \leftarrow X$ plus $^1\Pi \leftarrow X$ about equal $^3\Pi_{o+} \leftarrow X$ in total intensity, was more favorable than a third possibility that the transition mainly involves $^3\Pi_{o+} \leftarrow X$. In 1966,

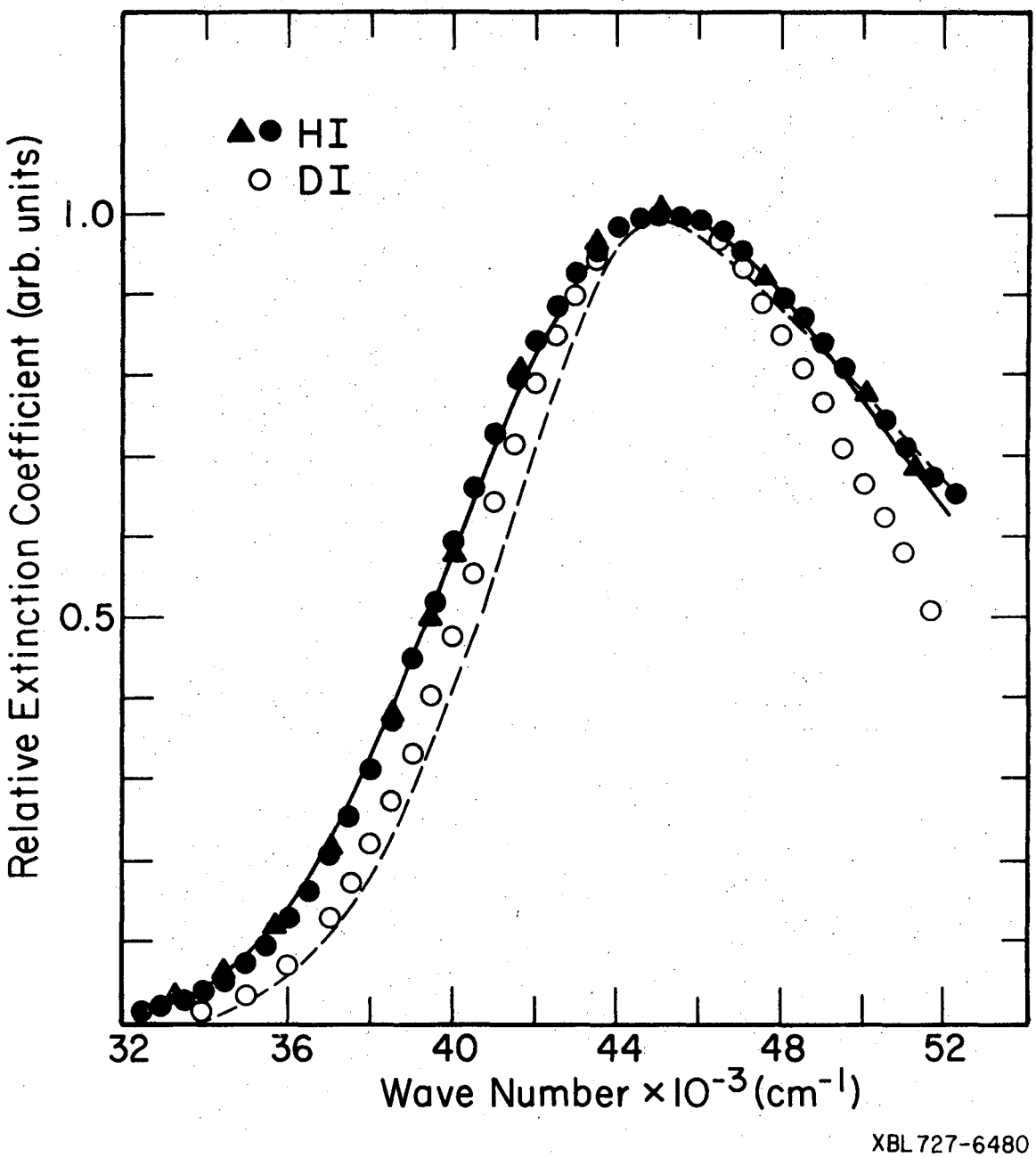

Fig. 4. Absorption spectra of HI and DI molecules. The solid curve shows the calculated intensity for HI and the dashed curve for DI, obtained from the solid repulsive curve shown in Fig. 3.

experimental evidence from Donovan and Husain[20] indicated that approximately one-fifth of the iodine atoms were formed in the excited state for 2180 Å absorption by HI. Cadman and Polanyi,[21] on the other hand, showed a 55 ± 25% yield of I^* ($^2P_{1/2}$) for the photolysis of HI at 2537 Å; this value is not in agreement with the later report by Compton and Martin.[22] They indicated that $I^*(^2P_{1/2})$ formation was only important in the proximity of absorption peak ($\leqslant$ 20%). Because of the large experimental uncertainty (10 to 25%) and the lack of detailed information through the entire spectrum concerned, no further analysis of the absorption spectrum of HI is attempted here.

Thus, the potential curve shown in Fig. 3 represents an "average potential" for the HI absorption in the 39,000-52,000 cm^{-1} range. Also, the inability shown in Fig. 4 to fit the HI and DI absorption with one repulsive potential is taken as further indication that the absorption is due to transitions to two or more repulsive potentials. Indeed, the remarks on the HI absorption spectrum which has been offered here illustrate the potentiality as well as the limitations of analysis of absorption spectrum as a means of gaining more insight into the repulsive excited states of diatomic molecules. Thus, we have shown that the δ - approximation in general distorts the derived molecular potential. Moreover, with the advent of modern, high-speed computers it is a relatively easy task to claculate exact FC overlap integrals and there seems little reason for the continued use of the δ - approximation. Furthermore, the results presented in Figs. 2-4 illustrate that a measured absorption spectrum will usually be

reasonably sensitive to the molecular potential so that one could expect to derive an accurate repulsive potential by fitting the measured spectrum. However, HI is typical of the problem which will be encountered in most molecules in that in general more than one repulsive electronic state of the molecule will be involved in the absorption. Thus, it will not be possible to unfold the data so as to arrive at the functional form of the potential unless the absorption spectrum is supplemented by other experimental measurements. These might include chemiluminescence or chemical laser determinations of the yield of atomic product states of the photodissociation. Additionally, the photodissociation recoil spectrum technique being pioneered by K. R. Wilson and his co-workers[23] as well as a few other laboratories should provide valuable information because their measurements of the angular distribution of the photodissociation products allow them to distinguish between parallel ($\Delta\Omega = 0$) and perpendicular ($\Delta\Omega = \pm 1$) transitions.

2. NaI Molecules.

The NaI repulsive potential was constructed, based on the measurement of fluorescent intensity of sodium D lines by Earl et. al.[15] in their quenching study. Both the exact FC principle and the δ - approximation were again employed in constructing the repulsive potential; results are shown in Fig. 5. Two repulsive potential curves previously, roughly estimated by Hanson[5] and Davidovits and Brodhead[4b] using the δ - approximation, denoted as H and D respectively, are also shown. The potential curve, B, generated from the δ - approximation shows a similar shape to that produced by the exact analysis but is quantitatively

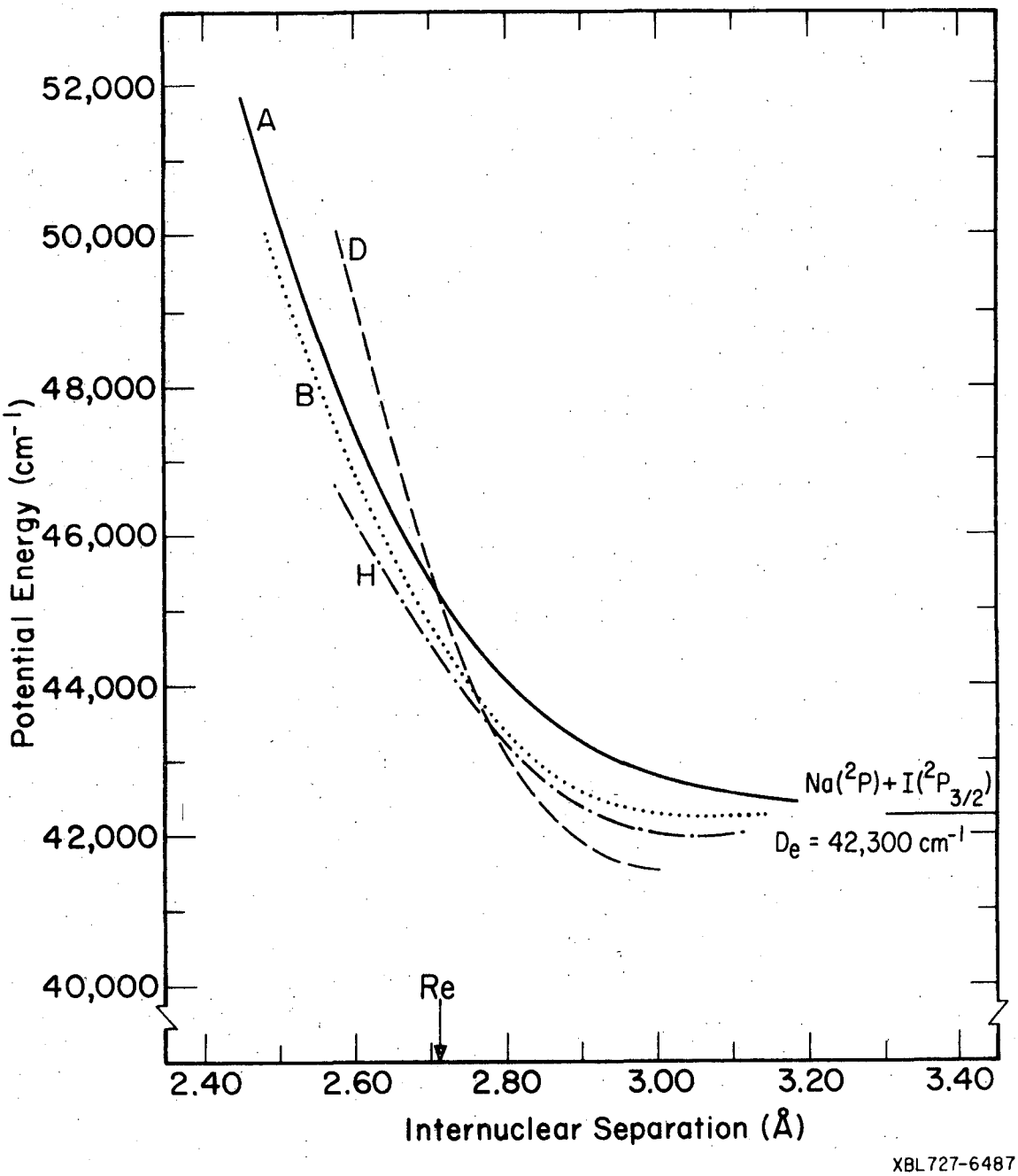

Fig. 5. Repulsive potential of NaI molecules, constructed from the exact FC principle (A) and the δ-approximation (B). Two previously reported potentials, H and D, are included for comparison (see the context).

different in a manner similar to that found for HI in the previous section.

The origin of the difference between curves A and B in Fig. 5 is more complicated for this case of NaI than for the HI case discussed in the preceeding section. This arises because more vibrational levels of the ground state NaI molecule are involved in the transition. The FC factors evaluated by the two methods for thethree lowest vibrational levels are compared in Fig. 6. For v = 0, the difference between the two methods is not as large as in the case of HI; this results from the fact that the overlap integrals for NaI in the v = 0 level essentially involve a smaller range of internuclear separations. However, the δ - approximation (the dashed curves) places too much weight on large ν transition for all vibrational levels, particularly for larger v values. This indicates that the δ - approximation is bad at smaller r values (corresponding to large ν). Again, the cancellation of successive loops of the oscillatory continuum wavefunction and the neglect of a proper energy normalization, discussed earlier in the HI section, accounts for this inaccuracy of the δ-approximation in the region corresponding to $r < r_e$.

Figures 7 and 8 show results obtained from the FC calculation. The repulsive potential was constrained to a dissociation limit of 42300 cm^{-1}.[14] Although a shallow minimum of theorder of ~ 0.2 e.v. was considered,[4b,5] its confirmation requires further experiment study. Moreover, as in the HI case, the actual transitions leading to $Na^*(3p\ ^2P) + I(5p\ ^2P_{3/2})$ are probably a sum of transitions to two

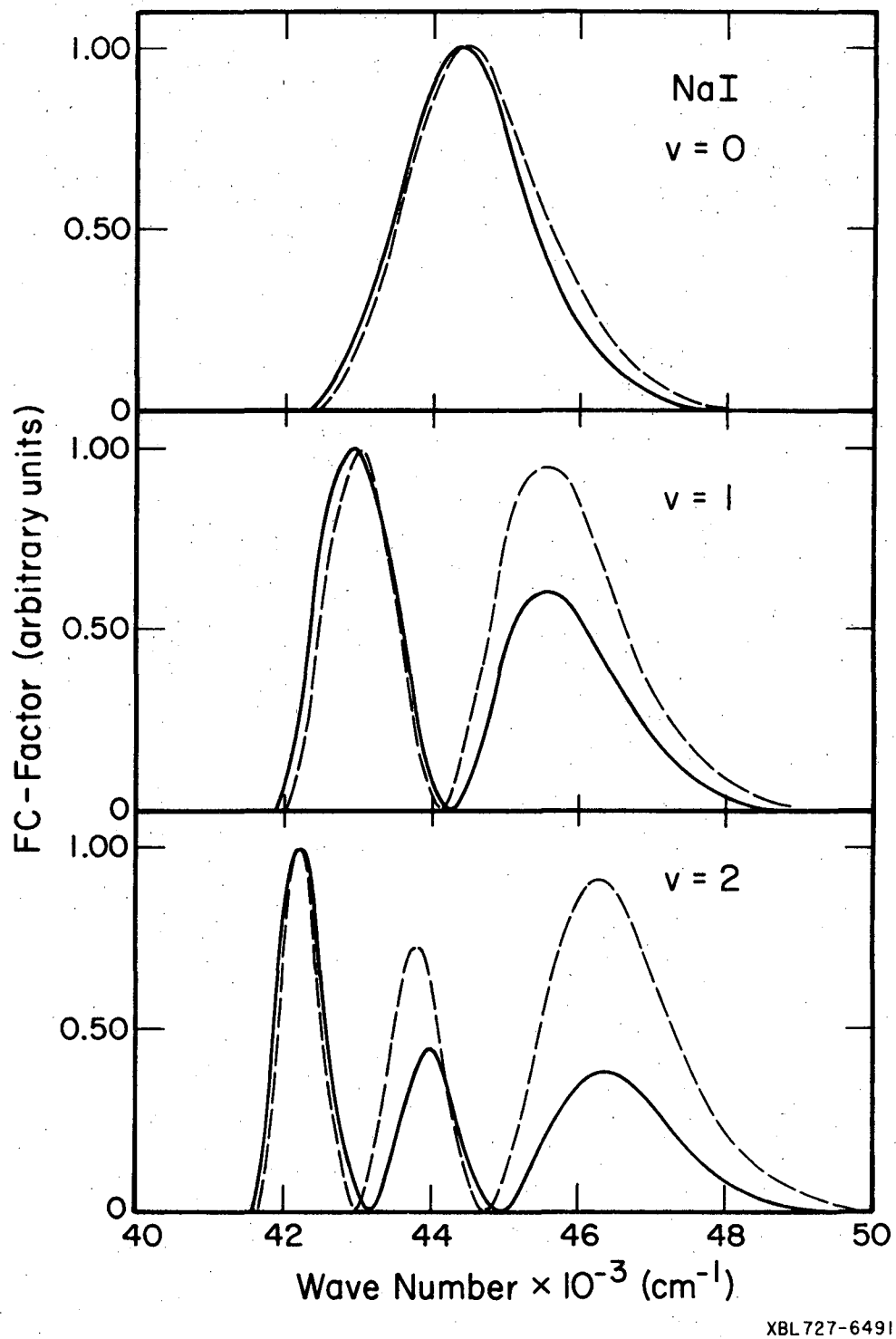

Fig. 6. FC factors of three lowest vibrational levels. The solid curves resulted from the exact FC calculation and the dashed curves, the δ-approximation.

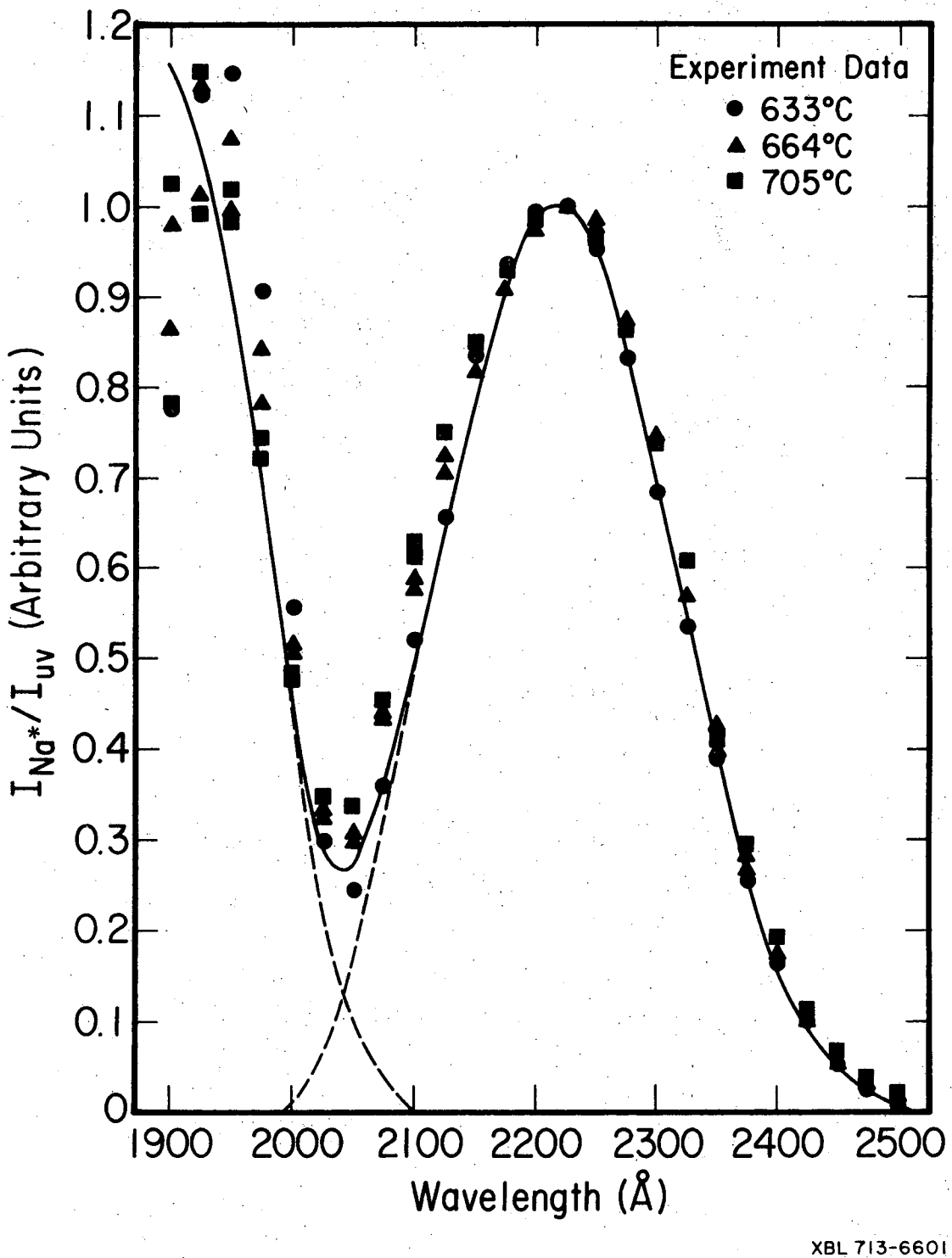

Fig. 7. The reduced fluorescent intensity distributions of Na D-lines. Data are given as solid symbols. The theoretical distributions calculated for T = 633°C are shown by solid curves but dashed lines at vicinity of the saddle. The complete curve at large wavelength corresponds to $Na^*(^2P) + I(^2P_{3/2})$.

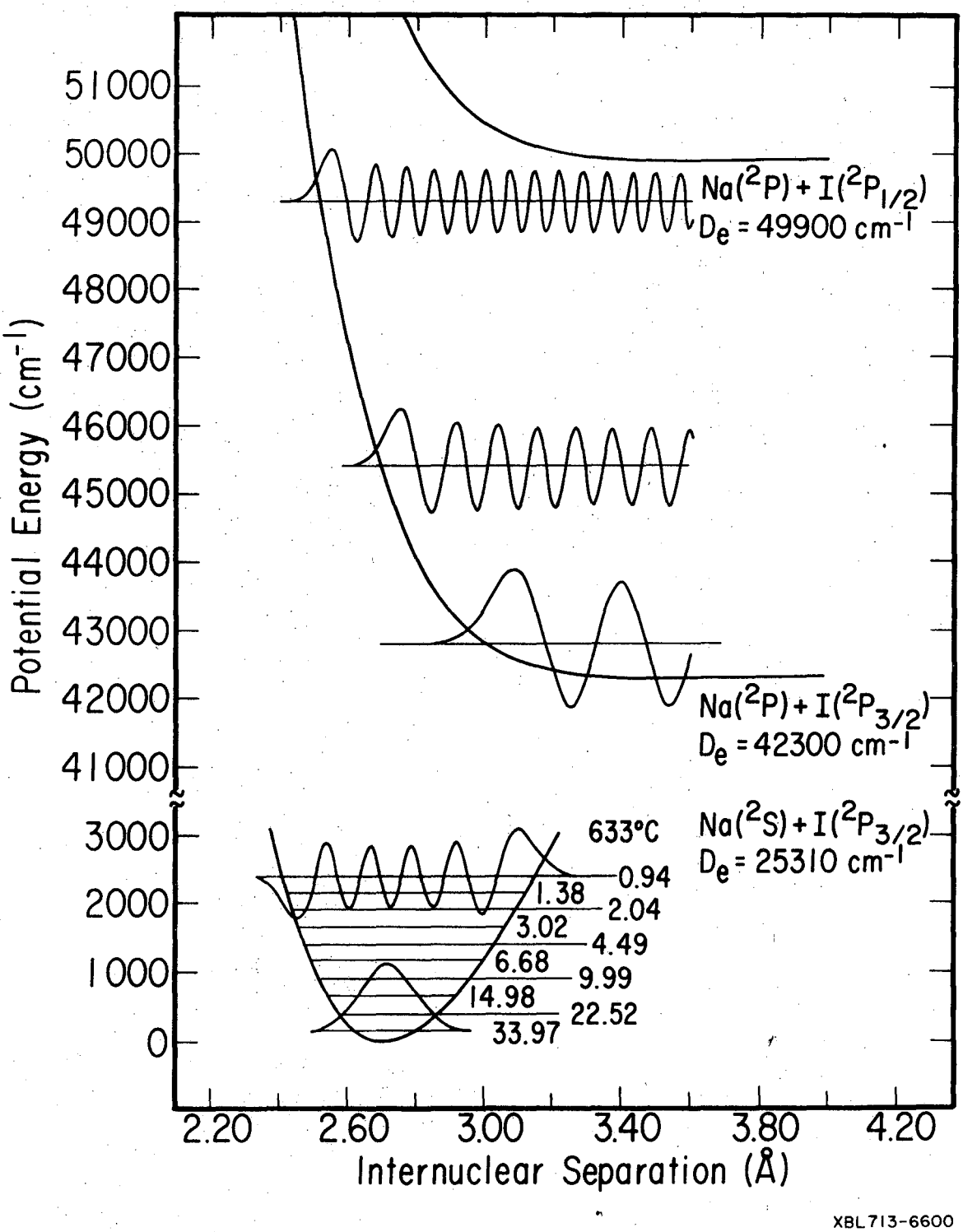

Fig. 8. NaI potential energy diagram. Thermal population of the first ten vibrational levels at T = 633°C and some selected, unnormalized wavefunctions are shown. Also shown is the dissociation limit of each state.

or more NaI excited electronic states. Consequently, the potential curve A shown in Fig. 5 is a potential for all those possible molecular states involved in the transitions.[24] Figure 7 only shows the comparison at T = 633°C; similarly good fits are also obtained for the data at other temperatures. Moreover, by raising this best found potential an amount corresponding to the energy separation of the two lowest atomic states of iodine $I(^2P_{3/2})$ and $I(^2P_{1/2})$ and assuming constant electronic moment matrix elements, curve A of Fig. 5 also fits the second peak (~ 1950 Å) shown in the reduced fluorescence spectrum of Fig. 7.

3. $\bar{r}$ - centroid analysis

The FC principle assumes that the variation of the matrix element of the electronic dipole moment with internuclear separation is small that it may be considered as a constant. The validity of this assumption varies from one molecule to the other;[25] however, it should be most satisfactory in the case where the vibrational wavefunctions concerned are confined to small ranges of r. This is especially true of heavy moleeuiles with strong force constants and low vibrational quantum numbers. Although it can be justified by directly calculating the dipole moment as a function of internuclear separation, the most widely used method in the analysis of the validity of the FC principle in interpreting molecular band spectra is the $\bar{r}$ - centroid analysis, introduced by Fraser[26] and Turner and Nicholls[27] in 1954. The $\bar{r}$ - centroid approximation states that

$$\langle v' \,|\mu_e(r)|\, v'' \rangle \simeq \mu_e(\bar{r}_{v',v''}) \langle v' \mid v'' \rangle \qquad (5)$$

where $\bar{r}_{v'v''}$ is defined as $\bar{r}_{v'v''} \equiv \langle v'|r|v'' \rangle / \langle v' \mid v'' \rangle$. This expression becomes exact when the transition moment is a linear function of $\bar{r}_{v'v''}$. The $\bar{r}$ - centroid analysis has apparently not been applied on the continuous spectrum yet. It is employed here to verify the applicability of the FC principle analysis presented earlier for both HI and NaI. To facilitate the numerical calculation, a new quantity,[28] y^n, is used

$$y^n \equiv \langle \varepsilon \, |r^n| \, vj \rangle / \bar{r}^n \langle \varepsilon \mid vj \rangle ; \quad n = 2, 3, \ldots \infty . \qquad (6)$$

When y^n is unity for all n's, the approximation implied in Eq. 5 becomes exact. Results of this calculation are shown in Fig. 9.

For the HI molecules, the deviation from unity for n = 2 is less than 1% and is about 10% for n = 10 throughout the entire region. This result is better than that shown by Drake and Nicholls[28] in their application of $\bar{r}$ - centroid on molecular hydride band spectra.

For NaI, results from v = 0 and v = 5 are shown in the figure; also included are the FC factors for each vibrational level. For n = 2, the result is much better than that for HI owing to the smaller range of internuclear separation involved. However, for v = 5, the deviation from unity at n = 10 becomes large (10 ~ 20%) when the FC factor is small. This arises simply because the $\bar{r}$ - centroid is appreciable only at or near the proximity of the overlap integral; in other words, the use of $\bar{r}$ - centroid loses its significance when the overlap integral is small. More detailed calculations for a series of diatomic oxides, nitrides, and halides of bound-bound

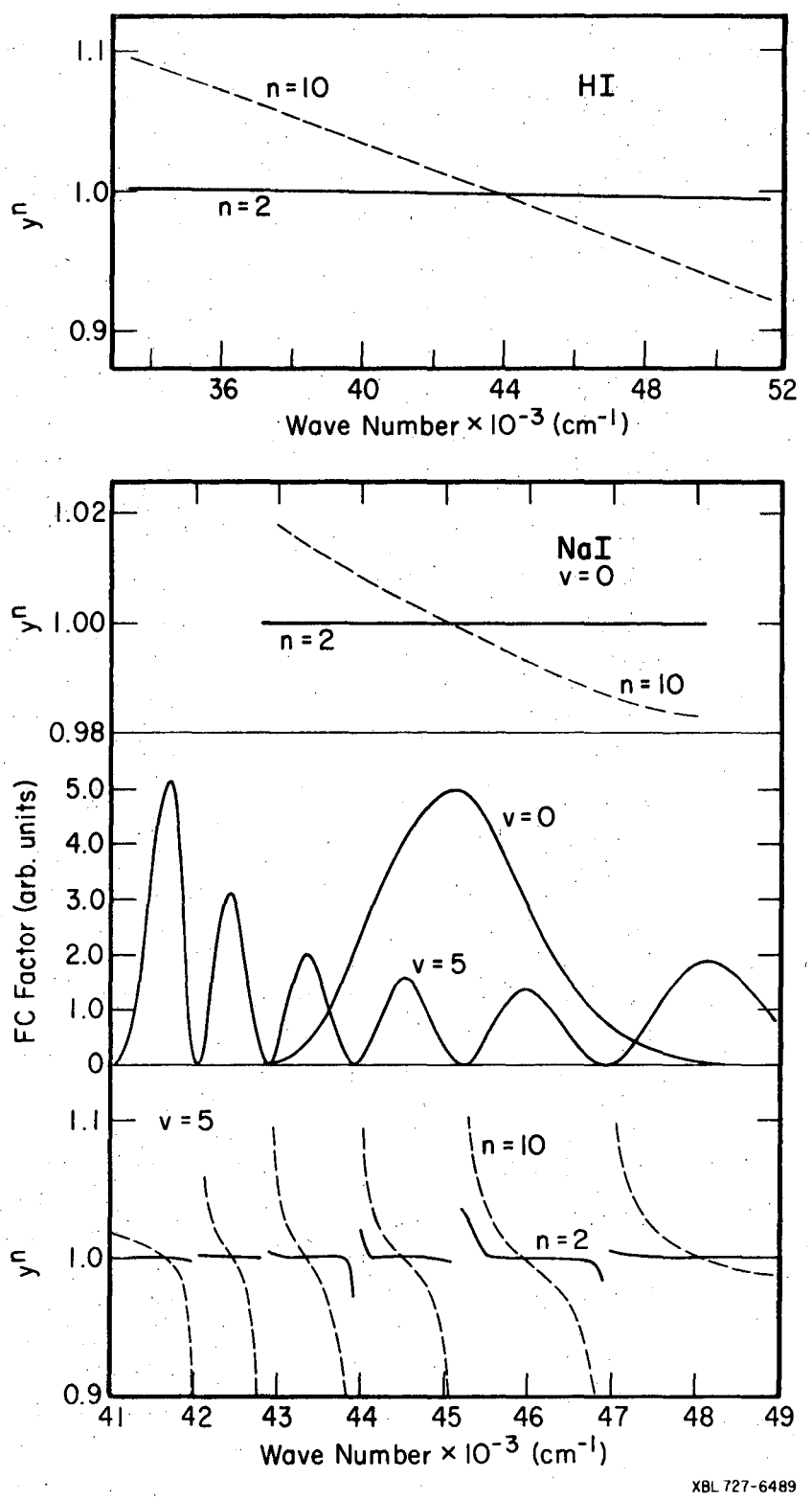

Fig. 9. $\bar{r}$ - centroid analysis. Results calculated for n=2 and 10 (see Eq. 6) for HI at v=0 and NaI at v=0 and 5. Also shown is the NaI FC factors at v=0 and 5.

transitions[28] illustrated the same trend at large values of n. For both HI and NaI molecules, this $\bar{r}$ - centroid analysis demonstrates that the FC principle is a good approximation in analyzing the continuous spectrum.

E. Summary

A comparison is made between the exact Franck-Condon principle and the δ-approximation in calculating the transition probabilities for photodissociation of both HI and NaI molecules. Results of this study indicate that the repulsive potentials extracted from the δ-approximation are about 1000 cm^{-1} lower than those obtained from the exact FC principle for both molecules. The origin of this discrepency is found that the δ-approximation weights too heavily at large wavenumber because it neglects (1) the energy dependence of continuum wavefunction for the repulsive state, and (2) the constructive and destructive effect of vibrational wavefunctions of the two electronic states involved. The first effect is most significant when the repulsive potential is very steep whereas the second effect is most pronounced when the repulsive potential is a slow function of internuclear separation. Auxilliary $\bar{r}$ - centroid calculations indicate that the matrix element of the electronic transition moment is only slightly dependent of the internuclear separation and thus, the error introduced in the FC principle is in the order of ~ 1-2%.

REFERENCES

1. G. Herzberg, Molecular Spectra and Molecular Structure. I. Spectra of Diatomic Molecules. (Van Nostrand, Princeton, 1950).
2. (a). A. S. Coolidge, H. M. James, and R. D. Present, J. Chem. Phys. 4, 193 (1936).

   (b). A. S. Coolidge, H. M. James, and E. L. Vernon, Phys. Rev. 54, 726 (1938).

   (c). H. M. James and A. S. Coolidge, Phys. Rev. 55, 184 (1939).
3. R. O. Doyle, J. Quant. Spect. Radiat. Transfer. 8, 1555 (1968).
4. (a). C. F. Goodeve and A. W. C. Taylor, Proc. Roy. Soc. (London) A154, 181 (1936).

   (b) P. Davidovits and D. C. Brodhead, J. Chem. Phys. 46, 2968 (1967).

   (c). J. F. Ogilvie, Tran. Far. Soc. 67, 2205 (1971).
5. H. G. Hanson, J. Chem. Phys. 23, 1391 (1955).
6. J. W. Cooley, Math. Computation. 15, 363 (1961).
7. (a) R. N. Zare and J. K. Cashion, UCRL-Rept. 10881. Lawrence Berkeley Laboratory, Berkeley, Calif. 1963; (b) R. N. Zare, UCRL-Rept. 10925, 1963.
8. M. A. Melkanoff, T. Sawada, and J. Raynal, Methods in Computational Physics. (Academic Press, N.Y. 1966), vol. 6, p 31.
9. (a) R. Rydberg, Ann. Physik. 73, 376 (1931).

   (b) O. Klein, Z. Physik, 76, 226 (1932).

   (c) A. L. G. Riess, Proc. Phys. Soc. (London). A59, 998 (1947).
10. R. M. Herman, R. H. Tipping, and S. Short, J. Chem. Phys. 53, 595 (1970).

11. E. S. Rittner, J. Chem. Phys. 19, 1030 (1951).

12. H. L. Kramer and D. R. Herschbach, J. Chem. Phys. 53, 2792 (1970).

13. A. Dalgarno, Adv. Phys. 11, 281 (1962).

14. L. Brewer and E. Brackett, Chem. Rev. 61, 425 (1961).

15. B. L. Earl, R. R. Herm, S. M. Lin, and C. A. Mims, J. Chem. Phys. 56, 867 (1972).

16. D. Villarejo, R. Stockbauer, and M. G. Inghram, J. Chem. Phys. 50, 1754 (1969); Chem. Phys. Letters 2, 11 (1968).

17. M. Bixon, B. Raz, and J. Gortner, Mol. Phys. 17, 593 (1969).

18. B. J. Huebert and R. M. Martin, J. Phys. Chem. 72, 3046 (1968).

19. R. S. Mullikan, Phys. Rev. 51, 310 (1937).

20. R. J. Donovan and D. Hurain, Trans. Far. Soc. 62, 1050 (1966).

21. P. Cadman and J. C. Polanyi, J. Phys. Chem. 72, 3715 (1968).

22. L. E. Compton and R. M. Martin, J. Phys. Chem. 73, 3474 (1969).

23. G. E. Busch, R. T. Mahoney, R.I. Morse, and K. R. Wilson, J. Chem. Phys. 51, 449 (1969); 51, 837 (1969).

24. (a). H. G. Hanson, J. Chem. Phys. 27, 491 (1957); 47, 4773 (1967)

(b). R. N. Zare and D. R. Herschbach, Proc. IEEE 51, 173 (1963); Lawrence Berkeley Laboratory Report UCRL-10438, Berkeley, Cal. 1963.

25. For an extensive review, see

(a). F. S. Ortenberg and E. T. Antropov, Sov. Phys. Usp 9, 717 (1967).

(b). R. W. Nicholls and A. L. Stewart, Atomic and Molecular Processes. chapt. 2. Allowed Transitions. (Academic Press Inc. N.Y. 1962).

26. P. A. Fraser, Can. J. Phys. 32, 515 (1954).

27. R. G. Turner and R. W. Nicholls, Can. J. Phys. 32, 475 (1954).

28. J. Drake and R. W. Nicholls, Chem. Phys. Letters. 3, 457 (1969).

Photodissociation of NaI Vapor and the Energy Dependence of the Quenching of Na* ($3p\ ^2P$) by Foreign Gases

BOYD L. EARL, RONALD R. HERM,* SHEN-MAW LIN, AND CHARLES A. MIMS
Inorganic Materials Research Division, Lawrence Berkeley Laboratory and Department of Chemistry, University of California, Berkeley, California 94720
(Received 16 August 1971)

Fluorescence of the Na* ($3p\ ^2P$) D lines is observed upon photodissociation of NaI vapor by 1900–2500 Å radiation obtained through a monochromator from a high current, low pressure H_2 arc continuum source; the properties of this source are briefly described. The D lines fluorescence efficiency exhibits a threshold at ~2500 Å, a relative maximum at ~2225 Å, and a relative minimum at ~2050 Å. An expression is derived for the distribution in laboratory speeds of an atom produced by photodissociation of a diatomic molecule at thermal equilibrium. This expression is then employed to calculate the distributions in speeds of the photodissociatively generated Na* and these computed Na* speed distributions are employed to analyze the observed attenuations of the D-lines fluorescence upon addition of foreign gases. In this manner, the dependences on relative collision velocity g of the cross sections Q_q for collisional quenching of Na* by CO_2, C_2H_4, CH_3CN, CF_3Cl, C_6H_6, SO_2, and I_2 have been determined. Over the range in g studied in this work (~1.0–2.5 km/sec), Q_q varies approximately as g^{-s}, with s in the range of 4–6, for all seven quenching gases. At a fixed value of g, Q_q varies as: $I_2 > SO_2 > C_6H_6 > CH_3CN > CF_3Cl > C_2H_4 > CO_2$. These results on the quenching cross sections are discussed in terms of the long-range forces between the reactants, including a possible long-range electron transfer curve crossing for the collision of Na* with I_2 or SO_2. These measured quenching cross sections are also compared with previous literature values; good agreement is found in most cases, although some discrepancies are noted.

In 1926, Terenin[1] observed that the optical dissociation of NaI vapor produced electronically excited Na* atoms. This was followed by the observation of the same phenomenon in the vapors of a number of diatomic halide molecules.[2] Soon after this discovery, it was realized that this phenomenon made possible measurements of the collisional quenching of electronic excitation of the atomic photodissociation product. When employed to measure collisional quenching cross sections, this method of photodissociative preparation of the electronically excited atom affords two advantages. Thus, it is possible to use as quenching gases species which would react with the ground state atom, but which are inert in the presence of the diatomic gas being photodissociated. It is this advantage of the method which made possible measurements[3,4] of thermally averaged cross sections for quenching of the $6^2P_{3/2}$ metastable state of Tl. Additionally, by varying the photodissociation wavelength, it is possible to vary the speed of the electronically excited atom produced. This has made possible measurements of the energy dependence of the cross sections for collisional quenching of the resonance radiation of sodium,[5–12] potassium,[13] and thallium[10,11,14–16] atoms.

Within the past decade, crossed molecular beam studies[17] of the reactions of ground state alkali atoms have supplemented the older diffusion flame data on alkali atom reaction kinetics and have provided a good deal of insight into the reaction dynamics of ground state alkali atoms. This has led to a renewed interest in the collisional quenching of excited metal atoms. For example, Refs. 4 and 11 draw analogies between their results on quenching collisions and molecular beam results on analogous reactions of ground state species. In our own laboratory, this has prompted a program to measure the cross sections for quenching of excited alkali atoms. This present paper reports initial results of this program on the quenching of $3p\ ^2P$ Na*, as well as a more detailed examination of this particular experimental technique for measuring the energy dependence of quenching cross sections.

EXPERIMENTAL CONDITIONS

The apparatus employed in this study was similar to that described in Ref. 9. Continuous radiation, of constant intensity, from a source described below was focused through a Heath Model EU-700 monochromator: $f/6.8$ at 2000 Å with a reciprocal dispersion of approximately 20 Å/mm at the exit slit. The ultraviolet radiation exciting from the monochromator was chopped at ~80 Hz and focused into a heated quartz cell containing the NaI vapor. Except where noted, the monochromator was operated with 2 mm slits. This provided radiation centered about the nominal wavelength setting with an approximately triangular distribution function characterized by a 47 Å FWHM bandspread, or an energy spread of ~950 cm^{-1} at 2250 Å; the experimental consequences of the monochromator bandwidth are discussed later and shown to be minor. Upon exiting from the sample cell, the ultraviolet radiation impinged upon an RCA 1P21 photomultiplier tube which had been sprayed with a coating of sodium salicylate. Since the fluorescence efficiency of sodium salicylate is reported[18] to be constant for the wavelength region studied here, the output signal from this phototube was proportional to the flux of incident ultraviolet photons.

The resulting sodium fluorescence was observed at a right angle to the ultraviolet flux through an interference filter; its intensity was measured by means of

Reprinted from:
THE JOURNAL OF CHEMICAL PHYSICS VOLUME 56, NUMBER 2 867–882 15 JANUARY 1972

an RCA 7265 photomultiplier and a PAR HR-8 amplifier locked in on the ~80 Hz oscillation imposed on the ultraviolet beam. A Baird Atomic B-11 interference filter, with a transmission bandwidth of ~15 Å FWHM, was used to isolate the 5896 and 5890 Å sodium *D* lines. Data presented in Ref. 12 indicate that the ratio of the fluorescence intensities of these two lines varies from ~2/3 to ~1 for NaI excitation in the 2100–2500 Å region. Insofar as only the total intensity of both fluorescence lines is measured in this work, the reported quenching cross sections are really an average (weighted by the relative population densities of the two levels) of the cross sections for quenching of the Na* $3p\,^2P_{1/2}$ and $3p\,^2P_{3/2}$ fine structure components. However, the cross sections for quenching of these two components should be practically the same in view of the very small energy separation of the levels and the complexity of the quenching species studied here. This expectation is further supported by the relatively large cross sections reported[12] for interconversion of these fine structure components by a collision partner as simple as argon.

The vapor cell was constructed from 30 mm quartz tubing, ~16.5 cm in height. Four flat windows, two of suprasil for the ultraviolet beam and two of quartz, were equally spaced at 90° about the tube circumference, ~4 cm down from the top. Each window extended out ~1.25 cm from the tube wall, so that the optical path of the ultraviolet through the cell was ~5.5 cm. At its top, the 30 mm quartz tube was connected to the vacuum line through a 3-mm-i.d. opening which could be sealed by a magnetically operated ground quartz rod. The 30 mm tube was joined at the bottom to a 10 cm length of 10 mm quartz tubing which was charged with reagent grade NaI. This entire assembly was placed in a wire wound oven which contained viewing ports coinciding with the windows in the cell. In order to prevent radiative cooling of these windows, they were further surrounded by additional heating coils. Two thermocouples were placed on the outside wall of the vapor cell, one just below the level of the windows and the other at the level of the charge of NaI salt. In operation, the temperature of the cell at the level of the windows was typically maintained 20–30°C hotter than that of the NaI charge, permitting independent variation of the temperature and pressure of the NaI vapor. The NaI vapor temperatures quoted in this paper refer to the temperature at the cell windows.

In the measurements of the collisional quenching of Na*, the NaI in the cell was maintained at the temperature of the experiment for a few hours, with periodic exposures to the vacuum line. Following this degassing procedure, the foreign quenching gas was admitted to the cell by means of the ground quartz seal. The pressure of the quenching gas admitted was measured by means of a Texas Instruments spiral quartz manometer situated on the external gas line. Because the mean free path within the gas at the pressures of quenching gas employed here was much smaller than the diameter of the interconnecting tubing, the pressure of the quenching gas measured at room temperature on the external gas line was equated with the pressure of quenching gas inside the cell (Ref. 4 discusses this thermal transpiration correction).

All chemicals employed as quenching gases were purchased commercially (reagent grade where available) and used without further purification. In so far as all of these gases exhibited relatively large quenching cross sections, the effects of small impurities should be negligible. It was also necessary to insure that the gases studied as quenching agents neither decomposed nor reacted with the NaI in the high temperature cell. Three experimental checks were employed to attempt to insure these conditions. As a first check, the behavior of the sodium fluorescence intensity upon admission of the foreign gas was examined. This resulted in the rejection of quite a few gases as possible quenching agents. Thus, the Na* fluorescence was virtually extinguished upon admission of CCl_4 gas and failed to reappear upon evacuation of the cell. Similarily, BF_3 and NO_2 were rejected because admission of these gases to the cell produced a rapid drop in the Na* fluorescence followed by a slower rise, suggestive of a slow chemical decomposition of these species. Admission of SF_6 to the cell at very low pressures (~0.1 torr) resulted in very large and non-reproducible attenuations of the Na* fluorescence. Trifluoromethane failed to quench the Na* fluorescence, even at pressures as high as 50 torr. Indeed, this gas had the opposite effect of enhancing the Na* fluorescence by 20%–30%, although the enhancement deteriorated with time. Related enhancement effects have been reported for thallium fluorescence[2] by NH_3 and sodium fluorescence[9] by H_2 at low pressures. As a second check, the constancy of the pressure of quenching gas was monitored while it was in the cell. This led to the rejection of propene, butene-1, butene-2, and toluene as possible quenching agents for study because, upon admission of any of these gases to the hot cell, the pressure measured on the external gas line increased slowly, suggesting decomposition of the gas admitted into smaller molecular weight products.

The seven gases employed as quenching agents in this study (C_2H_4, CH_3CN, CF_2Cl, C_6H_6, SO_2, I_2, and CO_2) satisfied both of these checks. As a final check, samples of each of the first five gases listed were collected from the hot vapor cell after actual quenching experiments. The mass spectral patterns of these gas samples were identical (to within experimental accuracy) to those of samples of the same gases taken prior to exposure to the hot vapor cell. The quenching of Na* fluoresence by CF_4, CH_4, and C_2H_6 was also examined briefly. These gases appeared to be stable

in the hot NaI cell, but proved to have very small quenching cross sections (estimated as less than ~ 5 Å^2).

Another effect which could invalidate the measured quenching cross sections arises when the foreign gas admitted to the cell absorbs a fraction of the ultraviolet being used to photodissociate the NaI. In such a case, the attenuation of the steady-state Na* fluorescence is due to a combination of the collisional quenching of the Na* and of absorption of the ultraviolet by the foreign gas. Of the seven quenching gases employed in this study, SO_2 and C_6H_6 absorbed[19] over a region of the NaI absorption continuum of interest. The ultraviolet absorptions by these gases were measured directly during the quenching experiments, and the quenching cross sections reported for SO_2 and C_6H_6 have been corrected for this effect. Another gas, CS_2, was studied briefly, but proved to absorb too strongly to permit quenching studies.

The Hydrogen Arc Ultraviolet Continuum Source

Initially, a high pressure Xe–Hg arc was employed as the source of the continuum ultraviolet radiation. However, this source was abandoned in favor of a low pressure H_2 arc patterned after a description due to Finkelstein[20] because the high output of visible radiation from the Xe–Hg arc proved troublesome. A brief description of this H_2 arc is given here because some initial difficulty was encountered in obtaining reliable operation. These remarks are intended to complement Finkelstein's[20] description. Figure 1 presents a schematic diagram of the electrodes inside the water-cooled brass lamp housing together with the electronics necessary for dc operation. In striking the arc, the cathode is resistance heated and the starting electrode is connected to a tesla coil. A voltage of about 260 V between anode and cathode is required to strike the arc with 6 torr of H_2. The lamp has been operated with both dc and rectified ac; operation in the dc mode enhances stability. The arc provides a usable continuum from ~ 1900 Å (the shortest wavelength examined) to above 3000 Å. Indeed, it provides an ultraviolet intensity through the monochromator and into the NaI cell which exceeds that provided by a Hanovia 1 kW high pressure Xe arc over the full 2000–3000 Å range and by a Hanovia 1 kW high pressure Xe–Hg arc below 2275 Å.

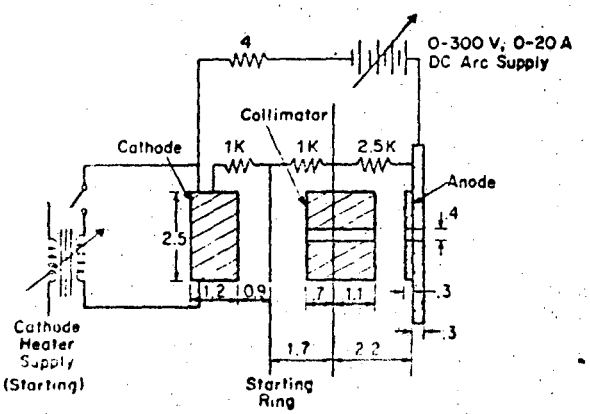

FIG. 1. Schematic sectional view (from the side) of the H_2 arc electrode arrangement, and a wiring diagram for dc operation. All distances are given in centimeters and resistances in ohms. The starting electrode is a ring of tantalum wire. The collimator is fabricated of molybdenum with a water-cooled copper sleeve and a large molybdenum disk to force the discharge to pass through the collimating orifice. The anode consists of a 2.5-cm-diam molybdenum disk mounted on a larger diameter (~ 5 cm) water-cooled copper disk. A 0.4 cm×0.65 cm orifice is cut through the collimator and anode.

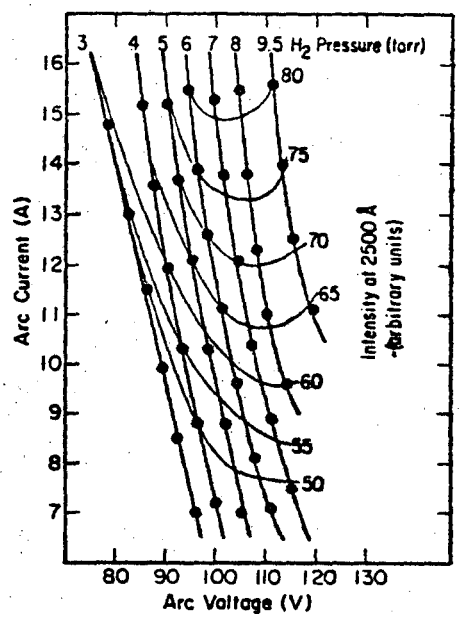

FIG. 2. The heavy solid curves (and dark circle data points) show the current through the arc as a function of dc voltage between the cathode and anode for various pressures of H_2 gas flowing through the arc housing. The lighter solid curves show contours of constant output intensity (measured in arbitrary units) at 2500 Å.

The nickel screen substrate cathode described in Ref. 20 is reinforced with a strip of tantalum foil down the middle, coated with a lacquer of barium–strontium carbonate, and folded into an accordian shape. Initially, the arc was difficult to strike and the cathodes exhibited short lifetimes until it was realized that the method of preparation and activation of the cathode surface is critical. By depositing a barium–strontium oxide solid solution onto the nickel screen substrate according to the directions given in Ref. 21, cathodes were subsequently obtained which exhibit acceptable lifetimes (40–50 h) and render the arc easy to strike and stable once struck.

Figure 2 shows the voltage–current–pressure–intensity relationship of the arc. The data are limited to arc voltages less than ~ 120 V because the arc is un-

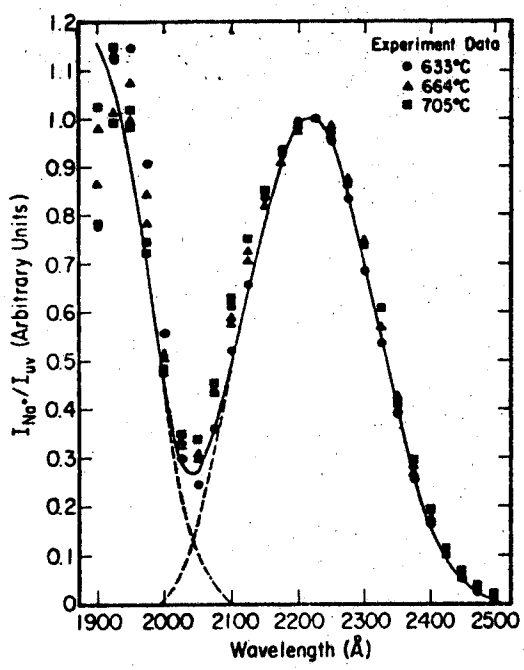

FIG. 3. The sodium *D* lines reduced fluorescence (i.e., the ratio of the total number of *D*-lines photons detected per second to the number of ultraviolet photons per second incident on the NaI vapor) plotted, in arbitrary units, versus the nominal wavelength of the ultraviolet. Data points are given as solid symbols. The temperature at the bottom part of the NaI cell, where the solid NaI resided, was 530, 565, and 603°C respectively for the data taken with vapor temperatures, at the cell window, of 633, 664, and 705°C. The bandwidths of the ultraviolet radiation were 24 Å (FWHM) for the 633°C vapor temperature experiment and 36 Å (FWHM) for the 664 and 705°C experiments. The uncertainty in the reduced fluorescence increases rapidly as the wavelength is lowered below 2000 Å. The dashed lines show theoretical *D*-lines reduced fluorescence curves calculated for an NaI temperature of 633°C for transitions to the two upper repulsive potential curves shown in Fig. 4; the solid curve is the sum of the two dashed curves. All three sets of data points and the theoretical curve were normalized to unity at their long wavelength relative maximum.

stable at higher voltages. Data are not given for arc currents higher than ~16 A because of limitation of the dc power supply used. Typical operating conditions in these experiments were in the 12–15 A, 6–8 torr of H_2 range.

PHOTODISSOCIATION OF NaI

The *D*-Lines Fluorescence Efficiency

Figure 3 shows the observed dependence of the reduced fluorescence efficiency $R(\lambda_0)$ (defined as the ratio of the total number of *D*-lines photons detected per second to the number of ultraviolet photons per second incident on the NaI vapor) on the nominal wavelength λ_0 of the ultraviolet impinging on the NaI vapor. In collecting this data, a temperature difference of ~100°C was maintained between the lower part of the NaI cell, where the solid NaI sample resided, and the upper part of the cell where the NaI vapor was photodissociated. This had the effect of rendering the temperature of the NaI vapor being photodissociated somewhat uncertain; for purposes of calculation, the temperature of the vapor was taken as the temperature at the windows of the cell. Since the vapor pressure of the NaI was governed by the lower temperature, however, the total absorption cross sections for NaI vapor quoted in Ref. 22 indicate that this procedure insured that the ultraviolet radiation was negligibly absorbed upon traversing the cell. It is probably worth emphasizing again that this temperature differential within the cell was maintained at ~20–30°C in measurements of quenching cross sections, thereby reducing the uncertainties in the quoted gas temperatures in these experiments. Figure 3 indicates that the reduced efficiency curves are similar for all three temperatures studied, although extending to somewhat longer wavelengths at higher temperatures. The second region of fluorescence excitation by radiation below 2000 Å has not apparently been previously reported.[9,22]

In agreement with previous workers,[1,9,11] the fluorescence peak at longer wavelengths shown in Fig. 3 is assigned to a transition of NaI from its ground state potential curve to the repulsive part of an excited state curve which dissociates into an excited Na atom (Na*) and a ground state iodine atom, i.e.,

$$\mathrm{NaI}(X\,^1\Sigma^+) \xrightarrow{\sim 2000\text{–}\sim 2500\ \text{Å}} \mathrm{Na}^*(3p\,^2P) + I(^2P_{3/2}). \quad (1)$$

A recent study[23] of the Doppler widths of the *D* lines suggested that the photodissociation of NaI vapor at wavelengths longer than ~2100 Å might not proceed exclusively by excitation of NaI to a repulsive state which dissociated into Na* and I within one vibrational period. However, the more recent study by Brus[11] of the Na* fluorescence lifetime indicated that the fluorescence is indeed a consequence of the direct photodissociative process depicted in Eq. (1).

The origin of the second, shorter wavelength fluorescence region shown in Fig. 3 is uncertain. It might be due to either or both of the following direct photodissociative processes:

$$\mathrm{NaI}(X\,^1\Sigma^+) \xrightarrow{?\text{–}2100\ \text{Å}} \mathrm{Na}^*(3p\,^2P) + I^*(^2P_{1/2}), \quad (2a)$$

or

$$\mathrm{NaI}(X\,^1\Sigma^+) \xrightarrow{?\text{–}2100\ \text{Å}} \mathrm{Na}^*(4s\,^2S) + I(^2P_{3/2}). \quad (2b)$$

Process (2a) would require a threshold energy shift relative to that of Eq. (1) of 7600 cm^{-1}; process (2b) would entail a corresponding shift of 8800 cm^{-1}. Indeed, this illustrates that a major obstacle to the extension of this NaI photodissociation technique to the study of quenching of more highly excited Na* species

arises because the density of NaI excited states correlating to different product atomic states increases rapidly with increasing excitation energy.

If the NaI vapor in vibrational level v and the zeroth rotational level is photodissociated by ultraviolet of frequency ν_0, then the kinetic energy E_v and speed u_v of recoil of Na* relative to the center-of-mass (c.m.) of NaI are given by conservation of energy and linear momentum in terms of m_{Na}, m_I, and m_{NaI}, the masses of Na, I, and NaI, by

$$m_{Na}u_v^2/2 = E_v = (m_I/m_{NaI})\epsilon,$$
$$\epsilon = h\nu_0 + \hbar\omega(v+\tfrac{1}{2}) - D_e - E^*. \qquad (3)$$

In this equation, ω refers to the circular vibrational frequency of ground state NaI, D_e to its dissociation energy[24] (25 310 cm^{-1}), and E^* to the Na* ($3p\,^2P$) excitation energy (17 000 cm^{-1}). Since, however, there exist thermal distributions in the NaI vibrational and rotational energies at a temperature T, the thermally averaged c.m. recoil energy and speed of Na* may be taken as

$$m_{Na}u_T^2/2 = E_T = E_{v=0} + (m_I/m_{NaI})(2kT). \qquad (4)$$

Finally, the final laboratory (LAB) Na* velocity is obtained from the vector sum of the Na* c.m. recoil velocity and the velocity of the original NaI molecule. Upon averaging the vector sums of the c.m. Na* recoil velocity given in Eq. (4) and the randomly orientated most probable NaI thermal speed, $\bar{v}_{NaI} = (2kT/m_{NaI})^{1/2}$, the characteristic Na* LAB speed is obtained[11] as:

$$V_T = u_T + \bar{v}_{NaI}^2/3u_T,\ u_T > \bar{v}_{NaI};$$
$$V_T = \bar{v}_{NaI} + u_T^2/3\bar{v}_{NaI},\ u_T < \bar{v}_{NaI}. \qquad (5)$$

In previous measurements of quenching cross sections by this photodissociative technique, the data has usually been analyzed[9] in terms of this characteristic LAB Na* speed. In order to proceed further and take into account the distribution of Na* LAB speeds, it is necessary to first compound the thermal distributions in translational and rotational motions of the NaI in order to calculate the probability density function for LAB Na* speeds, $P_{v,T,\nu_0}(V)$, produced by photodissociation of NaI in a particular vibrational level v by ultraviolet of frequency ν_0 and infinitesimal bandwidth δ_ν. The full probability density function of Na* speeds may then be calculated by summing the contributions of each vibrational level as

$$P_{T,\nu_0}(V) = \sum_{v=0}^{\infty} \rho_T(v) F_{T,\nu_0}(v) P_{v,T,\nu_0}(V). \qquad (6)$$

The first term, $\rho_T(v)$, is simply the thermal probability distribution function for NaI vibrational levels, readily calculated and shown in Fig. 4 for $T = 633$°C. The second factor is the relative probability of dissociation of an NaI molecule in vibrational level v by an ultraviolet photon of frequency ν_0, normalized such that

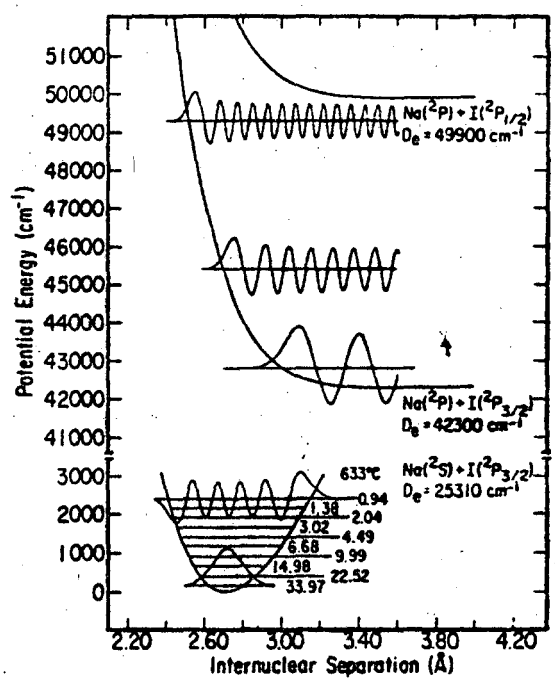

FIG. 4. The repulsive potential curves for the two electronically excited states of NaI dissociating into Na*($3p$) + I and Na*($3p$) + I* respectively and the NaI ground state potential curve which were used to fit the D-lines reduced fluorescence data of Fig. 3. Also shown are (1) the relative thermal populations at 633°C of the first ten vibrational levels of NaI, (2) unnormalized vibrational wavefunctions for the $v=0$ and $v=9$ levels of ground state NaI, and (3) three examples of continuum vibrational functions for the lower excited state of NaI. Note the break in the ordinate scale.

$$\sum_{v=0}^{\infty} \rho_T(v) F_{T,\nu_0}(v) = 1. \qquad (7)$$

In order to assess these $F_{T,\nu_0}(v)$ factors, it was necessary to reproduce the experimental reduced fluorescence curve shown in Fig. 3 by theoretical calculations. This was approached by recognizing that the steady-state rate of fluorescence of D-lines photons (I_D) was simply equal to the rate of excitation of NaI molecules, since Brus[11] has observed that NaI does not itself quench the Na* fluorescence. In terms of an unknown apparatus constant γ (comprised of photon detector efficiencies, efficiency of light collection, etc.), this is given by[23]

$$I_D = \gamma(8\pi^3/3h^2)\,|\mu|_{v,\nu_0}^2[\mathrm{NaI}]I_{\nu_0}/c, \qquad (8)$$

where [NaI] is the number density of NaI vapor, I_{ν_0} is the ultraviolet flux per frequency interval so that I_{ν_0}/c is the corresponding ultraviolet energy density, and $|\mu|_{v,\nu_0}$ is the electronic dipole matrix element between the ground state of NaI in vibrational level v and an upper electronic state dissociating into Na*

and I with an unbounded nuclear wavefunction corresponding to an asymptotic radial kinetic energy of ϵ given by Eq. (3). The actual experimental quantity of interest is the reduced fluorescence $R_v(\nu_0)=I_D/P_{\nu_0}$ where P_{ν_0} is the absolute number of incident ultraviolet photons/sec, given in terms of the cross sectional area A_{ν_0} of the ultraviolet flux by $P_{\nu_0}=I_{\nu_0}\delta_\nu A_{\nu_0}/h\nu_0$. If the Franck–Condon principle is assumed[26] so that $|\mu|_{v,\nu_0}$ becomes a product of a constant electronic matrix element μ_e times an overlap integral $f_{v,\epsilon}$ between the nuclear wavefunctions in the ground and excited states satisfying the radial Schrödinger equation, the reduced fluorescence efficiency becomes

$$R_v(\nu_0)=\left[\frac{8\pi^3}{3hc}\frac{\gamma[\mathrm{NaI}]\,|\mu_e|^2}{\delta_\nu A_{\nu_0}}\right]\frac{\nu_0 f_{v,\epsilon}^2}{\epsilon^{1/2}}, \qquad (9)$$

where the continuum nuclear wavefunctions are normalized asymptotically to sine functions of unit amplitude. Recognizing that the term in brackets in Eq. (9) is not a function of ν_0, $R_v(\nu_0)$ is given to within a constant factor by $\nu_0 f_{v,\epsilon}^2/\epsilon^{1/2}$. Furthermore, the $F_{T,\nu_0}(v)$ factors of Eq. (6) are proportional to this same variable, with a proportionality constant evaluated by means of Eq. (7). Finally, the theoretical calculations may be directly compared with experiment by summing over thermally distributed vibrational levels and integrating over the known bandpass function $M(\lambda, \lambda_0)$ of the monochromator as

$$R_T(\lambda_0)=c\sum_{v=0}^{\infty}\rho_T(v)\int_0^{\infty}M(\lambda,\lambda_0)R_v\left(\frac{c}{\lambda}\right)\left(\frac{d\lambda}{\lambda^2}\right). \qquad (10)$$

In order to calculate the reduced fluorescence curve shown in Fig. 3 by means of Eq. (10), the $X\,^1\Sigma^+$ ground state of NaI was assumed to be described in the important region of r near its minimum by an ionic potential model,

$$V(r)=\beta\left[Ae^{-r/\rho}-\frac{e^2}{r}-\frac{e^2(\alpha_+ +\alpha_-)}{2r^4}-\frac{C_6}{r^6}-\frac{2e^2\alpha_+\alpha_-}{r^7}\right]. \qquad (11)$$

The polarizabilities of Na^+ and I^- were taken[27] as $\alpha_+=0.15$ Å^3 and $\alpha_-=7.0$ Å^3 respectively and the dispersion force constant, C_6, was calculated from the Slater–Kirkwood approximation.[28] The repulsion constants, A and ρ, were evaluated by demanding that $dV/dr=0$ at $r=r_e$ and fitting $(d^2V/dr^2)_{r=r_e}$ with the experimental force constant (data taken from Ref. 24). Maltz[29] has shown that this procedure provides a potential function which correctly accounts for the dipole moments and dipole derivatives of a number of alkali halides. Finally, the scaling factor β was adjusted to 1.022 in order to obtain the correct dissociation energy for separation into Na^+ and I^-. Figure 4 shows a plot of the ground state potential function for NaI which was arrived at by fitting the expression given by Eq. (11) in the vicinity of the minimum, where all of the vibrational levels of interest here were determined, to a function which dissociated asymptotically into neutral Na+I.

The potential curve for the upper electronic state of NaI producing fluorescence for ultraviolet wavelengths from ~2000 Å to ~2500 Å was constrained to asymptotically approach a level 42 300 cm^{-1} above the minimum of the ground state potential curve. Subject to this constraint, upper state potential curves were chosen by trial and error. The normalized bound ground state vibrational wavefunctions and continuous upper state functions (normalized to unit asymptotic amplitude) were evaluated by numerical integration of the radial Schrödinger equations and the corresponding Franck–Condon overlap integrals were evaluated numerically. Following this, reduced fluorescence curves were computed according to Eq. (10) and normalized to the experimental data shown in Fig. 3. Figure 3 shows the comparison at one temperature for the best agreement which was obtained, corresponding to the upper state potential curve shown in Fig. 4; similarly good fits were obtained for the data at other temperatures shown in Fig. 3. For purposes of illustration, it was assumed that the shorter ultraviolet wavelength fluorescence region shown in Fig. 3 was due to the process described in Eq. (2a). Assuming that $|\mu_e|$ was the same for transitions to both upper states and that the potential curve for the state dissociating according to Eq. (2a) could be obtained simply by displacing the potential curve dissociating into Na*+I by the I* excitation energy, the full theoretical reduced fluorescence curve shown in Fig. 3 was obtained. The agreement between this full theoretical curve and the experimental data is very good, although similar good agreement might also be obtained by fitting the higher energy data to a potential curve appropriate to Eq. (2b).

Previous calculations of Franck–Condon factors for transition from a bound state to an unbounded state have often resorted to approximating the continuous nuclear wavefunction of the upper state by a delta function centered at the classical turning point of the motion.[25] Auxiliary calculations on the potential curves shown in Fig. 4 with this delta function approximation for the upper state wavefunctions appreciably distort the calculated reduced fluorescence curves, resulting in much poorer agreement with experimental data than is obtained using the true continuum wavefunctions. Two previous studies[9,22] have also offered somewhat more qualitative forms for the first of the upper state potential curves shown in Fig. 4. While qualitatively of the same form as that shown in Fig. 4, backcalculations based on these potential curves showed much poorer agreement with the experimental data of Fig. 3.

In the following section, the Franck–Condon factors computed in fitting the data of Fig. 3 are used to

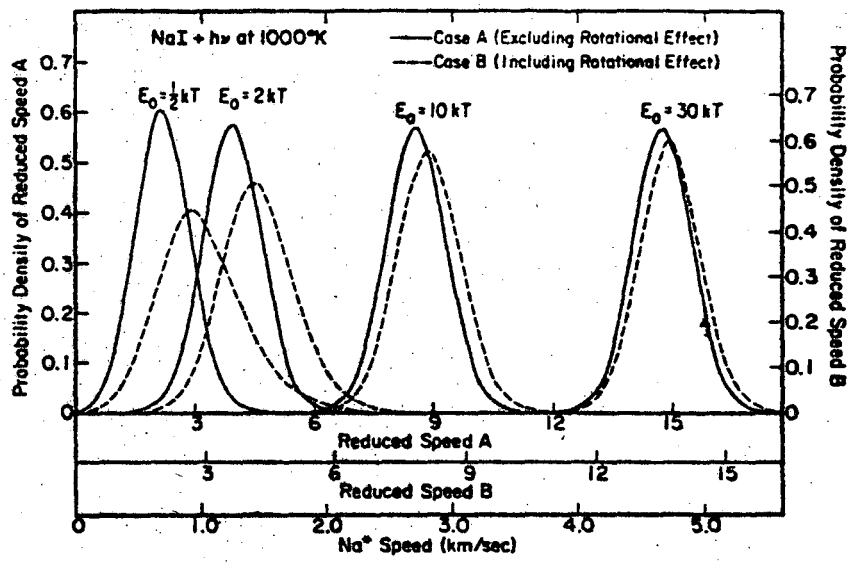

FIG. 5. Normalized probability density distributions for the LAB speed of an atom ejected with c.m. recoil energy given by Eq. (3) from a diatomic molecule with a thermal velocity distribution. The solid curves were calculated for the reduced speed A distribution considering only thermal translational energy in the target molecule, Eq. 17. The dashed curves were drawn for the reduced speed B probability density obtained by considering both thermal distributions in translational and rotational energies of the diatomic target; these reduced variable curves were calculated from Eq. (23) for the mass factors appropriate to the Na* product of photodissociation of NaI. These second probability density functions are also given (unnormalized) in terms of the absolute Na* speed for photodissociation of NaI at 1000°K.

estimate probability density functions for speeds of photodissociatively produced Na*. Before closing this section, however, it should be noted that the procedure adopted here of fitting the observed reduced fluorescence above ~2100 Å by a single upper state potential curve is an approximation. Indeed, a number of considerations[12,23,30] indicate that this D-lines fluorescence is actually a consequence of absorptions to a number (or at least two) of rather closely spaced upper potential curves, all of which correlate asymptotically with $Na^*(3p\,^2P)$ and $I(^2P_{3/2})$. However, the Na* speed distributions computed in the next section are not unduly sensitive to the forms of the Franck-Condon factors, so that the procedure adopted here should provide an excellent first approximation.

The Photodissociatively Generated Na* Speed Distributions

The authors know of no general expression available in the literature for the distribution in speeds of the atomic products of the photodissociation of a diatomic molecule. Zare and Herschbach[30] did treat the more complex problem of the distribution in vector velocity of the Na* produced by photodissociation of NaI; however, their distribution functions were arrived at by numerical computations and were based on the potential energy function given in Ref. 9. In this section, an analytic expression is derived for the probability density function, $P_{v,T,v_0}(V)$ of Eq. (6), of LAB Na* speeds produced by photodissociation of an NaI molecule in vibrational level v with thermal distributions in translational and rotational energies. This is then combined with the Franck-Condon factors discussed in the preceding section to arrive at the full probability density function, $P_{T,v_0}(V)$ of Eq. (6). This is approached by assuming that the Na* recoils away from the NaI c.m. at some one direction with a distribution of c.m. speeds u which is computed from the excess photon energy plus the NaI rotational energy which appears as radial recoil energy asymptotically. The distribution in LAB Na* speeds for recoil events at this one c.m. angle is then obtained by considering the distribution in scalar values of $\mathbf{V}=\mathbf{u}+\mathbf{v}_{NaI}$ obtained by averaging over all of the values of the randomly oriented, thermally distributed, $\mathbf{v}_{NaI}$. This distribution in V is then subsequently employed to calculate the distribution in relative speeds of approach of Na* to a foreign quenching gas M, i.e., the distribution in scalar lengths of

$$\mathbf{g}=\mathbf{V}-\mathbf{v}_M, \tag{12}$$

by averaging over the randomly orientated, thermally distributed values of $\mathbf{v}_M$. Thus, this procedure circumvents the far more complex problem treated in Ref. 30 of the distribution in angles of recoil of the Na* relative to the incident direction of the ultraviolet flux.

The Distribution Function Ignoring Rotation

In order to assess the relative contributions of NaI translational and rotational energies to the breadth of the Na* speed distributions, the $P_{v,T,v_0}(V)$ probability density function is first computed for photodissociation of NaI molecules with no rotational angular momentum. Assuming then that the Na* is produced with a recoil speed u_z given by Eq. (3) and directed along the z axis, the c.m. Na* recoil velocity distribution function for this case becomes

$$P_v^{J=0}(\mathbf{u})=\delta(u_x)\delta(u_y)\delta(u_z-u_z). \tag{13}$$

Since the thermal distribution in NaI velocities is given in terms of the most probable thermal NaI speed, the corresponding distribution in LAB Na*

speeds becomes

$$P_{v,T,v_0}(\mathrm{V}) = \frac{\pi^{-3/2}}{\bar{v}_{\mathrm{NaI}}^3}\int_u P_v(\mathrm{u})\exp\left(\frac{-v_{\mathrm{NaI}}^2}{\bar{v}_{\mathrm{NaI}}^2}\right)\left|\frac{\partial \mathrm{v}_{\mathrm{NaI}}}{\partial \mathrm{V}}\right| d\mathrm{u}. \tag{14}$$

Recognizing that the Jacobian factor is unity for a Cartesian coordinate system, Eq. (14) is readily evaluated for the $P_v(\mathrm{u})$ function given in Eq. (13) to obtain:

$$P_{v,T,v_0}{}^{J=0}(\mathrm{V}) = \frac{\pi^{-3/2}}{\bar{v}_{\mathrm{NaI}}^3}\exp\left(\frac{-V^2}{\bar{v}_{\mathrm{NaI}}^2}\right)\exp\left(\frac{-u_v^2}{\bar{v}_{\mathrm{NaI}}^2}\right) \times\exp\left(\frac{2u_vV\cos\theta}{\bar{v}_{\mathrm{NaI}}^2}\right) \tag{15}$$

in terms of θ, the polar angle between $\mathbf{u}_v$ and $\mathbf{V}$.

Equation (15) illustrates that the Na* velocity distribution obtained in this case is simply the original NaI thermal velocity distribution with its origin now centered about $\mathbf{u}_v$. The corresponding speed distribution may now be obtained by transforming to spherical coordinates and integrating over solid angle, i.e.,

$$P_{v,T,v_0}(V) = \int_\Omega P_{v,T,v_0}(\mathrm{V})\,V^2\sin\theta d\theta d\phi. \tag{16}$$

This integral is readily evaluated to give a speed distribution function which is naturally expressed in terms of a reduced Na* LAB speed $A = V/\bar{v}_{\mathrm{NaI}}$ and reduced Na* c.m. recoil speed $A_v = u_v/\bar{v}_{\mathrm{NaI}}$ as

$$P_{v,T,v_0}{}^{J=0}(A) = (2/\pi^{1/2})(A/A_v)\exp(-A_v^2)\exp(-A^2) \times\sinh 2AA_v. \tag{17}$$

Figure 5 shows plots of this reduced speed probability density function for several Na* c.m. recoil energies. The two highest recoil energies plotted ($E_0 = 10\ kT$ and $30\ kT$) were not achieved in this experiment, but are plotted to illustrate the rather severe broadening introduced by the NaI thermal velocity spread even in the case of recoil energies much greater than thermal energies.

The expression given in Eq. (17) has actually been discussed in the literature previously. Thus, Chantry and Schulz[31] gave its high recoil energy limiting form in discussing the kinetic energy of negative ions formed in dissociative electron attachment to diatomic molecules. Stanton and Monahan[32] have also derived an expression identical to Eq. (17) in considering the kinetic energy distribution of fragment ions in a mass spectrometer. This probability density function is also identical to that of the distribution in relative collision speeds for a monoenergetic beam impinging upon a thermal gas sample in a scattering cell, and in this context has been given in Ref. 33. Nevertheless, the derivation of Eq. (17) was presented here as a preliminary to the derivation of the probability density function obtained when the NaI rotational energy is included.

The Distribution Function Including Rotation

If the NaI molecule being photodissociated possesses rotational energy E_r, this energy will appear as an increment to the recoil energy so that the resulting Na* recoil speed will be given by

$$u^2 = u_v^2 + 2E_r/\kappa, \tag{18}$$

where $\kappa = m_{\mathrm{Na}}m_{\mathrm{NaI}}/m_{\mathrm{I}}$. Because of the small rotation constant and high temperature of the NaI vapor, the rotational energy may be treated as continuous and the rotational line strengths taken as unity[34] so that the thermal probability density function for rotational energy becomes

$$P(E_r) = (kT)^{-1}\exp(-E_r/kT). \tag{19}$$

This leads to a distribution in Na* c.m. recoil velocities directed along the z axis which is obtained from Eq. (19) as

$$P_v(\mathrm{u}) = (\kappa u_z/kT)\exp(\kappa u_v^2/2kT)\exp(-\kappa u_z^2/2kT) \times\delta(u_x)\delta(u_y); \quad u_z \geq u_v. \tag{20}$$

Inserting this expression into Eq. (14), the probability density function for Na* LAB velocities becomes

$$P_{v,T,v_0}(\mathrm{V}) = \frac{\kappa}{kT}\frac{\pi^{-3/2}}{\bar{v}_{\mathrm{NaI}}^3}\int_{-\infty}^{\infty}\int_{-\infty}^{\infty}\int_{u_v}^{\infty} u_z\exp\left(\frac{\kappa u_v^2}{2kT}\right) \times\exp\left(\frac{-m_{\mathrm{NaI}}v_{\mathrm{NaI}}^2}{2kT}\right)\exp\left(\frac{-\kappa u_z^2}{2kT}\right)\delta(u_x)\delta(u_y)du. \tag{21}$$

Without attempting to evaluate this integral, the desired probability density function for Na* speeds may be obtained by inserting it into Eq. (16). The resulting distribution function is naturally expressed in terms of reduced Na* LAB speed B and reduced Na* c.m. recoil speed B_v defined as

$$B = (1+\eta)^{-1/2}(V/\bar{v}_{\mathrm{NaI}}),$$
$$B_v = (1+\eta)^{1/2}(u_v/\bar{v}_{\mathrm{NaI}}), \tag{22}$$

in terms of the mass ratio $\eta = m_{\mathrm{Na}}/m_{\mathrm{I}}$. The results are given in terms of the error function[34] as

$$P_{v,T,v_0}(B) = \eta(1+\eta)^{1/2}B\exp\{[\eta/(1+\eta)]B_v^2\} \times\exp(-\eta B^2)G(B, B_v),$$

where

$$G(B, B_v) = \mathrm{erf}(B+B_v) + \mathrm{erf}(B-B_v), \quad B > B_v, \tag{23}$$
$$G(B, B_v) = \mathrm{erf}(B_v+B) - \mathrm{erf}(B_v-B), \quad B < B_v.$$

Figure 5 contrasts this speed distribution function obtained by including rotation with the simpler distribution obtained by ignoring effects of rotational energy and shows that the effects of rotational energy on the ensuing speed distribution may be appreciable for photodissociation near threshold. At very high recoil energies, however, Fig. 5 illustrates that the thermal diatomic translational energy is much more important than its rotational energy in determining the breadth of the speed distribution of the atomic product.

This effect arises because the rotational energy always adds to the recoil speed imparted by absorption of a photon whereas the translational velocity of the c.m. may add to or subtract from the c.m. recoil velocity.

The full probability density functions for Na* speeds produced photodissociatively in this work were calculated by means of Eqs. (23) and (6) and the Franck–Condon factors computed in the preceding section. The results of convoluting these distribution functions with the bandpass function of the monochromator are shown in Fig. 6. The curves of Fig. 6 are not unduly broadened relative to those of Fig. 5, indicating that the thermal distribution of NaI vibration energy was not a major source of breadth of the Na* speed distribution. Moreover, the curves of Fig. 6 illustrate that the 47-Å FWHM monochromator bandpass employed in the quenching studies had only a minor effect on the energy resolution obtained. In calculating averaged collisional quenching cross sections for comparison with experimental data, the probability distribution functions of interest are those for the relative collision speed g of Eq. (12). These distribution functions were calculated numerically by compounding the calculated, monochromator-bandpass-averaged Na* speed distributions with the thermal distribution in velocities of the quenching gases. Examples of these computed relative collision speed distribution functions for collision of Na* with a gas of much greater mass (I_2) and of comparable mass (C_2H_4) are shown in Fig. 6 and illustrate that this is another very important source of loss of energy resolution in the quenching studies in the case that the quenching gas has a mass comparable to or less than that of the species being quenched.

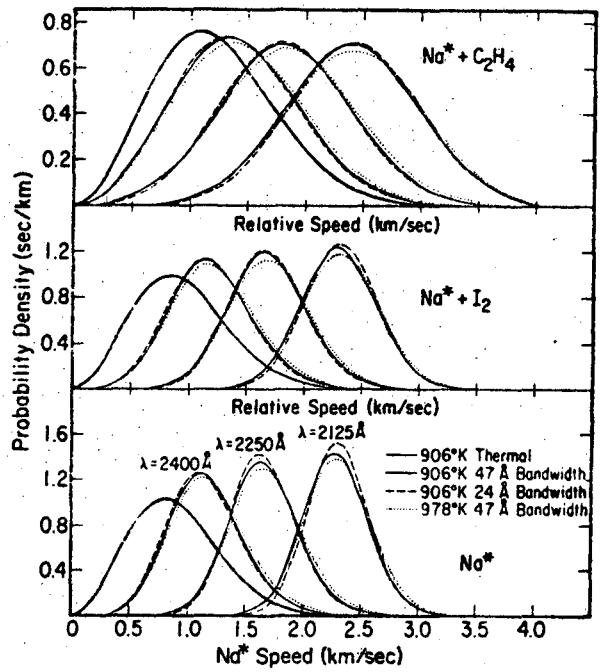

FIG. 6. The lower panel shows the calculated normalized probability densities for speed of Na* upon photodissociation of NaI by ultraviolet of the indicated wavelengths for a monochromator bandwidth function which is approximately triangular; the bandwidths quoted are the FWHM. Also shown as the bold solid curve is the Na* speed distribution corresponding to a 906°K thermal distribution. The upper two panels show the normalized probability density functions for relative speed for collisions of the Na* produced with the speed distributions given in the lowest panel with I_2 and C_2H_4 at 906°K. Also shown, as bold solid curves, are the corresponding thermal distribution functions for relative speeds in the collisions.

The Steady-State Na* Speed Distributions

The Na* speed distributions produced by photodissociation of NaI which were computed in the preceding section are certainly not precisely the true steady-state Na* speed distributions because of possible relaxation of the original distributions as a consequence of collisions between the Na* and other gas molecules which do not destroy the Na* electronic excitation but may alter its speed. These collisions may be either elastic or inelastic, but certainly the elastic collisions will be of dominant importance in relaxing the Na* speed owing to their higher probability of occurrence. The derivation of the true steady-state distribution is a difficult problem, beyond the scope of the present study. Nevertheless, this section offers some estimates of the likely magnitudes of the differences between the steady-state Na* LAB speed distributions and the photodissociatively generated distributions.

The cross section Q_R and associated rate constant $k_R=gQ_R$ for this relaxation by elastic collisions is dependent on the extent of perturbation of the Na* speed, V, considered. Thus, small impact parameter hard collisions may appreciably alter V, but these occur with a correspondingly small rate constant. On the other hand, large impact parameter collisions will occur much more frequently, but will produce a correspondingly smaller perturbation of V. Suppose then that the relaxation is characterized by some cross section $Q_R=\pi b_R^2$. If this is big, it will include contributions of some small impact parameter hard collisions, but will be dominated by larger impact parameter collisions for which $b\approx b_R$. Now, let k^* represent the rate constant for the first order decay of electronic excitation of Na*. Then, k^* will be given in terms of the rate constants for spontaneous emission of Na*, k_r, and for collisional quenching of Na*, k_q, by

$$k^*=k_r+k_q[M], \tag{24}$$

where $[M]$ is the quenching gas number density. Thus, the probability that an Na* atom will experience at least one elastic collision during its lifetime is given by $k_R[M]/(k^*+k_R[M])$.

In analyzing the problem further, it is natural to divide it into two regimes, that of high and low pressures of quenching gas, because the true steady-state Na* speed distribution will be dependent on pressure. In the low pressure regime, k^* is essentially given by

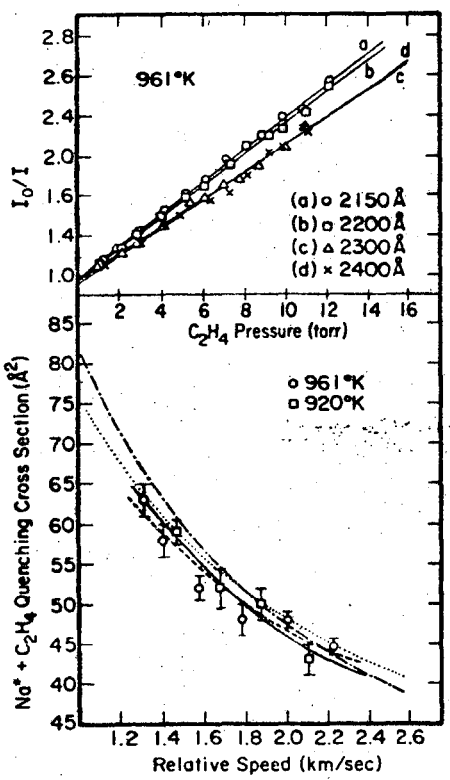

FIG. 7. Upper panel: The ratio of the reduced D-lines fluorescence for ethylene absent to that for ethylene present versus the ethylene pressure for four ultraviolet wavelengths studied. The straight lines show the least squares linear fits of the primary data to the Stern–Volmer relation, Eq. (27). Lower panel: The data points show plots of the phenomenological cross sections for collisional quenching of Na* ($3p\,^2P$) electronic excitation by ethylene, extracted from primary data such as is illustrated in the upper panel by means of Eq. (28), as a function of the characteristic relative collision speed given by Eq. (29). The error bars were obtained from the standard deviations of the slopes of the least squares linear fits of primary data to Eq. (27). The dash-dot-dash and dot-dot-dot curves show the true velocity dependence of cross sections $Q_q(g)$ assumed to vary as $K_5/g^{4/5}$ and $K_6/g^{2/3}$ respectively (with K_5 and K_6 given in Table I) which best fit the data. The solid and dashed curves show the corresponding fits to the data when these assumed functional forms of $Q_q(g)$ are averaged over the distribution in relative collision speeds.

k_r, known[11] to have the value of 6.2×10^7 sec^{-1}. Taking 1 torr of quenching gas as typical of this regime, this implies that k_R must be $\sim6\times10^{-9}$ cm^3 sec^{-1} in order that 50% of the Na* atoms experience at least one elastic collision during their lifetime. This corresponds to impact parameters b_R for the elastic collisions of $\sim$14, 12, and 10 Å for relative collision speeds of 1.0, 1.5, and 2.0 km/sec. At these large impact parameters, the collision is dominated by the long range form of the potential. Taking this long range form to vary as C_6/r^6, the high energy approximation for the classical elastic angle of deflection which should adequately describe these soft collisions gives

$$\chi\approx 15\pi C_6/8\mu g^2 b^6 \qquad (25)$$

in terms of the reduced mass of the collision partners, $\mu=m_{Na}m_M/(m_{Na}+m_M)$. If C_6 is assumed to be $\sim-10^{-57}$ erg-cm^6, this predicts very small angles of deflection, $\sim-0.2--0.3°$ for these collisions.

The velocity of the quenching gas is distributed thermally; however, the effect of the average collision may be estimated by assuming that the two gases intersect as right angles and assigning to the foreign gas its most probable thermal speed, $\bar{v}_M$. In this case, the following small angle approximation may be used to estimate the perturbation (ΔV) of the Na* speed:

$$\Delta V/V=\pm\chi[m_M/(m_M+m_{Na})](\bar{v}_M/V). \qquad (26)$$

For these small deflection angles, Eq. (26) provides estimates of 0.1–0.2% perturbations in V. Thus, at low pressures of quenching gas ($\sim$1 torr), the average elastic collision perturbs the Na* speed negligibly. Of course, virtually all of the Na* atoms may experience several elastic collisions which are even softer than those considered in the preceding paragraph. However, the effect of each of these very soft collisions will be very small. Moreover, they are about equally likely to increase or decrease V, so that the net spread in V might be expected to vary something as the square root of the number of these very soft collisions.

While these considerations suggest that the nascent Na* speed distributions are negligibly perturbed for low quenching gas pressures, the actual data on quenching cross sections was collected for quenching gas pressures in the range of $\sim$0.5–10 torr. In the high pressure limit, k^* is dominated by $k_q[M]$ so that the condition that half of the Na* atoms experience a relaxation collision prior to quenching becomes $Q_R=Q_q$. Recognizing, however, that the quenching collisions are probably given by the smaller impact parameter collisions, we may estimate that $Q_q=\pi b_q^2$. Then the important relaxation collisions will occur for impact parameters larger than this so that

$$Q_R=\pi(b_R^2-b_q^2).$$

Thus, the 50% relaxation collision is characterized by an impact parameter $b_R=\sqrt{2}b_q$. Taking benzene as an example and anticipating the results of the following section on the magnitude of the quenching cross section, Eqs. (25) and (26) suggest a deflection angle of $\sim3°$ and fractional perturbation of V of $\sim$1–2%. Of course, these are no longer extremely soft collisions and Eq. (25) is not strictly applicable, but should provide an adequate approximation.

Here again, this calculated small perturbation of V is encouraging, but may be somewhat misleading in this case. Thus, the probability that the Na* will suffer a hard collision is somewhat higher in this high pressure limit. For example, it seems probable that $\sim$10% of the Na* atoms may suffer a collision which could change V by as much as 50%. Nevertheless, it would appear that even at this high pressure limit, the true Na* speed distribution will resemble that calculated for photodissociation of NaI, but with some additional

breadth and a slight downward shift of the most probable Na* speed. In what follows, the quenching cross sections are analyzed in terms of the unrelaxed Na* speed distributions and this procedure is further supported by the observation that the high energy data evaluated in this study agree well with other results in the literature when extrapolated down to thermal energies.

DATA ANALYSIS AND RESULTS

If it is assumed that absorption of an incident photon by NaI vapor leads directly to production of an Na* as described by Eq. (1) and if it is further assumed that the Na* formed must either radiate or be collisionally quenched by the foreign gas present in the cell, the Stern–Volmer relation is obtained[9] for the ratio of the reduced fluorescence efficiency for finite quenching gas, $R_{[M]}$, to that for no quenching gas, R_0:

$$R_0/R_{[M]}=1+(k_q/k_r)[M]. \qquad (27)$$

Figure 7 shows this ratio as a function of ethylene gas pressure for four typical ultraviolet wavelengths studied. Also shown are least squares fits of the data for each wavelength to Eq. (27). It will be noted that the zero pressure intercepts of these least squares linear fits differ slightly from the value of unity predicted by Eq. (27). In all cases, however, this discrepancy in the intercept is less than the standard derivation in the intercept provided by the least squares fit. The rest of the primary data collected for ethylene as well as that collected for the other six quenching gases studied is not presented here. However, the data shown in Fig. 7 is typical of the quality of the data obtained for all of the quenching gases, with the possible exceptions of I_2 where the inherent room temperature vapor pressure of this material limited measurements to low quenching gas pressures and consequent D-lines fluorescence ratios near unity.

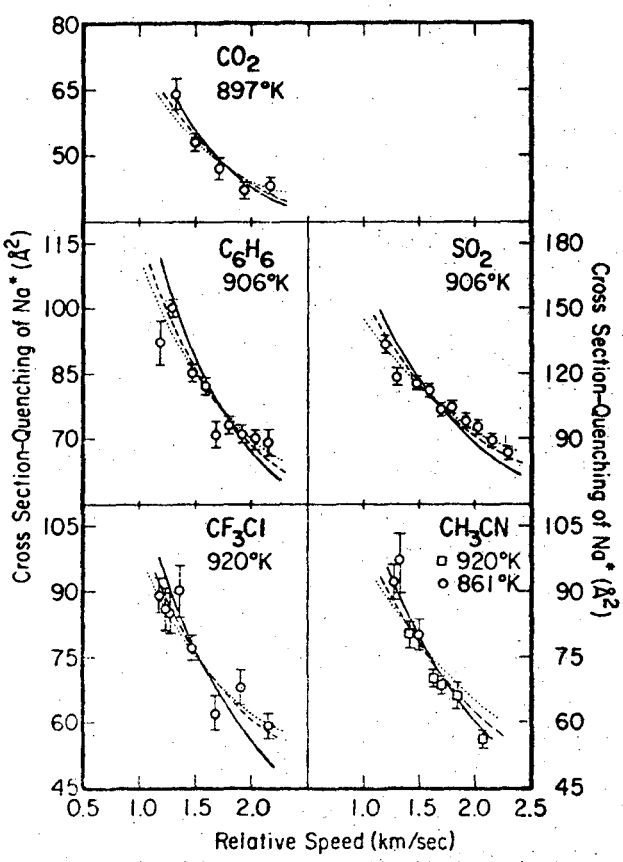

FIG. 8. Cross sections for collisional quenching of Na* by CO_2, C_6H_6, CF_3Cl, SO_2, and CH_3CN as a function of characteristic relative speed given by Eq. (29). The data points were evaluated by analyzing primary data by means of Eqs. (27) and (28); error bars reflect the standard deviations in k_q of least squares fits of primary data to Eq. (27). The curves show the best fits to the data points obtained by averaging cross section functions of the form $Q_q=K_s/g^{4/s}$ over the distribution in relative collision speeds: solid curve, $s=4$; dashed curve, $s=5$; dotted curve, $s=6$. The values of K_s employed are listed in Table I.

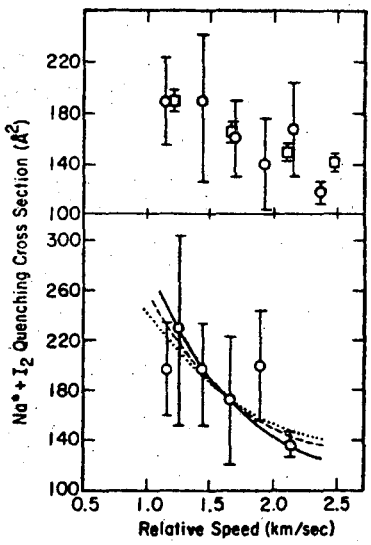

FIG. 9. Upper panel: Comparison of the velocity dependence of the Na*+I_2 quenching cross sections reported in Ref. 11 (open squares) with the values arrived at in this work (open circles), if the data collected here is analyzed by the procedure employed in Ref. 11. Lower panel: The velocity dependence of the Na*+I_2 quenching cross section measured in this work. The temperature was 906°K. All conventions are as described for Fig. 8.

If it is assumed for purposes of an initial analysis of the data that the quenching cross section is energy independent over the spread in relative collision velocities and that the Na* is produced with the one characteristic speed V_T given by Eq. (5), then the quenching rate constant may be shown to be given in terms of $x=V_T/\bar{v}_M$ as

$$k_q=\pi^{-1/2}\langle Q_q\rangle\bar{v}_M\psi(x)/x,$$

where

$$\psi(x)=x\exp(-x^2)+(2x^2+1)\int_0^x\exp(-y^2)\,dy. \qquad (28)$$

Quenching cross sections for the Na*+C_2H_4 collision evaluated from measured values of k_q by means of Eq. (28) are plotted in Fig. 7 against the characteristic relative speed,

$$\langle g\rangle=V_T+\bar{v}_M^2/3V_T, \qquad V_T>\bar{v}_M,$$
$$\langle g\rangle=\bar{v}_M+V_T^2/3\bar{v}_M, \qquad V_T<\bar{v}_M. \qquad (29)$$

The error bars shown reflect only the standard deviations in k_q provided by the least squares fits of the

TABLE I. Best experimental values[a] of K_s for Na^* quenching cross sections varying as $K_s/g^{4/s}$.

Quenching gas	10^9K_4	$10^{10}K_5$	$10^{11}K_6$
CO_2	0.88	0.78	1.6
C_2H_4	0.93	0.82	1.7
CH_3CN	1.2	1.1	2.3
CF_3Cl	1.2	1.1	2.2
C_6H_6	1.3	1.2	2.4
SO_2	1.8	1.6	3.3
I_2	2.9	2.6	6.0

[a] K_s is given in units of centimeter^4 · (centimeter/second)$^{4/s}$.

data to Eq. (27). Other sources of error certainly exist. For example, if the NaI dissociation energy employed here were in error, this could significantly alter the calculated values of $\langle Q_q \rangle$ and $\langle g \rangle$, although this would have less effect on the functional dependence of $\langle Q_q \rangle$ on $\langle g \rangle$ shown by the data.

Figures 8 and 9 give similar plots of phenomenological values of $\langle Q_q \rangle$ versus characteristic relative collision speed. Because SO_2 and C_6H_6 absorbed the shorter wavelength ultraviolet somewhat, a correction has been applied in arriving at the higher velocity data points plotted in Fig. 8 for these two gases. The magnitude of the correction was relatively uncertain, resulting in larger uncertainties in the data points plotted at higher velocities than are indicated by the error bars shown. This additional uncertainty was smaller than the standard deviations of the least squares fits to Eq. (27) in the case of benzene, but comparable for the SO_2 data at higher collision speeds.

The Stern–Volmer steady-state procedure for measurements of the quenching cross sections which is employed here is open to criticism because of its assumption of a very limited chemistry in the hot NaI-quenching species vapor mixture. The pulsed ultraviolet excitation followed by observation of the rate of decay of the subsequent Na* fluorescence which was employed in Ref. 11 to measure the I_2 quenching cross sections is a more direct method and is not subject to the possible criticisms of the Stern-Volmer technique. Unfortunately, this experimental method is much more time consuming and so was not adopted in this study. Figure 9 shows the very excellent agreement between the Na^*+I_2 quenching cross sections measured in this study (if the data analysis method employed in Ref. 11 is used) and the values arrived at in Ref. 11 by the more direct pulse technique. The relatively large error bars shown on our data points in Fig. 9 are a consequence of the limited I_2 vapor pressure region scanned. The Na^*+CO_2 quenching cross section data shown in Fig. 8 is also in similar good agreement with the values measured in Ref. 9 by the same Stern–Volmer technique employed here, if our data is analyzed by the procedure employed in Ref. 9.

In attempting to deconvolute the experimental data to arrive at the true dependence of the quenching cross sections on relative energy, it was assumed that the cross sections varied as $K_s/g^{(4/s)}$ with $s=4$, 5, or 6. As discussed in the following section, there are varying theoretical grounds for expecting that Q_q might vary in this manner. However, the main reasons for fitting the data to these functions were (1) that adequate fits to the experimental data were obtained and (2) that comparisons of the fits obtained with $s=4$, 5, and 6 provided some estimate of the sensitivity of the experimental data to the precise form of $Q_q(g)$. Having assumed a form of $Q_q(g)$, the quenching rate constant was calculated by numerical integration over the monochromator-bandpass-averaged probability density function for relative collision speeds derived in a previous section as

$$k_q = \int_0^\infty g Q_q(g) P_{T,v_0}(g) dg. \tag{30}$$

Phenomenological values of $\langle Q_q \rangle$ were then calculated from these computed values of k_q from Eq. (28) for comparison with the data points. Figure 7 shows the $K_5/g^{(4/5)}$ and $K_6/g^{(2/3)}$ forms of $Q_q(g)$ together with their energy averaged phenomenological quenching cross sections which best fit the ethylene data. Table I gives the K_4, K_5, and K_6 constants which best fit the experimental data for all seven quenching gases studied and Figs. 8 and 9 show the corresponding fits to the data obtained for the other six gases. In general, adequate fits are obtained for $s=4$, 5, or 6. The data seem to show some predilection for $s=6$ except for the CH_3CN quenching gas, where $s=4$ appears to provide the best fit.

DISCUSSION

Comparison with Other Work

The good agreement between the quenching cross sections obtained in this work and those derived by similar NaI photodissociative studies for I_2 (Ref. 11) and CO_2 (Ref. 9) has already been noted in the previous section. Most of the results of earlier workers employing the NaI photodissociative technique are discussed in Refs. 9 and 11 and so are not considered here. However, one other more recent study[10] by this technique provided cross sections for quenching of Na* by CO_2 and CH_3CN which are about a factor of two higher than those reported here. We cannot account for this discrepancy, but note again our agreement with Hanson's[9] results for CO_2.

In addition to comparisons of the present work with previous studies employing the NaI photodissociation technique, it is also of interest to compare these results with thermally averaged rate constants for quenching of Na* obtained by mixing Na vapor with quenching gases. The results of all such previous thermal studies

for the quenching gases examined here are listed in Table II. Indeed, one previous criticism[35] of the NaI photodissociative technique has been the inability to unequivocally compare the results obtained on quenching cross sections with thermal quenching rate constants. However, it has been argued in this work that the distribution in relative collision speeds is known and this has been used to fit the data to functional dependences of the form $Q_q(g)=K_s/g^{(4/s)}$. If this functional form is assumed to hold down to the lower collision speeds encountered in some of the thermal experiments, then thermal rate constants may be calculated from the expressions given in Ref. 39.

Table II compares literature values of thermal quenching rate constants with the extrapolations of the $K_6/g^{(2/3)}$ form of $Q_q(g)$ employed here. The first entry in the table for benzene (Ref. 36) was obtained by a pulsed excitation study of the lifetime of Na* fluorescence and so should be especially reliable. The C_6H_6 and C_2H_4 results reported in Ref. 37 were obtained by a steady-state resonance fluorescence technique and so are subject to possible ambiguities occasioned by imprisonment of resonance radiation and collisional broadening of the resonance absorption line. Indeed, comparisons of the results of Refs. 36 and 37 for N_2, H_2, CO_2, and C_6H_6 suggest that the results of Ref. 37 may be too high by about a factor of two. In view of this, the agreement shown in Table II between the results of the present work and thermal literature values for C_6H_6 and C_2H_4 is gratifying. Extrapolations of the K_4/g or $K_5/g^{4/5}$ fits obtained here would give higher values of $10^{10}k_q$(~11 and 13 for $s=5$ and 4 for C_6H_6) in poorer agreement with the literature values, although the change in going from $s=6$ to $s=5$ is not too pronounced. These comparisons and the data presented earlier suggest that $Q_q(g)$ varies as $g^{-(0.8-0.6)}$ for a speed range of ~0.7–2.0 km/sec for benzene and ethylene as quenching gases. The agreement between the CO_2 result obtained here and that obtained from studies of fluorescence in a flame reported in Ref. 35 is very good. Since the flame temperature was high, the characteristic thermal collision speed shown in Table II is comparable to those directly studied here, so that calculations of k_q for the $s=4$, 5, or 6 fits would all yield comparable values. The magnitude of k_q arrived at in Ref. 38 by a flame fluorescence study is in rather bad agreement with that obtained here. These workers also seemed to observe a g^{-2} dependence of Q_q for Na^*+CO_2, in clear disagreement with the results shown in Fig. 8 unless their observed temperature dependence was influenced by the changing thermal vibrational distributions in the CO_2.

TABLE II. Comparison[a] of thermal quenching rate constant measurements with extrapolations of $K_6/g^{2/3}$ fit.

Quenching gas	Ref.	T (°K)	g_T	$10^{10}k_q$ Reported	$10^{10}k_q$ This work
C_6H_6	36	~600	0.85	8.0	10
C_6H_6	37	400	0.69	16	10
CO_2	35	1600	1.49	7.5	8.2
CO_2	38	1790	1.58	17	8.4
C_2H_4	37	400	0.82	11	7.1

[a] Rate constants are given in centimeter³/molecule·second. The average relative collision speeds, $g_T=(8kT/\pi\mu)^{1/2}$, are given in units of kilometer/second.

Theoretical Implications

The Weak Quenchers

The data obtained here for CO_2, C_2H_4, CH_3CN, CF_3Cl, and C_6H_6 are well fit by quenching cross sections of the form $Q_q(g)=K_s/g^{(4/s)}$ with $s=4-6$. This is the well-known functional form of the cross section which is obtained by assuming that a constant fraction w of those incoming trajectories which surmount the barrier in the effective potential, obtained by adding the centrifugal repulsion to the true long-range potential $V(r)=C_s/r^s$, lead to quenching collisions. This model provides[39] an expression for $Q_q(g)$ in terms of the power law potential constant,

$$Q_q(g)=w\pi[s/(s-2)]^{(s-2)/s}[s/\mu]^{2/s}(C_s^{2/s}/g^{4/s}). \quad (31)$$

The Na* atoms involved in these collisions will experience electric quadrupole interactions. This could give rise to a long-range r^{-4} dipole–quadrupole potential for collisions with the polar quenching gases. However, this interaction would average to zero over one rotational period of the quenching molecule except in the case of symmetric top molecules with rotation about the symmetry axis excited. Moreover, no qualitative difference in behavior between the polar and nonpolar quenching gases was observed here, so that the dipole–quadrupole interaction does not appear to be dominant in general in determining the quenching cross sections. It may influence the CH_3CN collisions somewhat. This molecule does possess the largest dipole moment of the seven quenching gases studied here, and the energy dependence of its quenching cross section shown in Fig. 8 is somewhat steeper than is that of the other quenching gases. All of the quenching gases studied here should have electric quadrupole moments. Thus, this could give rise to long range r^{-5} quadrupole–quadrupole interactions. Although the quadrupole moment of the $3p$ state of Na* is apparently not known, our estimates indicate that these quadrupole–quadrupole interactions should be less than or comparable to the r^{-6} dispersion interactions at intermolecular separations important in determining the barriers in the effective potentials. However, owing to uncertainties associated with the Na* quadrupole

TABLE III. Comparisons of measured Na* quenching cross sections with projections based on long-range dispersion forces.

	CO_2	C_2H_4	CF_3Cl	CH_3CN	C_6H_6	SO_2	I_2
Reaction product	NaO	NaH	NaCl	NaCN	NaH	NaO	NaI
ΔD_0 [a]	−10	∼−8	66	∼46	∼−8	−14	85
μ (grams/mole)	15.3	12.6	18.9	14.7	17.8	16.9	21.1
α_2 (Å^3) [b]	2.6	4.3	5.0	4.4	10.3	3.7	9.7
$10^{11}K_6$(theor) [Eq. (32)]	2.0	2.5	2.2	2.4	2.9	1.7	2.7
$10^{11}K_6$(exptl) (Table I)	1.6	1.7	2.2	2.3	2.4	3.3	6.0

[a] $\Delta D_0 = D_0(\text{Na–X}) + E^* - D_0(\text{R–X})$ is the reaction exoergicity. D_0(Na–O) taken from and D_0(Na–CN) estimated from arguments given in R. R. Herm and D. R. Herschbach, J. Chem. Phys. 52, 5783 (1970); D_0 for NaCl and NaI taken from Ref. 24. Bond energies in the quenching gases taken from V. I. Vedeneyev, L. V. Gurvich, V. N. Kondrat'yev, V. A. Medvedev, and Ye. L. Frankevich, *Bond Energies, Ionization Potentials, and Electron Affinities* (St. Martin's, New York, 1966).

[b] For CH_3CN, from E. P. Lippincott, G. Nagarajan, and J. M. Stutman, J. Phys. Chem. 70, 78 (1966); for CF_3Cl, from W. N. Hess, R. L. Mather, and R. A. Nobles, J. Chem. Eng. Data 7, 317 (1962); all other values from *Landolt–Bernstein Zahlenwerte und Functionen*, edited by A. M. Hellwege and K. H. Hellwege, (Springer, Berlin, 1951), Vol. 1, Pt. 3, pp. 510 ff.

moment and the correct treatment of the relatively strong orientation dependences, any possible role of the quadrupole–quadrupole interaction will not be treated here and the discussion of the possible influence of long-range intermolecular forces on the measured quenching cross sections will be confined to a consideration of the dispersion forces.

Various approximations have been employed to estimate the C_6 dispersion force constant. Analysis of these approximations in Ref. 28 indicates that the dispersion contribution to C_6 should be well described by the Slater–Kirkwood approximation for these collisions; the dipole-induced dipole contribution should be much smaller and will be ignored. For this case of an excited alkali atom with one electron in the outer shell of polarizability α_1 much greater than the polarizability α_2 of the quenching gas, the Slater–Kirkwood approximation for C_6 provides the following approximation for $Q_q(g)$ from Eq. (31) in terms of e and m_e, the charge and mass of the electron:

$$Q_q(g) = w_2^2\pi[6e\hbar/m_e^{1/2}]^{1/3}(\alpha_1^{1/6}\alpha_2^{1/3}/\mu^{1/3}g^{2/3}). \quad (32)$$

Note that this expression predicts that for constant w, α_1, and g, the quenching cross section should vary as $(\alpha_2/\mu)^{1/3}$. This differs considerably from the older suggestion[40] that Q_q should scale as $\alpha_2\mu^{1/2}$ and the more recent suggestion[40] that the quenching of electronic excitation in molecules proceeds by a molecular predissociation so that Q_q should vary as $\mu^{1/2}I_2\alpha_2/R_x^3$, where I_2 is the ionization potential of the quenching species and R_x is a mean distance of closest approach of the collision pair.

Table III provides a comparison of the K_6 coefficients measured here with estimates provided by Eq. (32) for $w=1$ and $\alpha_1=51$ Å^3 (Ref. 41), and indicates that Eq. (32) (with $w=1$) does provide reasonable estimates of the magnitude of the quenching cross sections for the weaker quenchers studied here.[42] The K_6 values estimated from Eq. (32) may be slightly in error because of approximations involved in arriving at values of C_6; however, these errors should be small because K_6 depends only on the cube root of C_6. Thus, the entries in Table III clearly imply $w<1$ for CO_2, C_2H_4, and C_6H_6. Indeed, the results obtained here in conjunction with earlier work[5–11,35–38] suggest that most of the molecules which quench Na* electronic excitation may be broadly divided into four classes. In class A may be listed those molecules which cannot chemically react with Na* because all reaction channels are either endoergic or essentially thermoneutral (for which an appreciable activation energy might be expected), and whose lowest unfilled molecular orbital is a very high energy, antibonding σ^* orbital. Examples of molecules in this class, such as CF_4, saturated alkanes, and possibly H_2O, are all very inefficient quenchers. In class B are included those molecules which cannot chemically react with Na*, but which possess relatively low lying unfilled π^* molecular orbitals. These molecules, examples of which are provided by the CO_2, C_2H_4, and C_6H_6 studies here, are relatively efficient quenchers, with w values evaluated from Eq. (32) between 0.1 and 1.0. Since no change in chemical identity is effected by these quenching collisions, the Na* excitation energy must be dissipated either as translational recoil energy or as internal excitation of the class B quenching molecule. Studies of the chemiluminescence[43] produced by the Na*+CO quenching collision and of the inverse collisions using vibrationally[44,45] or translationally[46] hot species suggest that the electronic excitation is released predominately as internal (vibrational) excitation of the quenching molecule. Class C would include quenching molecules which, while not strongly electronegative, afford a very exoergic reaction channel. Results for two molecules of this class studied here, CH_3CN and CF_3Cl, suggest that their quenching cross sections may

be given by Eq. (32) with $w=1$, although results for many more molecules of this class will be required to unequivocally establish this. Finally, class *D* quenchers, exemplified by the I_2 and SO_2 behaviors observed in this work, are highly electronegative and exhibit quenching cross sections which are too large to be in interpreted in terms of the long range dispersion forces between the neutral reactants.

Thus, the quenching behavior observed in this study suggests that the long-range dispersion forces may account for the magnitude and energy dependence of quenching of Na* ($3p\,^2P$) by class *C* and, to a certain extent, class *B* quenchers. Nevertheless, many additional studies will be required to unequivocally establish the role of these dispersion forces. In particular, experiments are underway in our own laboratory to measure quenching cross sections of more highly excited ^2P states of alkali metal vapors. Thus, calculations reported in Ref. 41 indicate that the magnitude of the polarizability of a ^2P state of an alkali metal increases by about an order of magnitude for each increment of one in the principal quantum number of the outer p electron. Even more striking is the fact that for Na*, the polarizability changes sign on going from the $3p\,^2P$ to the $4p\,^2P$ state, so that the dispersion forces should be repulsive for collisions of Na* ($4p\,^2P$) and Na* ($5p\,^2P$) with foreign gas molecules. However, it should also be noted here that the quadrupole moment grows faster than does the dispersion force constant as the principal quantum number of the excited orbital of the atom is increased. Thus, analysis of results on quenching of more highly excited states simply in terms of dispersion forces will be subject to increasing criticism, and, indeed, the increasing quadrupole–quadrupole interactions may even mask the effect of the repulsive dispersion forces for these states of Na*.

The Stronger Quenchers

Table III indicates that SO_2 and I_2 exhibit cross sections for quenching of Na* ($3p\,^2P$) which are too large to be understood in terms of the centrifugal barrier in the effective potentials associated with the long-range dispersion forces between the neutral reactants. Thus, these large quenching cross sections demand a strong force which pulls the reactants into small internuclear separation and which is operative at very long distances. This requisite long-range force has long been understood[17a] in terms of an electron transfer model. In this model, the incoming Na* atom is seen to transfer its electron to the quenching gas at a distance R_c where the coulombic potential curve for the two ions becomes lower than that for the two neutrals, and the resulting coulombic force rapidly accelerates the ion pair formed to small internuclear separations. In terms of the ionization potential of Na*, I_1, and the electron affinity of the quencher, EA, R_c is given to lowest order by $e^2/(I_1-EA)$.

The electron affinity of SO_2 is reported to be[47] ~1.1 eV so that the crossing point, R_c, occurs at a relatively small internuclear separation, ~7.5 Å, in the Na*+SO_2 collision. Moreover, Table III indicates that the NaO+SO reaction channel is closed by energy conservation, at least at the lower relative collision speeds studied here. Thus, this quenching collision is pictured as taking place by Franck–Condon transitions from SO_2 to SO_2^- at R_c, exciting vibrational levels of SO_2^- on the incoming trajectory. The $Na^+-SO_2^-$ ion pair formed then may oscillate many times, passing through crossing points with the Na*+SO_2 and Na+SO_2 potential curves. In each passing, the SO_2^- may retransfer the electron to Na^+, at the same time making Franck–Condon transitions to various vibrational levels of SO_2. Calculations on the quenching of Na* by N_2 by this model are presented in Ref. 48 and suggest that it may provide an efficient mechanism for the dissipation of the Na* electronic excitation in vibrational excitation of SO_2 and recoil energy of Na from SO_2.

A recent measurement[49] indicates a relatively large electron affinity for I_2, 2.6 eV, corresponding to a calculated Na*+I_2 ionic curve crossing radius of ~36.5 Å. Table III indicates that this quenching collision can proceed by the very exoergic reaction forming NaI+I; indeed, the exoergicity is such that the reaction products might even be[11] Na+I+I. This suggests that any incoming Na*+I_2 trajectories which successfully cross onto the ionic curve have a very high probability of exiting in the reactive channel. In view of this, the observation that the Na*+I_2 quenching cross section measured here is very much less than πR_c^2 is understood in terms of a very low probability that the Na* will transfer its electron over the large distance required while the Na–I_2 internuclear separation is in the vicinity of the curve crossing radius. This same Born–Oppenheimer breakdown effect has recently been discussed[50] in rationalizing the observed branching ratios for thermal dissociation of alkali halide vapors between atoms and ions. Moreover, Child[51] has derived an expression for the translational energy dependence of the cross section for reactions such as Na*+I_2 by calculating the probability of a transition between the neutral and ionic curves as a function of the local radial velocity at R_c. Although his calculations did not extend to the very large crossing radius encountered here, extrapolation of his reported calculations is in qualitative agreement with the magnitude and velocity dependence of the Na*+I_2 quenching cross section measured here.

ACKNOWLEDGMENTS

We are indebted to Thomas Weber and Maynard Chen who collaborated on parts of the work described

here as undergraduates in the College of Chemistry: Mr. Weber helped in the original assembly of the equipment, especially the development of the H_2 arc continuum source; Mr. Chen assisted in the measurements of many of the quenching cross sections presented here. This work was supported by the U.S. Atomic Energy Commission through the Lawrence Berkeley Laboratory.

* Alfred P. Sloan Foundation Fellow.
[1] A. Terenin, Z. Physik. 37, 98 (1926).
[2] For a review, see G. G. Neuimin, *Elementary Photoprocesses in Molecules*, edited by B. S. Neporent (Consultants Bureau, New York, 1968), p. 3.
[3] V. A. Dudkin, V. I. Malyshev, and V. N. Sorokin, Opt. Spectrosk. 20, 554 (1966) [Opt. Spectrosc. 20, 313 (1966)].
[4] J. A. Bellisio and P. Davidovits, J. Chem. Phys. 53, 3474 (1970).
[5] J. G. Winans, Z. Physik 60, 631 (1930).
[6] A. Terenin and N. Prileshajewa, Z. Physik. Chem. (Leipzig) B13, 72 (1931).
[7] B. Kisilbach, V. Kondratjew, and A. Leipansky, Physik. Z. Sowjetunion 2, 201 (1932).
[8] V. Kondratjew and M. Siskin, Physik. Z. Sowjetunion 8, 644 (1935).
[9] H. G. Hanson, J. Chem. Phys. 23, 1391 (1955).
[10] D. J. Dowling, G. R. H. Jones, and E. Warhurst, Trans. Faraday Soc. 55, 537 (1959).
[11] L. E. Brus, J. Chem. Phys. 52, 1716 (1970).
[12] In a related experiment, H. G. Hanson, J. Chem. Phys. 27, 491 (1957) measured velocity dependent cross sections for interconversion of the Na* $3p\,^2P$ fine structure components.
[13] J. Gatzke, Z. Physik. Chem. (Leipzig) 223, 321 (1963).
[14] N. Prileshajewa, Physik. Z. Sowjetunion 2, 351, 367 (1932).
[15] N. Prileshajewa, Acta Physicochim. URSS 2, 647 (1935).
[16] D. J. Dowling and E. Warhurst, Trans. Faraday Soc. 55, 532 (1959).
[17] See, for example, the following reviews: (a) D. R. Herschbach, Advan. Chem. Phys. 10, 319 (1966); (b) E. F. Greene and J. Ross, Science 159, 587 (1968); (c) J. P. Toennies, Ber. Bunsenges. Physik. Chem. 72, 927 (1968).
[18] J. A. R. Samson, *Techniques of Vacuum Ultraviolet Spectroscopy* (Wiley, New York, 1967).
[19] G. Herzberg, *Molecular Spectra and Molecular Structure. III. Electronic Spectra and Electronic Structure of Polyatomic Molecules* (Van Nostand, New York, 1966).
[20] N. A. Finkelstein, Rev. Sci. Instr. 21, 509 (1950).
[21] G. Herrmann and S. Wagner, *The Oxide Coated Cathode* (Chapman and Hall, London, 1951), pp. 20, 33, 58ff.
[22] P. Davidovits and D. C. Brodhead, J. Chem. Phys. 46, 2968 (1967).
[23] H. G. Hanson, J. Chem. Phys. 47, 4773 (1967).
[24] L. Brewer and E. Brackett, Chem. Rev. 61, 425 (1961).
[25] A. S. Coolidge, H. M. James, and R. D. Present, J. Chem. Phys. 4, 193 (1936).
[26] Auxilliary $\bar{r}$-centroid calculations indicate that the assumption of the Franck-Condon principle introduces only very small errors here.
[27] A. Dalgarno, Advan. Phys. 11, 281 (1962).
[28] H. L. Kramer and D. R. Herschbach, J. Chem. Phys. 53, 2792 (1970).
[29] C. Maltz, Chem. Phys. Letters 3, 707 (1969).
[30] (a) R. N. Zare and D. R. Herschbach, Proc. IEEE 51, 173 (1963); (b) R. N. Zare and D. R. Herschbach, Lawrence Radiation Laboratory Report No. UCRL-10438, Berkeley, Cal., 1963.
[31] P. J. Chantry and G. J. Schulz, Phys. Rev. Letters 12, 449 (1964).
[32] H. E. Stanton and J. E. Monahan, J. Chem. Phys. 41, 3694 (1964).
[33] Fr. von Busch, H. J. Strunck, and Ch. Schlier, Z. Physik. 199, 518 (1967).
[34] M. Abramowitz and I. A. Stegun (Eds.), Natl. Bur. Std. (U.S.) Appl. Math. Ser. 55, (1964).
[35] D. R. Jenkins, Proc. Roy. Soc. (London) A293, 493 (1966).
[36] C. Bästlein, G. Baumgartner, and B. Brosa, Z. Physik. 218, 319 (1969).
[37] R. G. W. Norrish and W. M. Smith, Proc. Roy. Soc. (London) A 176, 295 (1940).
[38] H. P. Hooymayers and C. T. J. Alkemade, J. Quant. Spectry. Radiative Transfer 6, 847 (1966).
[39] H. S. Johnston, *Gas Phase Reaction Rate Theory* (Ronald, New York, 1966), pp. 142-145.
[40] For a recent review of quenching, see J. I. Steinfeld, Accounts Chem. Res. 1970, 313.
[41] R. W. Schmieder, A. Lurio, and W. Happer, Phys. Rev. A 3, 1209 (1971).
[42] The polarizabilities used are averaged over orientations and the minor effects due to the anisotropies of the polarizabilities of Na* and the quenching gases are neglected.
[43] J. C. Hassler and J. C. Polanyi, Discussions Faraday Soc. 44, 182 (1967).
[44] J. E. Mentall, H. F. Krause, and W. L. Fite, Discussions Faraday Soc. 44, 157 (1967).
[45] S. Tsuchiya and I. Suzuki, J. Chem. Phys. 51, 5725 (1969).
[46] V. Kempter, W. Mecklenbrauck, M. Menzinger, G. Schuller, D. R. Herschbach, and Ch. Schlier, Chem. Phys. Letters 6, 97 (1970).
[47] K. Kraus, W. Muller-Dzysing, and H. Neuert, Z. Naturforsch. 16a, 1385 (1961).
[48] E. Bauer, E. R. Fischer, and F. R. Gilmore, J. Chem. Phys. 51, 4173 (1969).
[49] J. J. De Corpo and J. L. Franklin, J. Chem. Phys. 54, 1885 (1971).
[50] J. J. Ewing, R. Milstein, and R. S. Berry, J. Chem. Phys. 54, 1752 (1971).
[51] M. S. Child, Mol. Phys. 16, 313 (1969).

ACKNOWLEDGEMENTS

The author wishes to express his sincere appreciation to Professor R. R. Herm for his guidance throughout the course of this work. His interest in this project and the helpful suggestions that he has always provided are grateful acknowledged.

Thanks are also expressed to all who have been participating in the same research group for their helpful discussions and suggestions. The author owes a special debt of gratitude to C. A. Mims for his cooperation in sharing this project; without him, little of this work would have been possible.

Special thanks are extended to the staffs of the Chemistry Department and the Lawrence Berkeley Laboratory. Their assistance has greatly contributed to the progress of this research.

This research was performed under the auspices of the United States Atomic Energy Commission.

TECHNICAL INFORMATION DIVISION
LAWRENCE BERKELEY LABORATORY
UNIVERSITY OF CALIFORNIA
BERKELEY, CALIFORNIA 94720